Stony Brook University

Environmental Redox Reactions of Iron

A Dissertation Presented

by

Matthew Carlton Frederick Wander

to

The Graduate School

in Partial Fulfillment of the

Requirements

for the Degree of

Doctor of Philosophy

in

Geosciences

Stony Brook University

August 2007

Stony Brook University

The Graduate School

Matthew Carlton Frederick Wander

We, the dissertation committee for the above cantidate for the

Doctor of Philosophy degree, hereby recommend

acceptance of this dissertation

Martin Schoonen – Dissertation Advisor
Professor of Geosciences

Richard Reeder – Chairperson of the Defense
Professor of Geosciences

Brian Phillips
Assistant Professor of Geosciences

John Parise
Professor of Geosciences

Jim Kubicki
Associate Professor of Geosciences, the Pennsylvania State University

This dissertation is accepted by the Graduate School

Lawrence Martin
Dean of the Graduate School

Abstract of the Dissertation

Environmental Redox Reactions of Iron

By

Matthew Carlton Frederick Wander

Doctorate of Philosophy

in

Geosciences

Stony Brook University

2007

While the focus of this study is the chemistry of iron, the goal of this study is the understanding of toxic waste remediation chemistry. This work is predominantly a modeling study that uses Marcus theory to define the components of the rate of electron transfer reactions. The components of an electron transfer reaction are known and quantifiable: thermodynamics, solvent, reorganization energy (HOMO-UMO gap), electronic overlap between reactant states, and heterogeneous reactions on mineral catalysts. All aspects are explored and their impact quantified for select examples: dinitrogen, green rust, chromate and uranium. This study utilizes hybrid density functional theory to determine rates of electron transfer. Particular focus is paid to the reorganization energies, which give indications of chemical periodicity, a key to the possibility that kinetics may achieve the same quantification as thermodynamics. The properties of Green rust are explored showing a slow intersheet transfer but fast intra-

sheet transfers. The study of Uranium triscarbanato reduction by ferrous iron shows a favorable transfer that is facile but moderately slow, limited by the distance the iron can approach the uranium. Water plays a significant role in mediating electron transfer reactions and we show that water at a surface has similar electrochemical properties as that in bulk. Finally, in a combined experimental theoretical study we showed that adsorption of ferrous iron onto goethite alters the thermodynamics of electron transfer but not the reorganization energy of the electron transfer. As a result alteration of the thermodynamic potential of iron is insufficient to reduce dinitrogen, which requires some form of pre-activation, such as ligation to multiple metal centers, in order to be reduced. Overall, we are able to demonstrate the importance of understanding environmental chemistry at the electronic scale in order to understand the redox transitions of aqueous species.

Table of Contents

List of Figures

List of Tables

Acknowledgements

The author wishes to thank Karenann Jurecki and the usual suspects.

Introduction

This work employs primarily quantum mechanical techniques to understand environmental reaction chemistry, specifically redox reaction kinetics. Quantum mechanics has been a part of physics and chemistry research for decades, however, their inclusion in the geochemical sciences is recent. In physics, density functional theory has been applied to mineral systems at high temperatures and pressures[1-5]. Hartree-Fock is chemistry's counterpart having been applied to chemical problems for over fifty years. In chemistry, Hartree-Fock and related approaches are considered pure, as they do not add additional terms to the Schrödinger equation like density functional theory does[6]. They focus on individual electron orbitals rather than the total electron density. Density functional theory has achieved great success predicting energies accurately with minimal computational requirements[7-9]. In the last few decades, efforts have been made to meld these approaches in hope of taking the best of both[10, 11]. The application of both approaches to environmental systems allows for an understanding of how electronic structure plays a role in environmental processes[12-15].

The question of which scale or scales is best when studying environmental problems is an important one. Two important scales will be the focus of this study: the physical and the chemical. Light microscopes can magnify to certain scales before quantum mechanical effects predominate, and no improvements in instrumentation can overcome that barrier. This barrier is fundamental to all of science. At scales smaller than nanometers, quantum mechanics, the behavior of atoms, protons, electrons, and photons, determine behavior. For larger scales chemical gradients, *e.g.* pH and Eh, replace

individual atoms in determining system behavior. Both scales must provide a congruent explanation of the system's behavior. However, in most approaches individual electrons are invisible and virtually undetectable. Therefore, to have a good understanding of chemical scale, or electronic structure behavior, ab-initio approaches are required.

Iron displays a wide variety of redox behavior including heterogeneous reactions, proton couple electron transfers, adiabatic, diabatic, inner-sphere and outer-sphere reactions[16, 17]. It is also an ideal benchmark system for studying other redox systems because it has two stable oxidations states that are only 1 step apart: +2 and +3. Ferrous iron is the reduced of the two forms that can be in equilibrium with water. Iron is an important reductant both naturally and as a man-made pollution remediator, which is why it is the focus of this study. Even in man-made remediators, such as the permeable reactive coating of ferrous iron that forms on scrap, reduced rusts are the active form or iron that reacts with pollutants[18-20]. Ultimately, the goal of this study is to understand the redox chemistry and kinetics of toxic waste remediation, how oxidation state can determine pollutant mobility, and how remediation approaches can overcome kinetic barriers to reduction.

1. In the first chapter, we examined the electronic structure of Green Rust in the form of $Fe(OH)_2^+$ as a coating of scrap metal iron in alkaline systems and its role in pollution remediation. This system is particularly challenging because it is a solid solution of oxidation states.
2. This chapter explores uranium reduction by ferrous iron in aqueous media in carbonate-rich alkaline conditions. This is an inner-sphere reaction, and is an important step on the path to U(IV) precipitation. U(V) is a focus of this study

because while it is a stable intermediate it is difficult to observe in the lab, and rarely seen in the environment.

3. While this chapter does not address redox chemistry directly it does address a fundamental component the role solvent plays in mediating those reactions. We calculated the electronic structure of water and the variation of the dielectric constant of water above a solvated mineral surface. Water forms a double layer above a mineral surface without any counter ions to promote that structure. The dielectric constant of water in the interfacial region is high, varying between about half of bulk water and values slightly higher than bulk.
4. In this chapter we switch from environmental chemistry to prebiotic chemistry, but the principles are the same. Experimentally, we explored the reaction of dinitrogen with aqueous ferrous iron, ferrous iron adsorbed onto goethite, and $Fe(OH)_{2(ppt)}$: white rust. The hypothesis was that photochemistry could break the N_2 triple bond, which was not the case indicating the importance of ligation in pre-activating the triple bond prior to the electron transfer.
5. Given the failure of photochemistry, in this chapter we wanted to explore the relationship between the failed environmental mechanisms and the biological systems that we know are capable of reducing dinitrogen at near room temperature. We compared using hybrid DFT the reaction of dinitrogen with aqueous ferrous iron versus that of ferrous iron adsorbed onto goethite with its part metalocubane structure. We demonstrate how ligation stabilizes the p* orbital in dinitrogen facilitating the electron transfer.

Overall, we demonstrated the importance of changes as small as the position of an electron or proton in environmental processes. Furthermore, it is possible to decompose reactions into their essential rate components, demonstrating that kinetics, like thermodynamics, obeys fundamental chemical properties like periodicity. These results indicate the importance of ab-initio modeling in the long-term pursuit of understanding toxic waste and other important environmental consequences of industrial and energy policy.

Structure and Charge Hopping Dynamics in Green Rust

Matthew C. F. Wander[1], Kevin M. Rosso[2], Martin A. A. Schoonen[1]

[1]Center for Environmental and Molecular Science (CEMS), Department of Geosciences, Stony Brook University, Stony Brook, NY

[2]Chemical and Materials Sciences Division and the Environmental Molecular Sciences Laboratory (EMSL), Pacific Northwest National Laboratory (PNNL), Richland, WA

Abstract. Green rust is a family of mixed-valent iron phases formed by a number of abiotic and biotic processes under alkaline suboxic conditions. Due to its high Fe^{2+} content, green rust is a potentially important phase for pollution remediation by serving as a powerful electron donor for reductive transformation. However, mechanisms of oxidation of this material are poorly understood. An essential component of the green rust structure is a mixed-valent brucite-like $Fe(OH)_2$ sheet comprised of a two dimensional network of edge-sharing iron octahedra. Liquid nitrogen temperature Mössbauer spectra show that any Fe^{2+}-Fe^{3+} valence interchange reaction must be slower than approximately 10^7 s^{-1}. Using $Fe(OH)_2$ as structural analogue for reduced green rust, we performed Hartree-Fock calculations on periodic slab models and cluster representations to determine the structure and hopping mobility of Fe^{3+} hole polarons in this material, providing a first principles assessment of the Fe^{2+}-Fe^{3+} valence interchange reaction rate. The calculations show that among three possible symmetry unique iron-to-iron hops within a sheet, a hop to next-nearest neighbors at an intermediate distance of 5.6 Å is the fastest. The predicted rate is on the order of 10^{10} s^{-1} (at 300 K) and 10^3 s^{-1} (at 70 K), consistent the Mössbauer-based constraint. All other possibilities, including hopping across interlayer spaces, are predicted to be slower than 10^7 s^{-1}. Collectively, the findings suggest the possibility of hole self-diffusion along sheets as a mechanism for regeneration of lattice Fe^{2+} sites, consistent with previous experimental observations of edge-inward progressive oxidation of green rust.

Introduction

When scrap iron is buried in an alkaline anoxic/suboxic environment, it forms a greenish-white coating called "green rust".[21-28] This material is family of structurally similar phases composed of alternating brucite-like $Fe(OH)_2$ layers with an anionic aqueous interlayer. Within the brucite-like layers is a solid solution of Fe^{2+} and Fe^{3+}, the ratio determined by the overall degree of oxidation.[29-32] Deviation from the ideal

$Fe(OH)_2$ layer stoichiometry due to positive Fe^{3+} defects created by oxidation requires charge compensation to maintain neutrality, which is provided by anions, such as chloride, sulfate, or carbonate anions in the interlayer space. This greenish-white substance coats the scrap iron entirely, forming both a physical barrier to the iron metal and, because of its Fe^{2+} content, a reactive surface capable of reducing many pollutants[33]. Compared to various other possible forms of Fe^{2+}, green rust has the most negative reduction potential, being nearly as reducing as zero-valent iron.[34] In an alkaline anoxic environment, it is capable of reducing CrO_4^{2-}, UO_2^{2+}, TCE, Ag, Au, Hg, NO_3^{1-}, SeO_4^{2-} and AsO_2^{1-}.[35-43] It has been shown that green rust is more reactive in this regard then aqueous Fe^{2+}.[44, 45] Hence, green rust has garnered significant attention in recent years as a key reactive intermediate between iron metal and contaminants in engineered reactive barriers.[46, 47]

Studies to determine mechanisms of green rust reactivity have been hampered by a lack of definitive crystal structure information. The structure of green rust is varied and many details are not fully understood. Perhaps the best understood green rust structure is its most oxidized end member, fougerite: $Fe(II)_2Fe(III)(OH)_6An{\cdot}n(H_2O)$ where An = Cl^-, $½CO_3^{2-}$, $½C_2O_4^{2-}$, or $½SO_4^{2-}$. Figure I-1 shows the structure of chloride form.[48] Cell dimensions, particularly the interlayer spacing, vary depending on the anion present.[49-54] Differences in individual sheets between green rust and ideal $Fe(OH)_2$ "white rust" include the interlayer spacing 8.762 Å vs. 4.6013 Å, respectively, and cell dimensions along the basal plane, which shorten by 0.1 Å (Fig. 1).[55] Green rust will also undergo deprotonation of structural hydroxyl groups in the presence of certain weak bases.[56, 57] The transition between white and green rust occurs at approximately 20% oxidation[58, 59]

when the sheets develop enough positive charge that Coulombic repulsion causes the sheets to separate. Figure I-1 illustrates the structural differences between green rust and white rust, and shows the octahedral iron sheet structure that is common to the two materials.

An aspect of green rust reactivity that is particularly important in this regard is its ability to redistribute charge within the brucite-like $Fe(OH)_2$ layers. Many iron oxides are semiconductors known to possess sufficiently high electron mobilities that long range charge transport is possible.[60-65] Electrons in these materials tend to be localized corresponding to very narrow conduction band widths,[66-68] which lead to the formation of small polarons.[16] A small polaron can be viewed as a quasi-particle consisting of a localized electron (or hole) self-trapped in the lattice distortion it creates. Movement of charge occurs by thermally activated site-to-site polaron hopping equivalent to the transfer of a single electron via a Fe^{2+}-Fe^{3+} valence interchange reaction. This feature of iron oxides has demonstrable implications for their reactive behavior that includes controlling the physical form of adsorbed Fe^{2+},[69-71] their ability to accept electrons during bioreduction,[72-75] and their ability to donate electrons across distances.[61, 73] Given the structural similarities between the iron oxides at the local level, it is reasonable to hypothesize that similar behavior is operative during the oxidation of $Fe(OH)_2$ layers in green rust materials.

Therefore, in this study we set out to provide computational molecular modeling insights into fundamental structural and kinetic aspects of green rust oxidation. Here we focus just on the basic building block of the reduced green rust end-member, the brucite-like $Fe(OH)_2$ layer. We determine the structure of hole polarons associated with Fe^{3+}

defects in a single $Fe(OH)_2$ layer, and predict their site-to-site hopping rates along basal directions within an $Fe(OH)_2$ layer. Since the mobility of polarons is tied in part to the magnitude of the lattice distortion and its crystallographic extent, we analyze how the polaron is manifested in the $Fe(OH)_2$ structure and determine its radius. This question is also important for understanding whether or not the distortion associated with a polaron influences the tendency of adjacent sites to oxidize.

Numerous Mössbauer spectra of green rust have been collected both on synthetic and natural green rust samples,[23, 35, 50, 51, 56, 76-81] which do not show[82] a characteristic signature for intermediate valence on the iron, indicating that Fe^{2+}-Fe^{3+} valence interchange reaction is slower, at temperatures around or below 70 K, than the residence lifetime of the Mössbauer resonance or about 10^7 s^{-1}.[83] Correspondingly, a small polaron model yielded a maximum Fe^{2+}-Fe^{3+} charge hopping rate in layered Fe-silicates of only 10^6 hops/second,[61, 73] consistent with Mössbauer. Therefore, we have an experimentally well-established cutoff value of 10^7 s^{-1} around liquid nitrogen temperature for the hopping rate to which our theoretical predictions can be compared. In addition to examining the lateral motion of polarons in $Fe(OH)_2$, we also address the possibility of interlayer charge transfer by the same mechanism.

We model charge transfer in $Fe(OH)_2$ using the principles of electron transfer (ET) laid out by Marcus and others,[84-87] in combination with quantum mechanical calculation of the parameters entering into Marcus' model. The physical quantities and mathematical rate expressions are effectively identical to the small polaron hopping model of Holstein.[88] The computational strategy is very similar to our recent studies of small polaron transport in other iron and chromium oxides.[16, 60-64, 73, 89]

The ET can be understood as occurring between two diabatic ET states ψ_A and ψ_B corresponding to the electronic states of the ET 'reactants', and the ET 'products', respectively. In our case, the ET reactants can be viewed as $Fe^{2+}{}_a + Fe^{3+}{}_b$ and the products are $Fe^{3+}{}_a + Fe^{2+}{}_b$ for any Fe site pair in a partially oxidized $Fe(OH)_2$ layer. The potential energies of the two electronic states can be viewed as having an approximate quadratic dependence on nuclear coordinates (Fig. 2). At equilibrium the energies of the two states correspond to minima in their respective potential energy surfaces, and in our case these energies are identical (i.e., the ET reaction is a symmetric one). The shapes of these potential wells are characterized by the reorganization energy (λ), which is the energy to distort the nuclear configuration of the reactants into the configuration of the products (including local bond distortions and repolarization of the surrounding lattice), or vice versa, without having moved the electron (Fig. 2). For ET to occur, the energies of states *A* and *B* need to be made equal, which is achieved by thermally-promoted fluctuations in the nuclear configuration (i.e., lattice vibrations). This coincidence condition corresponds to a crossing point between the two potential energy surfaces (Fig. 2). The height of the barrier at the crossing point is the diabatic activation energy ($\Delta G^{*\prime}$) for ET (Fig. 2). It has been shown that for parabolic potential energy surfaces and symmetric ET, $\Delta G^{*\prime} \approx \lambda/4$.[84]

Electronic interaction between Fe_a and Fe_b, such as by super-exchange mediated by bridging oxygen atoms, leads to a reduction in the activation energy. This effect is described by the electronic coupling matrix element (V_{AB}), which is the interaction integral for ψ_A and ψ_B evaluated at the crossing-point. The magnitude of V_{AB} dictates whether the ET is nonadiabatic (or the symantically equivalent diabatic), where the

transition probability at the crossing point is low, or adiabatic where the transition probability at the crossing point is close to 100%. The appropriate ET rate expression depends upon this 'adiabaticity'. As it turns out, all of the intralayer nearest-neighbor Fe^{2+}-Fe^{3+} ET reactions are predicted to be adiabatic, while the one interlayer ET we evaluated is nonadiabatic. The principal quantities that enter into the ET rate expressions for symmetric ET are the reorganization energy and the electronic coupling matrix element. For the adiabatic reactions, the adiabatic barrier height ΔG^* is estimated by subtracting V_{AB} from $\Delta G^{*\prime}$ (Fig. 2). These concepts are presented in more detail below.

Methods: We used periodic slab structure optimizations to compute the minimum energy configuration for a single layer of $Fe(OH)_2$ where all Fe sites are in the 2+ oxidation state, and also for the case where one of the lattice sites was oxidized to Fe^{3+}. We used the code Crystal03[90] for these structure optimizations, which allows for two-dimensional periodic boundary conditions to be applied to finite slab models. Crystal performs *ab initio* calculations of the ground state energy at either the Hartree-Fock (HF) or density functional theory (DFT) levels using a linear combination of Bloch functions defined in terms of local orbital functions. The local functions are in turn defined in terms of a set of Gaussian functions comprising the basis set. Basis sets used in the Crystal program must be free of overly diffuse functions typical of basis sets for molecular orbital cluster calculations to avoid too much overlap and quasi-linear dependence. We optimized the basis set for Fe^{2+} starting from the Durand-21d41G electron core pseudopotential basis set for Fe^{3+} of Catti and co-workers[91] using the program LOptCG.[92] This basis set was optimized in $Fe(OH)_2$ along with the diffuse functions for O in the Durand-41G basis set

of Apra.[93] The Fe^{3+} basis set of Catti and co-workers, optimized for use with α-Fe_2O_3,[16] was used for the Fe^{3+} 'defect' site.

All Fe^{2+} were assumed to be in a $3d^6$ high-spin configuration (four unpaired electrons), while the Fe^{3+} was assumed to be in a $3d^5$ high-spin configuration (five unpaired electrons); hydrogen and oxygen were closed shell. This is consistent with the high-spin occupation of the 3*d* orbitals found for most iron oxides and oxyhydroxides.[60, 94, 95] A ferromagnetic spin arrangement was assumed, consistent with ferromagnetic coupling often found for Fe-Fe interactions across shared octahedral edges.[96] To test for convergence with respect to cell size, the geometry optimizations were performed on 2×2 and 4×4 supercells of a single $Fe(OH)_2$ layer using two-dimensional periodic boundary conditions. For both supercells, we optimized the structure with and without a single Fe^{3+} defect. No symmetry restrictions were used (P1 symmetry). For the geometry optimization of the slab model containing the Fe^{3+} defect, a uniform background charge was used to neutralize the +1 unit cell. The optimizations were performed at the HF level to allow us to satisfy the requirement of extreme electron localization. HF is well known to overbind electrons,[97] whereas DFT often over-delocalizes electrons.[6] Here we build on previous work showing that good results are obtained for small polaron systems using HF.[16, 60, 61, 73]

As in earlier work, small clusters were used for calculations of the internal part of the reorganization energies: pertaining to bond distortion around the donor Fe^{2+} site and the acceptor Fe^{3+} site. These same clusters were also used for calculation of the electronic coupling matrix elements.[16, 60, 61, 73] These clusters were excised from optimized periodic slabs and charge neutralized by protonating edge oxygen atoms in a

manner that best preserves the local bonding symmetry around each edge oxygen atom and the bond valence they had in the periodic slab. Single-point energy calculations were performed on the various clusters at the HF level using NWchem[98] using a 6-311++G(d,p) for H, and O, and the Ahlrichs TZV basis set for Fe augmented by Hay-Wadt diffuse and polarization functions.[99-107] All calculations were performed in the gas phase.

A number of clusters were used, depending on the specific valence interchange reaction of interest in the lattice (Figs. 3a-d). We selected clusters that represented the crystallographically unique valence interchange reactions possible within the 4 × 4 unit cell. For example, Fe^{2+} atom is surrounded by six equivalent nearest neighbors comprising the first hexagonal 'ring' of possible locations for an Fe^{3+} acceptor site, and 12 next-nearest neighbor sites comprising the second 'ring' of possible locations for an Fe^{3+} acceptor site. There is one possible crystallographically unique nearest neighbor ET, and we model this using a single cluster containing both Fe sites (Fig. 3a) of stoichiometry $Fe(II)Fe(III)(OH)_2(H_2O)_8^{3+}$. For next-nearest neighbor ET, there are two crystallographically unique directions, one towards a side of the second hexagonal ring and the other towards the corners. Therefore, two more clusters of stoichiometry $Fe(II)_2Fe(III)(OH)_4(H_2O)_{10}^{3+}$ and $Fe(II)_3Fe(III)(OH)_6(H_2O)_{10}^{3+}$ were excised to represent these two sites (Fig. 3b and 3c). The 'fragment guess' option of NWChem was used to produce initial guess wavefunctions by concatenating component wavefunctions together with the desired electronic distribution and 3*d*-orbital occupation. Mulliken spin densities were used to confirm that energy minimized wavefunctions had converged to the desired solution.

A fourth cluster was created to evaluate the electronic coupling matrix element for interlayer ET. Two clusters representing the Fe^{2+} donor site and Fe^{3+} acceptor site were excised from the slab optimizations and merged into a supercluster model, with the two clusters aligned, separated, and oriented in a manner consistent with their positions across an interlayer space in fougerite. The Fe-Fe spacing was 8.762 Å, with no interlayer constituents considered (Fig. 3d). The supercluster stoichiometry was $2Fe(H_2O)_6$ and the net charge was +5. While this cluster was not necessary for understanding the electron hopping rates in the basal plane, it does provide an estimate of the rate of ET across the interlayer space and makes for a valuable comparison. Therefore, a total of four clusters were created, and four valence interchange reactions considered: One nearest neighbor intralayer ET reaction, two next-nearest neighbor intralayer ET reactions, and one interlayer ET reaction.

For each of the four valence interchange reactions considered, we needed to approximate the nuclear configuration for the ET transition states at the curve crossing-points. We used the linear synchronous transit (LST) method to do so,[108] as it has performed well in earlier work[60, 61]. This method is reasonably accurate where relatively small nuclear displacements are concerned,[108] such as in the separate iron polyhedra[109] in our system. The LST method assumes that the intermediate geometry is due to a linear combination of the reactants and products configurations, according to

$$X_n = \varepsilon X_p + (1-\varepsilon)X_r \,, \tag{1}$$

where X represents a set of nuclear coordinates for the reactants (r), the products (p), and their mixture (n). The mixing parameter ε varies from 0 to 1 and refers to the extent of progress along the reaction pathway. Because all of our valence interchange reactions are modeled as symmetric electron transfer reactions (i.e., there is no net free energy difference between the reactants and products states), we can expect that the potential energy surfaces will have similar curvature and the crossing point must be $\varepsilon = 0.5$, or in other words, halfway between reactants and products configurations. Therefore, single point energy calculations are required only for the reactants or products in their equilibrium configurations ($\varepsilon = 0$ or 1, since their energies are equivalent), for a charged reversed state ($\varepsilon = 1$ or 0 where the electron is forced to reside on the Fe atom bearing the ferric geometry), and for the crossing point ($\varepsilon = 0.5$).

To compute the electronic coupling matrix element V_{AB}, we used the quasi-diabatic method[108] using the wavefunction output of NWChem. At the crossing-point geometry, V_{AB} is obtained by solving the secular equation

$$\begin{vmatrix} H_{AA} - E & H_{AB} - ES_{AB} \\ H_{AB} - ES_{AB} & H_{BB} - E \end{vmatrix} = 0 \qquad (2)$$

where $H_{ij} = \langle \psi_i | H | \psi_j \rangle$ where i and j are equal to states A or B, H is the total electronic Hamiltonian, $S_{AB} = \langle \psi_A | \psi_B \rangle$, and E is the energy eigenvalue. The two roots of the secular equation give the upper and lower adiabatic surfaces (Fig. 2). Half of the energy difference between the two adiabatic surfaces at the crossing point is given by

$$V_{AB} = (1 - S_{AB}^2)^{-1} | H_{AB}^2 - (H_{AA} + H_{BB})S_{AB}/2| \ . \quad (3)$$

Full details can be found in Farazdel et al.[108]

The internal part of the reorganization energy is computed as the total electronic energy difference between the equilibrium and charge-reversed states for any valence interchange cluster pair. The external part of the reorganization energy derives from the energy to repolarize the material surrounding the donor and acceptor iron polyhedra. Because the presence of water is expected as a principal component of the green rust interlayer space, we chose to focus on this medium. For simplicity, this external part (λ_E) was computed using Marcus' continuum expression, which gives[110]

$$\lambda_E = (\Delta e)^2(1/2r_1 + 1/2r_2 - 1/R)(1/d_{op} - 1/d_s) \ . \quad (4)$$

In this equation r_1 and r_2 are radii for the donor and acceptor cavities, R is the distance between them, d_{op} is the optical dielectric constant, taken as 1.7689 for water, and d_s is the static dielectric constant, taken as 78.39 for water.[111] Values of R were taken from the final optimized slab structures. Cavity radii were chosen by averaging the lengths of Fe-O bonds in the excised cluster models. The external(λ_E) and internal(λ_I) reorganization energies were summed to yield the total reorganization energy: λ.

Utilizing the values of λ and V_{AB} from the cluster calculations, first order ET rate constants were computed using:

$$k_{et} = \nu_n e^{-\frac{\lambda/4 - V_{AB}}{kT}} \qquad \text{where } \lambda = \lambda_I + \lambda_E \quad (5)$$

or

$$k_{et} = \frac{V_{AB}^2}{h\sqrt{4\pi\lambda kT}} e^{-\frac{\lambda/4}{kT}} \text{ where } \lambda = \lambda_I + \lambda_E \quad (6)$$

depending on whether the reaction is adiabatic or nonadiabatic, respectively. The value of ν_n in the first equation represents a frequency of nuclear motion, which we equate with the highest infra-red active longitudinal optic phonon, which has the value 1.85×10^{13} s^{-1} in iron oxides[112, 113]. The adiabaticity was determined by comparing the value of $\frac{V_{AB}^2}{h\sqrt{4\pi\lambda kT}}$, the electron hopping frequency at the crossing point, from Eq. 6, to ν_n: if ν_n is greater, then the rate is nonadiabatic and determined by the transition probability at the crossing point (i.e., by the value of V_{AB}), otherwise the rate is determined by the probability of vibrational excitation to the adiabatic activation energy.[114]

Results

Our calculations indicate that green rust, $Fe(II)_nFe(III)(OH)_{2n+2}^{1+}$, is structurally different from white rust, pure $Fe(OH)_2$. Both the 2 × 2 and the 4 × 4 $Fe(OH)_2$ slabs are thicker, with oxygen atoms displaced farther outward along the *c* direction away from the plane of Fe ions forming the central plane of the slab, compared to the experimental crystal structure of fougerite. In the case of the 4 × 4 slab, this increase was from 1.018 Å to 1.086 Å (Table I-1). This difference could be due in part to the HF computational method which tends to overestimate bond lengths.

We now compare the optimized structures predicted for pure $Fe(OH)_2$ to the 'defect' case. For clarity, any slab model that was optimized with a charge of 0 is a pure

$Fe(OH)_2$ slab and will be called a 'no defect' case, and a slab model optimized with one Fe^{3+} site (i.e., a hole) amongst the remaining Fe^{2+} sites has an overall charge of +1 and will be called a 'defect' case. The 2 × 2 defect structure was optimized solely as a test for determining the ease of localizing the hole in the defect case and to examine the pattern of lattice distortion. Indeed the 2 × 2 slab did yield a localized hole for the defect case and manifested the polaron as a distortion of Fe-O(H) and Fe-Fe distances surrounding the defect (Table I-1). The significance of these results, beyond the confirmation of charge localization, is minimal as the unit cell size is too small to determine the polaron shape due to defect-defect interactions between image cells. Therefore, the 2 × 2 results were given less weight than the 4 × 4 slab optimizations, although comparison of the magnitudes of the atomic displacements is useful.

The results from the 4 × 4 slab optimization are more representative due to the larger supercell size. The 'no defect' slab model possessed P-3m symmetry, although no such symmetry restrictions were imposed during the optimization. The optimized slab for the defect case showed hole localization and an associated lattice distortion (collectively the polaron) that propagated in a number of ways. The predicted modification of Fe-O(H) and Fe-Fe distances surrounding the defect were very consistent with the 2 × 2 slab results. Collectively, these displacements reduced the geometric symmetry from P-3m to P-1. The oxygen atom planes contracted along the *c* direction toward the iron layer by a displacement of O_z = 1.086 Å → 1.056 Å, which is larger than the 0.99 Å vertical position in green rust (Table I-1). This is likely due to two factors, a slight elongation in the bonds predicted by HF and the regularity of defects due to the

supercell constraint, a characteristic intrinsic to the slab model not present in crystalline fougerite.

The polaron is manifested in the structure in a number of ways, as seen in Figures I-4 to I-7. Within the first ring of iron atoms surrounding the defect Fe^{3+} (the six nearest neighbors) half are pushed up above the original iron plane of iron atoms and half below. The seven iron atoms taken together remain co-planar with respect to one another but that plane is tilted with respect to the original plane of iron atoms. Surrounding this first ring is a second, rippled ring of iron atoms (the 12 next-nearest neighbors) related to each other by an S_6 symmetry operation. In other words, in the second ring three iron atoms are displaced up out of the iron plane in which they started, three are displaced down, and the remaining six iron atoms are not displaced. The magnitudes of these displacements, determined by comparing the difference in absolute *z*-coordinate for the 'defect' versus the 'no defect' slabs (aligned to be coincident on the defect iron atom), are displayed in Figure I-4. Considering just these iron Δz displacements, in visual appearance it resembles a flat-bottomed coffee filter (Fig. 4). In our second analysis of the iron atom displacements we computed and graphed the magnitudes of the in-plane (x,y) component of the displacement (Fig. 5). This graph shows that the first ring of iron atoms around the defect are displaced away from the defect, likely due to the increased electrostatic repulsion upon changing from Fe^{2+}-Fe^{2+} to Fe^{3+}-Fe^{2+} interactions between nearest neighbors. In turn, the outward displacements are accompanied by a slight 'compression' of the Fe-Fe distances between the first and second rings (Fig. 5), with slightly more 'compression' occurring at the corners of the second ring as opposed to the faces of the ring. Displacements can be observed in the third ring of iron atoms but at that distance

the magnitudes are very small and subject to interference from distortions propagating into the cell from adjacent image cells.

We also investigated the spatial variability of vertical oxygen displacements. Absolute Δz displacements for the oxygen atoms in the slab are shown in Figure I-6. Unfortunately, all that can be immediately gleaned from this Figure is that oxygen atoms move in the *z* direction as a function of both the polaron shape and the contraction of the oxygen planes. The resulting displacement is a combination of both effects. Due to this ambiguity, we found it necessary to subtract the contraction component from the oxygen vertical displacements and create a new contour plot that displays only the displacements arising from the polaron shape (Fig. 7). The result shows the oxygen vertical displacements are manifested as a symmetric radial function of distance from the defect.

Therefore, in both the iron and oxygen atom displacements, we find that the polaron has a symmetric radial structure. Its effect on any individual bond distances is small in general; the average atomic displacement overall was 0.0495 Å. Figure I-8 is a plot of average atomic displacements as a function of lateral distance from the Fe^{3+} defect. The plot shows that the polaron has an approximate exponential decay with increasing distance from the Fe^{3+} site. The atomic displacements at the cell edges are insignificant. The polaron has an approximate radius of 6 Å at which point the total displacement drops below 0.01 Å.

Given the predicted structure of the polaron, it is then possible to estimate the rate at which this polaron can 'hop' to an adjacent iron site by Fe^{2+}-Fe^{3+} valence interchange. We considered three symmetrically unique hops relative to the Fe^{3+} defect: to the nearest neighbor, to the corner in the next-nearest neighbor ring, and to the side in the next-

nearest neighbor ring (Fig. 9). Additionally, as discussed in the Methods section, the intersheet hop was also considered for an unoccupied interlayer space with a total hopping distance of 8.762 Å. The cluster models used for these calculations are shown in Figure I-3.

Calculated internal and external reorganization energies, electronic coupling matrix elements, and hopping rates are given in Table I-2. Values predicted for the internal reorganization energy λ_I are consistent with many other theoretical estimates for a variety of FeO_6 octahedra,[17, 61, 73, 89, 109, 115] a finding that is expected due to the similar coordination, polyhedra shape and size, and similar Fe^{2+}-O and Fe^{3+}-O force constants. In contrast to previous treatments of polaron hopping in iron oxides,[16, 63] the external reorganization energies were chosen to be based on repolarization of solvent water around the donor-acceptor iron sites, as opposed to repolarization of the surrounding solid phase. Water molecules are expected to have a substantial presence in the interlayer space of green rust and in the interaction volume for intrasheet polaron hopping. Therefore, calculated values for λ_E in the current case tend to be much higher than predicted for other iron oxides that are more compact framework structures excluding water.

Evaluation of the adiabaticity for each unique hop indicated that only the 'intersheet' hop is a nonadiabatic electron transfer, whereas all others are adiabatic. Calculated values of V_{AB} normally show an exponential dependence on the iron-to-iron hopping distance,[17, 67, 116] and this behavior is approximately followed in the current study (Fig. 10). The absolute value of the slope of a linear fit to $ln(V_{AB})$ as a function of R yields the decay parameter β, which is conventionally used in expressions of the type[86]

$$V_{AB} = V_{AB}^{0} \exp\left[-\beta\left(R - R_0\right)/2\right] \quad (7)$$

where V_{AB}^{0} is the value of V_{AB} at the optimal separation distance R_0. The value for β calculated in this study is 5.1 $Å^{-1}$. This excludes the nearest neighbor hop which turns out to be significantly off the trend (Fig. 10). The 'to side' next-nearest neighbor hop with the intermediate hopping distance of 5.67 Å has the largest predicted V_{AB}, enough to place it in the adiabatic electron transfer regime (Table I-1). This hop is therefore predicted to have the fastest rate in this material by far, having a frequency ~ 10^{10} s^{-1} at 300 K. While this rate is faster than the residence lifetime of the Mössbauer resonance, the majority of Mössbauer spectra of green rust has been collected at 78 K and at this temperature an intermediate iron valence signature is not observed. Accordingly, at 70 K our calculations predict that the rate of the 'to side' transition slows to ~ 10^{3} s^{-1}, well below the residence lifetime. Therefore, we find that our theoretical predictions are consistent with these measurements. The fast hopping frequency at room temperature is not readily evident in the limited available Mössbauer spectra published for this temperature[82] but questions remain regarding its interpretataion. The fast hopping frequency predicted by our model is similar to that found for nearest-neighbor hops over distances of ~ 3 Å in other iron oxides[61]. Although in the current case, nearest neighbor iron atoms are connected through a shared octahedral edge (i.e., double hydroxo bridged), the connectivity and the details of the bonding geometry have a strong influence on the electronic coupling.[61, 73] The 'to side' hop does not involve direct bonding connectivity between the donor and acceptor iron atoms and yet is predicted to have the fastest

polaron hopping rate. This result is unique among the iron oxides modeled previously using methods similar to those used here.

The intersheet hop over 8.76 Å through vacuum is predicted to be extremely slow. Unless the interlayer constituents provide a means for increasing the electronic interaction between sheets, the results suggest that intersheet polaron hopping is insignificant in green rust materials. For the purposes of this study, we did not include any intervening anions or water molecules because to do so would require a significant effort in producing structural configurations for interlayer constituents and the evaluation of intersheet polaron hopping rates as a function of the configuration. We leave this topic to future work.

Discussion

Our findings provide some indication of how green rust might interact with aqueous redox species. Rapid intrasheet hole polaron mobility suggests that for any particular Fe^{2+} site that is oxidized to Fe^{3+}, for example by electron transfer to an adsorbed oxidant species, that site can in principle be rapidly reduced back to Fe^{2+} by diffusion of the hole polaron through the lattice away from that site. This provides a mechanism of regeneration of electron donors at the mineral-water interface for continued reduction of adsorbed species. This mechanism invokes donor electron movement to the adsorbate, rather than the conventional view of the converse process. Our findings also suggest that this ability to replenish Fe^{2+} electrons will be strongly directional, with a much greater tendency to operate along basal directions within sheets than across the interlayer spaces. Transmission electron microscopic observations by

O'Loughlin and co-workers[36] show U(VI) reduction to U(IV) nanoparticles primarily at the edges of hexagonal green rust crystals The prevalence of U(VI) reduction at the crystal edges could reflect facile regeneration of Fe^{2+} donor sites at sheet edges by preferential electron migration to those locations from deeper in the crystal (or equivalently, preferential diffusion of holes away from the edges). Such a process would undoubtedly be coupled to a charge-compensating counter ion diffusion process that could involve, for example, concentrating anions in interlayer regions where the bounding sheets are dominated by Fe^{3+}. Despite this consistent picture, other explanations remain, including strong preferential adsorption of U(VI) species at green rust edges relative to basal planes yielding an apparent preferential uranium reduction exclusively at the edges.

Collectively our findings also lead to questions pertaining to the role of charge mobility in directing the oxidative breakdown of the green rust structure. These questions include whether charge defects are more stable near the center of the sheet or near the edges? Preferential edge-inward oxidation creates a strong distinction between reactive and available surface area on this material. Passivation of redox-active surface area on green rust crystals could manifest slower macroscopic oxidation rates and control the transformation process. This is potentially a result of slower intersheet versus intrasheet transfer. Only a limited range of Fe^{2+}/Fe^{3+} ratios are associated with stable green rust materials. This ratio ranges from 20% which has been purported to have the necessary charge repulsion to separate the sheets from one another to 33% which is the maximum number of sites which can be oxidized without having adjacent Fe^{3+}. Oxidative

degradation of the structure could be spatially linked to crystallographic regions undergoing active accumulation or depletion of charges facilitated by polaron mobility.

Conclusions

We have studied the structure and room temperature hopping dynamics of hole polarons in green rust materials using *ab initio* calculations. Hole polarons in green rust have a symmetric radial structure that decays exponentially to insignificant lattice distortions at approximately 6 Å. Hole polarons hop from iron site to iron site with rates that strongly depend on the crystallographic direction and hopping distance. Next-nearest neighbor 'to side' hops across intermediate iron-iron distances of approximately 5.7 Å are remarkably fast relative to all other possibilities including the nearest neighbor hops across the smallest iron-iron distances. This result differs markedly from the polaron hopping behavior examined for other iron oxides using similar methodologies. The 'to side' hopping frequency is predicted to be on the order of 10^{10} s^{-1} at room temperature and 10^{3} s^{-1} at 70 K, which is consistent with distinct Fe^{2+} and Fe^{3+} iron valences observed experimentally using Mössbauer spectroscopy at low temperature. Intersheet hopping is predicted to be slow in vacuum but this process may become feasible if interlayer molecules and ions facilitate the intersheet ET. More work is needed to evaluate whether or not interlayer constituents influence this rate. Collectively this work suggests that solid-state charge transport in green rust is facile, such that charge redistribution could play a major role in directing the transfer of electron equivalents out of green rust into adsorbed redox-active species. This finding provides a foundation for examining heterogeneous reductive degradation and reductive immobilization reactions

between green rust materials and environmentally relevant contaminant species such as TCE, UO_2^{2+}, and CrO_4^{2-}.

Acknowledgements

MCFW and MAAS are grateful for financial support from National Science Foundation (NSF)-Chemistry Division through the Center for Environmental Molecular Science at Stony Brook, Award #CHE-0221934 and a supplement that allowed MCFW to visit the William R. Wiley Environmental Molecular Sciences Laboratory (EMSL) to conduct part of this work. KMR acknowledges support from the Stanford Environmental Molecular Sciences Institute, jointly funded by NSF-Chemistry and the U.S. Department of Energy (DOE) Office of Biological and Environmental Research (OBER), and also from the Office of Basic Energy Sciences Geosciences Program. This research was performed in part using the Molecular Science Computing Facility (MSCF) in the EMSL at the Pacific Northwest National Laboratory. The EMSL is funded by the DOE OBER. Pacific Northwest National Laboratory is operated by Battelle for the DOE under Contract DE-AC06-76RLO 1830.

Table I-1: Select average interatomic distances and oxygen atom *z*-coordinates (Å) calculated using *ab initio* slab models compared to experimental counterparts.				
No Defect[a]	Fe-O		O_z	O-H
White Rust-exp.	2.1425		1.0183	0.8733
2 × 2-calc.	2.175(0.008)		1.085(0.007)	0.9577(0.0005)
4 × 4-calc.	2.18(0.02)		1.086(0.004)	0.9463(0.0002)
Defect	Fe^{2+}-OFe^{3+}	Fe^{3+}-OFe^{2+}	O_z	Fe^{3+}-Fe^{2+}
Green Rust-exp.	2.09[b]	2.09[b]	0.99	3.19
2 × 2-calc.[c]	2.038(0.002)	2.19(0.04)	1.051(0.001)	3.26515
4 × 4-calc.[c]	2.246(0.001)	2.035(0.001)	1.051(0.003)	3.293(0.001)

[a]Fe+2-Fe+2 distances were not calculated as the cell size was fixed to the experimental dimensions, in effect fixing the average Fe-Fe distance.

[b]The crystallographic structure presented only one bond distance, they did not specify whether this was to Fe^{3+} or Fe^{2+}.

[c]In both defect cases only the 6 nearest oxygens and the 6 nearest irons to the defect are included in the average.

Table I-2. Calculated hopping distances, reorganization energies, electronic coupling matrix elements, and hopping rates for polarons in green rust materials.

Hop	R/Å	λ_I/kJmol^{-1}	λ_E/kJmol^{-1}	V_{AB}/kJmol^{-1}	Rate/s^{-1}
To neighbor	3.29	152.8	132.4	11.5	6.11×10^{2}
To corner	6.53	157.2	247.9	6.8	5.15×10^{-4}
To side	5.67	176.8	230.0	88.3	8.33×10^{10}
Intersheet	8.76	113.7	277.4	0.03	1.42×10^{-8}

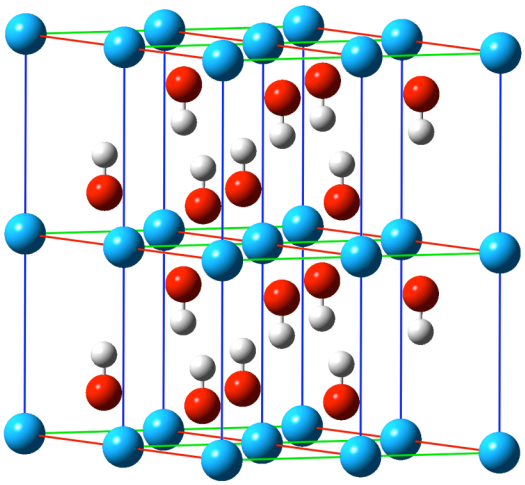

a)

b)

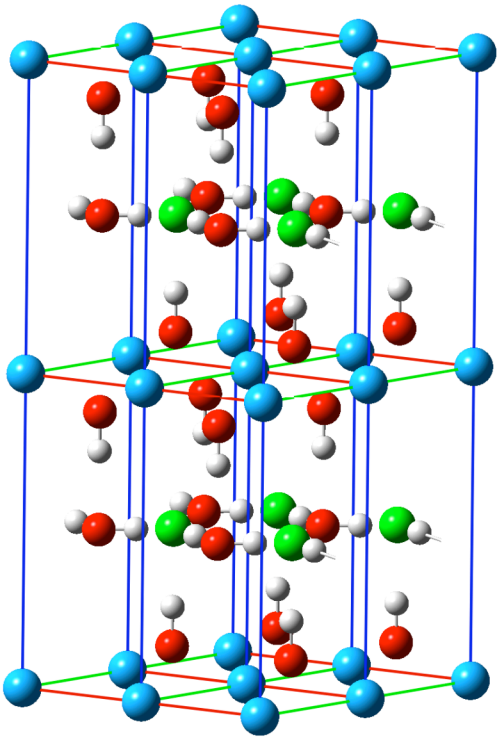

c)

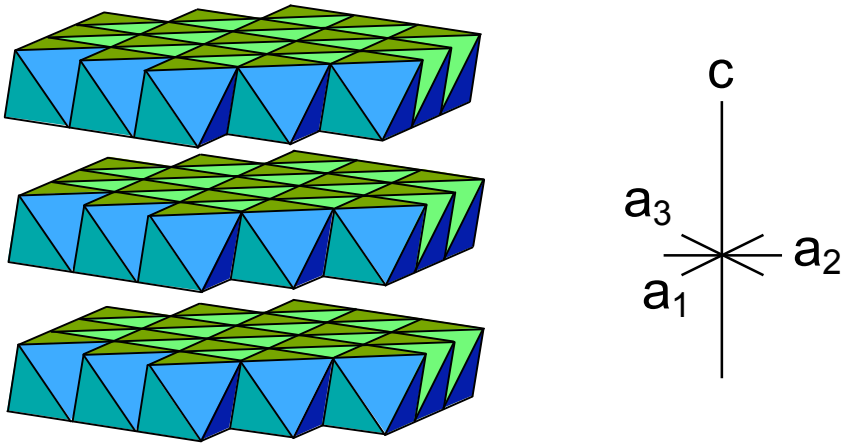

Figure I-1. Structure models of a) $Fe(OH)_2$ "white rust"[55] and b) simplified $Fe(II)_4Fe(III)_2OH_{12}Cl$ $(H_2O)_n$ "green rust" [48] (key: blue=iron, green=chloride, red=oxygen, white=hydrogen), and c) the polyhedral sheet structure common to both materials.

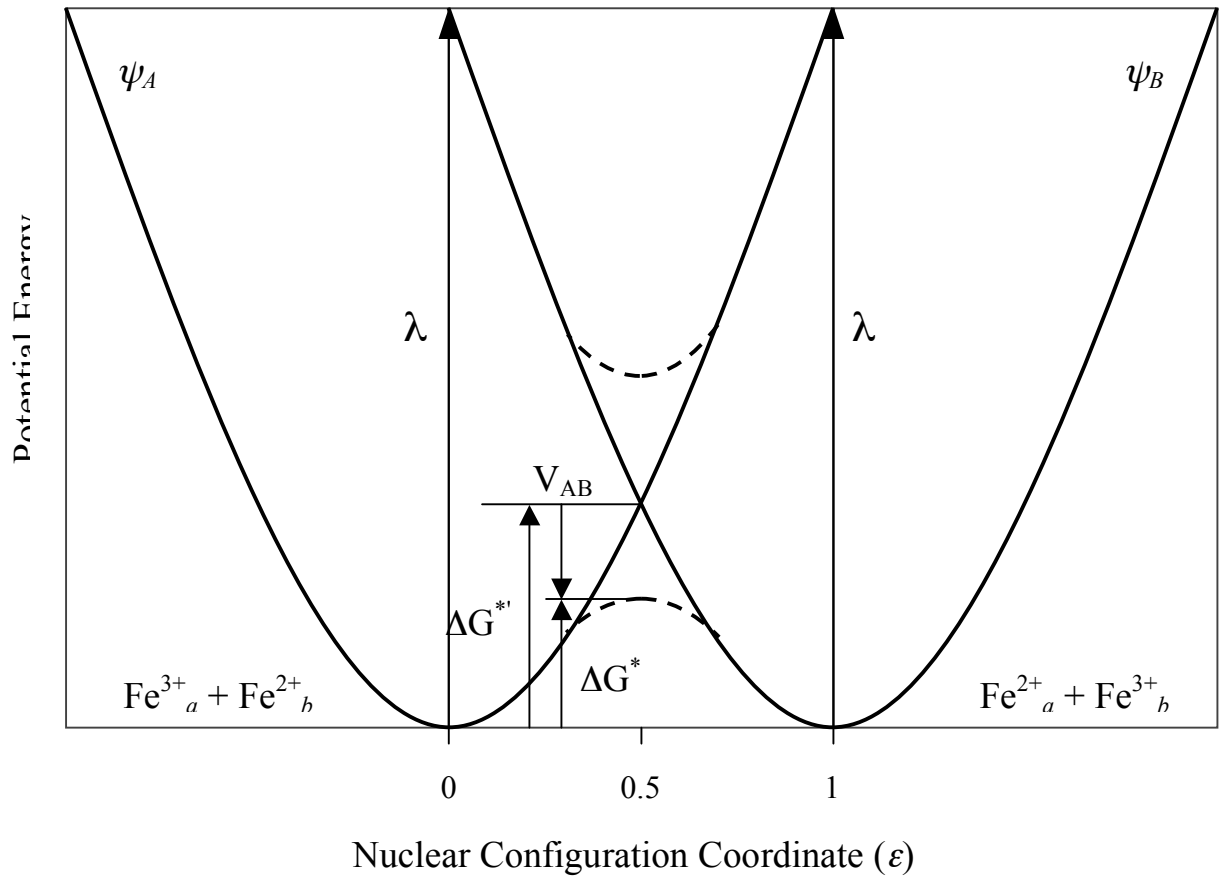

Figure I-2. Marcus two-state potential energy diagram showing a symmetric reaction typical of the polaron hopping treatment used in this study, and depiction of relevant quantities. See text for details.

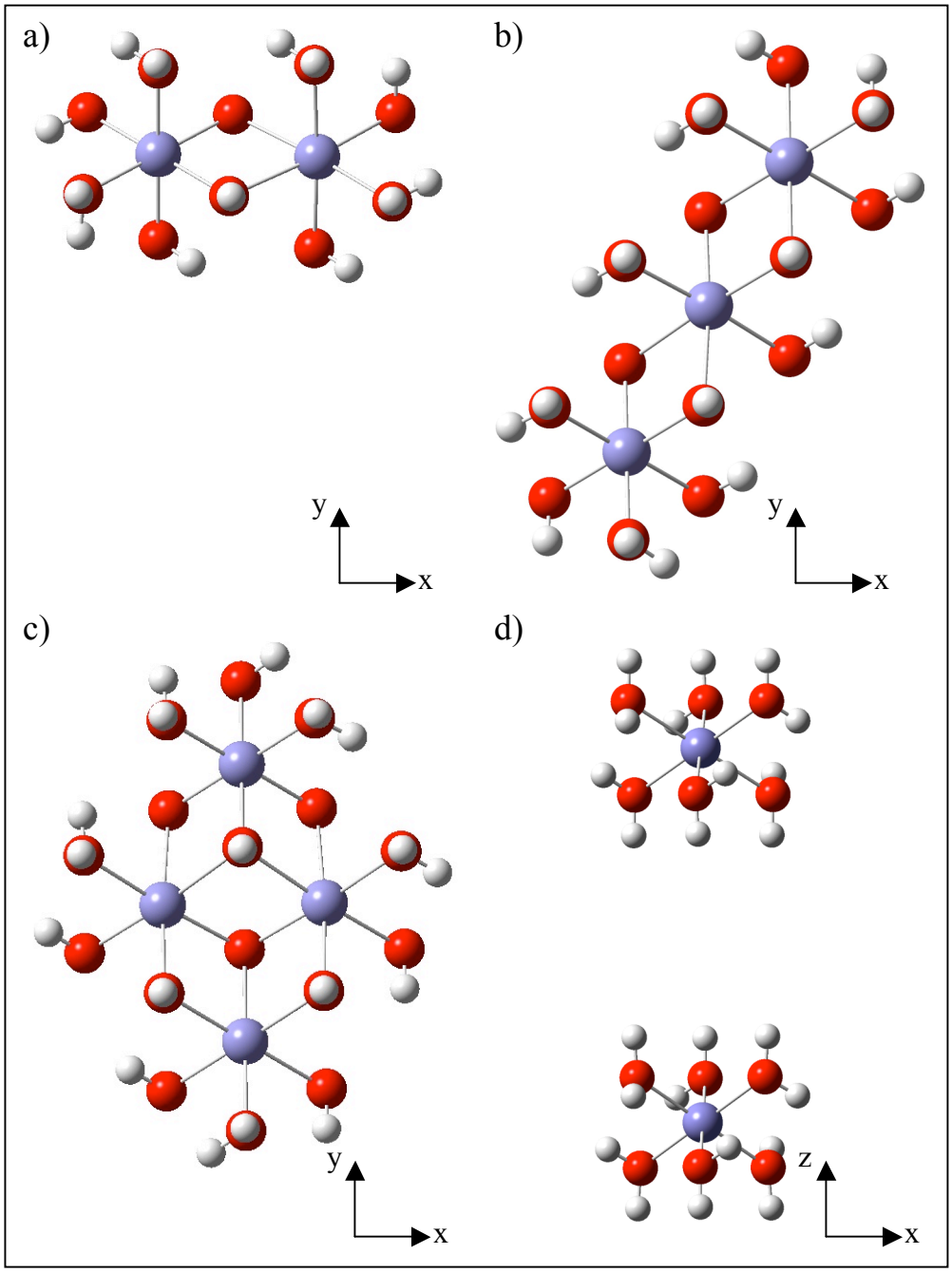

Figure I-3. Cluster models used in the determination of the internal reorganization energies, the electronic coupling matrix elements, and polaron hopping rates. They are: a) 'to neighbor' (top left), b) 'to corner' (top right) and c) 'to side' (bottom left) and d) intersheet (bottom right). See text for details.

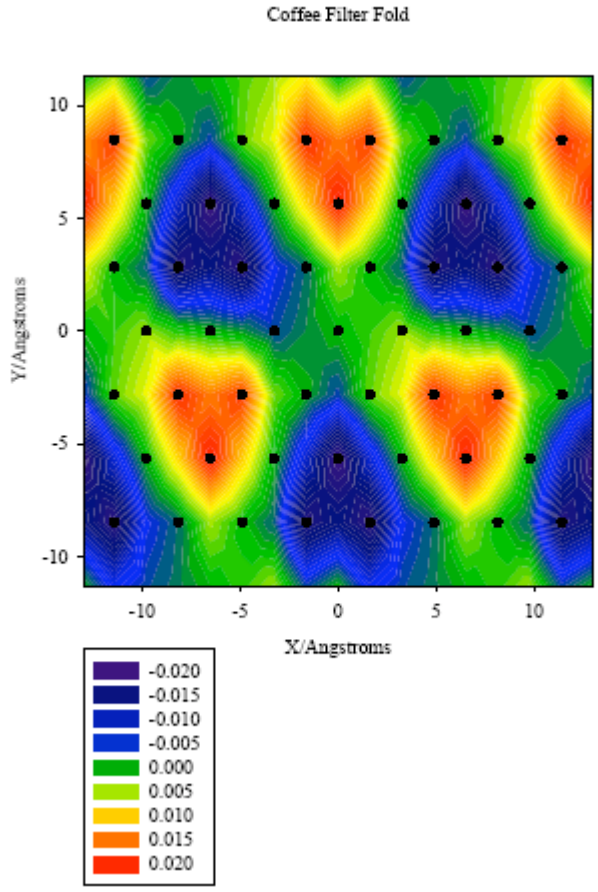

Figure I-4. A map of the Fe^{3+} 'hole' polaron in terms of Fe displacements in the *z* direction (normal to the basal surface). The sheet takes on a distinctive "coffee filter" distortion with the first ring tilted out of the plane and the second ring rippled.

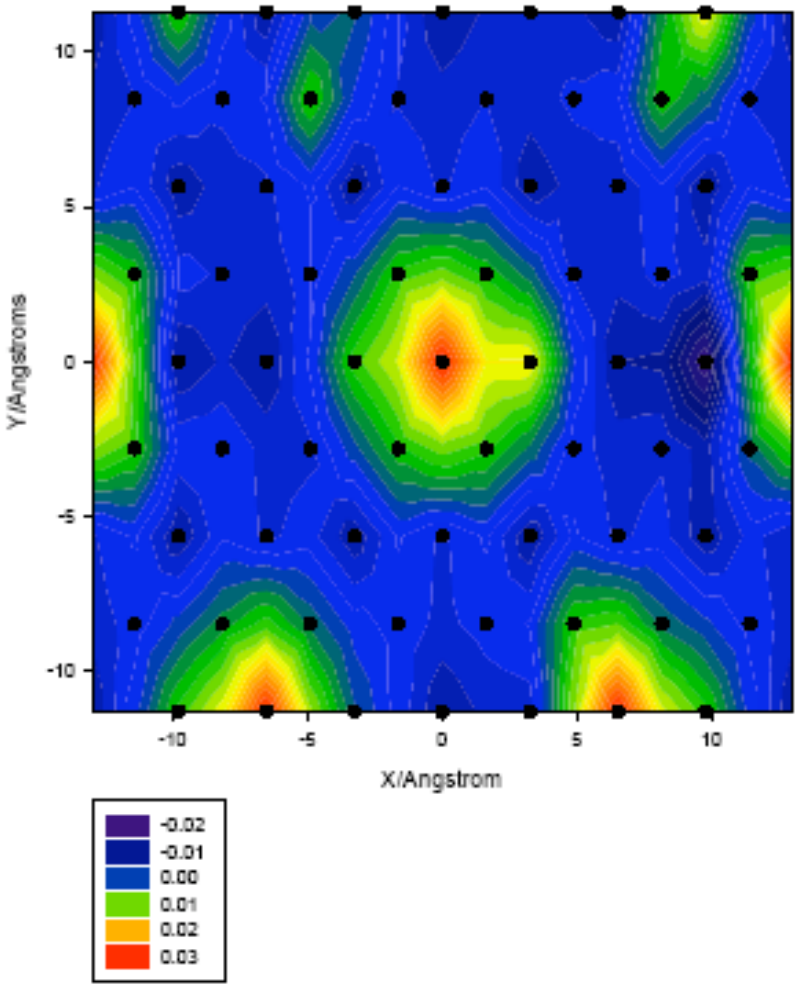

Figure I-5: A map of the Fe^{3+} 'hole' polaron in terms of Fe displacements in the *x* and *y* directions. The ring of nearest neighbor iron atoms is expanded while the ring of next-nearest neighbors is slightly compressed.

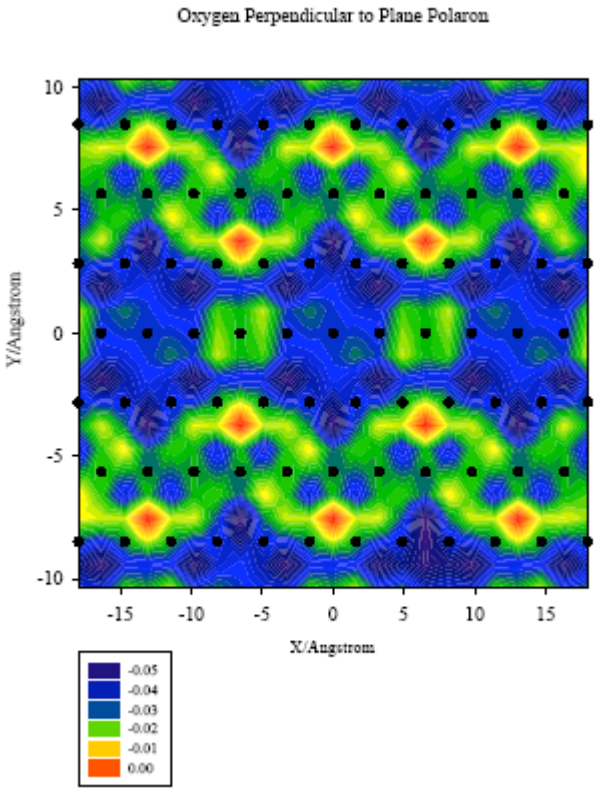

Figure I-6. A map of the Fe^{3+} 'hole' polaron in terms of oxygen atom displacements in the *z* direction. This characterization involves the polaron shape convoluted with overall contraction of the oxygen atom planes.

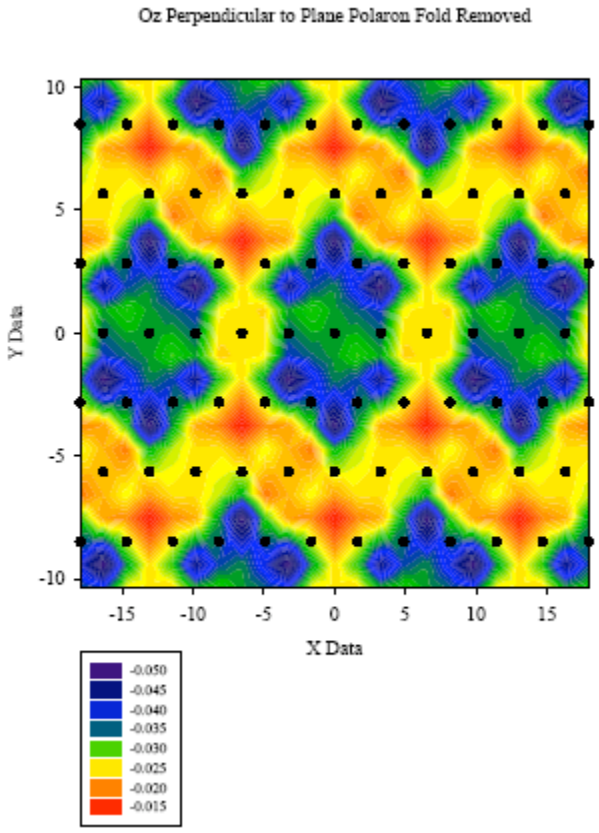

Figure I-7. A map of the Fe^{3+} 'hole' polaron in terms of oxygen atom displacements in the *z* direction with the contraction component removed. Radial symmetry is displayed in the oxygen atom displacements about the defect.

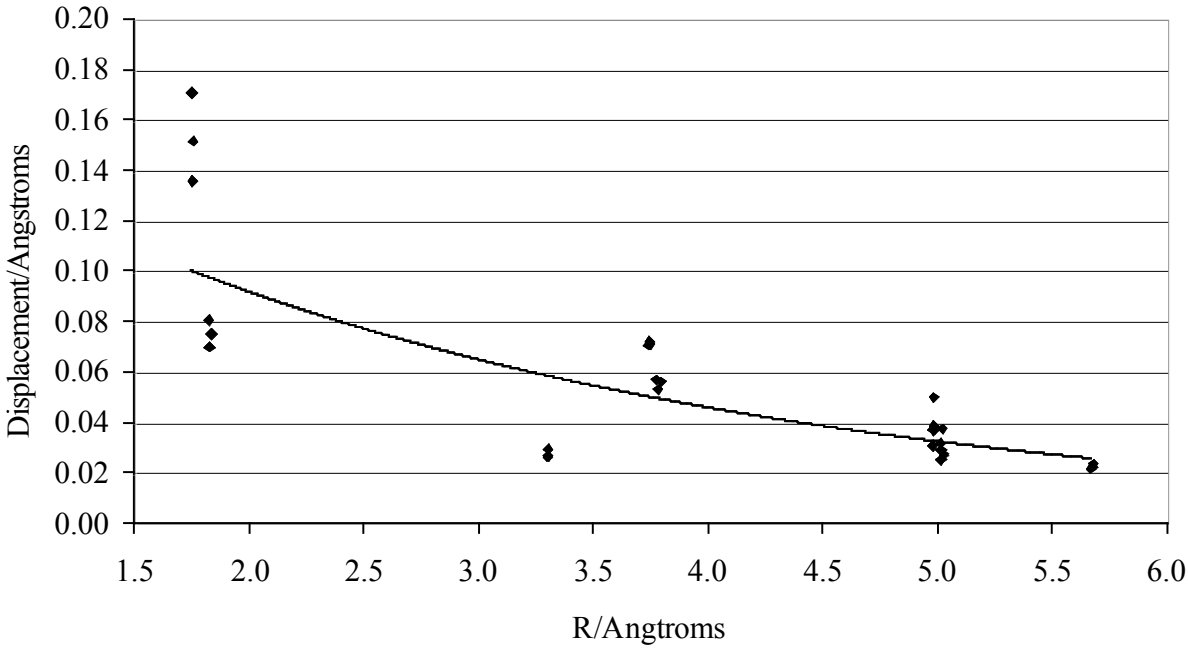

Figure I-8. Average atomic displacements associated with the Fe^{3+} defect as a function of distance from the defect. This graph shows the approximate exponential radial decay of the polaron.

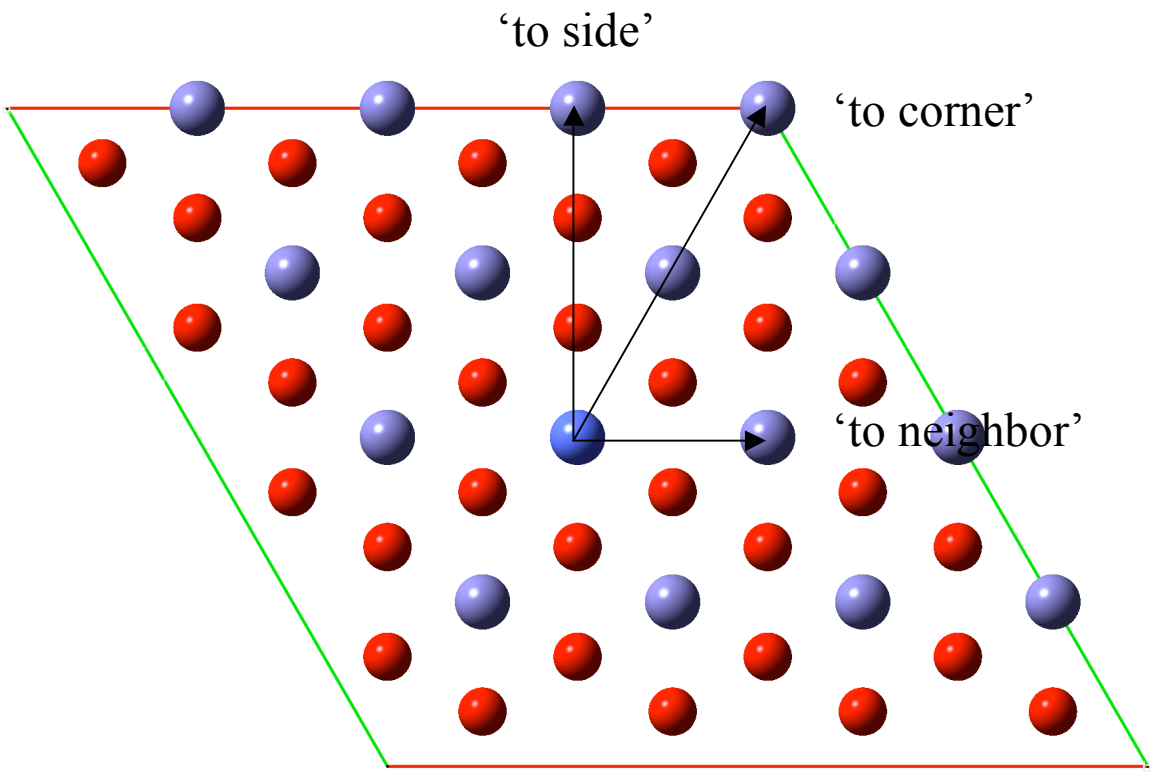

Figure I-9. This diagram shows the three unique electron transfers we considered in this study, drawn with respect to the structure of the 4 × 4 supercell.

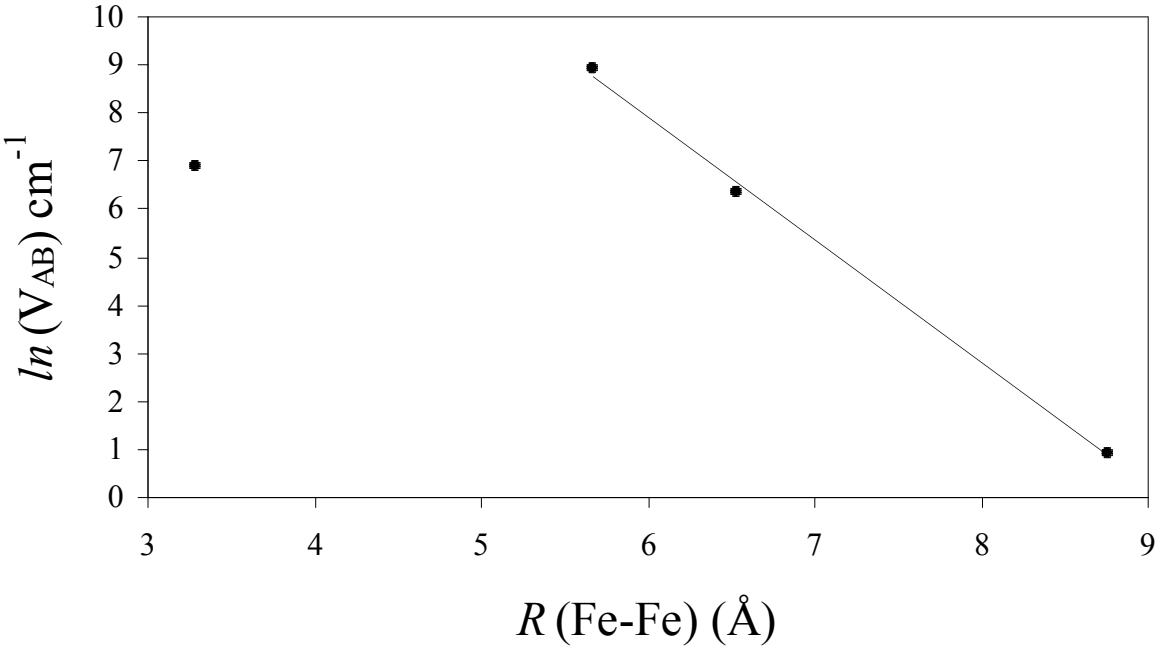

Figure I-10. Plot showing the exponential decay of the electronic coupling matrix element for hole polaron hopping as a function of the iron-iron separation distance, and the exceptionally low value calculated for the nearest neighbor hop. The decay constant $\beta = 5.1$ Å^{-1} for the linear trend; see text for discussion.

Kinetics of Triscarbonato Uranyl Reduction by Aqueous Ferrous Iron: A Theoretical Study

Matthew C. F. Wander[1,2], Sebastien Kerisit[3], Kevin M. Rosso[3], Martin A. A. Schoonen[1,2]

[1] Department of Geosciences, Stony Brook University, Stony Brook, NY 11794-2100

[2]Center for Environmental and Molecular Science (CEMS), Stony Brook University

[3]Pacific Northwest National Laboratory (PNNL), Richland, WA

Abstract Uranium is a pollutant whose mobility is strongly dependent on its oxidation state. While U(VI) in the form of the uranyl cation is readily reduced by a range of natural reductants, by contrast complexation of uranyl by carbonate greatly reduces its reduction potential and imposes increased electron transfer (ET) distances. Very little is known about the elementary processes involved in uranium reduction from U(VI) to U(V) to U(IV) in general. In this study, we examine the theoretical kinetics of ET from ferrous iron to triscarbonato uranyl in aqueous solution. A combination of molecular dynamics (MD) simulations and density functional theory (DFT) electronic structure calculations is employed to compute the parameters that enter into Marcus' ET model, including the thermodynamic driving forces, reorganization energies, and electronic coupling matrix elements. MD simulations predict that two ferrous iron atoms will bind in an inner-sphere fashion to the three-membered carbonate ring of triscarbonato uranyl, forming the charge-neutral ternary $Fe_2UO_2(CO_3)_3(H_2O)_8$ complex. Through a sequential proton-coupled electron transfer mechanism (PCET), the first ET step converting U(VI) to U(V) is predicted by DFT to occur with an electronic barrier that corresponds to a rate on the order of

~ 1 s^{-1}. The second ET step converting U(V) to U(IV) is predicted to be significantly endergonic. Therefore, U(V) is a stabilized end-product in this ET system, in agreement with experiment.

INTRODUCTION

Uranium pollution, a consequence of uranium mining as well as nuclear research and development, is a problem that is complicated by many factors. Foremost of these is that uranium mobility is highly dependent upon its oxidation state. U(VI) is highly soluble and therefore mobile in oxic aqueous environments in the form of the divalent dioxo-uranium cation UO_2^{2+}. Electron transfer (ET) to U(VI) reduces it to less soluble forms yielding the precipitation of insoluble uranium phases and effective immobilization[117]. Hence, many strategies are being developed to immobilize uranium by reduction. These include the abiotic reactive barriers charged with reductants such as Fe(0), as well as the use of dissimilatory metal reducing bacteria[118-121].

Another factor complicating matters is the pivotal role of uranium complexation. In both the hexavalent and pentavalent oxidation states, the uranyl cation is a linear molecule with five or six available coordination sites in the equatorial plane around the uranium atom[122, 123]. In the tetravalent state, uranium localizes its electrons taking on octahedral or higher (7, 8, or 9) fold coordination[124, 125]. Uranyl is capable of forming strong complexes with oxyanions such as carbonate, filling coordination sites in the equatorial plane. Uranium groundwater speciation is dominated by uranium carbonate complexes when dissolved CO_2 is present[126].

Carbonate has a significant effect on uranium chemistry in the environment by enhancing its solubility proportionally to carbonate concentration[127, 128] and increasing it in systems where no significant hexavalent uranium is present[129, 130]. Except in certain biologic mechanisms[131], carbonate is known to inhibit uranium reduction to U(IV) completely[132]. Even under reducing conditions, uranium can incorporate itself into carbonates or ferric oxides as a hexavalent species[133-136]. From a thermodynamic

standpoint, complexation of U(VI) by carbonate drives its reduction potential to significantly more negative values, eliminating a wide range of otherwise useful target reductant species. Complexation can further modify the ET behavior of a species by modifying the intrinsic electron affinity of a molecule, as well as possibly creating a steric hindrance that impedes the close-approach of a reductant species. Hence, complexation with carbonate affects the driving force for ET as well as the mechanism, and therefore the rate of the reaction. It has been shown that the electrochemical behavior of the uranyl carbonate system is kinetically limited via electrode methods[137]. Those same electrochemical methods have been used to determine the redox potential of the U(VI)/U(V) couple in carbonate solutions: −0.820, −0.760, −0.778, −0.3 vs. SHE[132, 138-140].

Uranium reduction behavior is complicated by the fact that in many studies it has been observed to be influenced strongly by ET kinetics[87, 141]. Homogeneous reduction of U(VI) by Fe(II) in aqueous solution was found to be slow even though partial reduction was predicted to be exothermic; instead it required the presence of solid phases to catalyze the reduction reaction[142, 143]. Yet in most cases the intermediate oxidation state U(V) is short-lived, often consumed quickly by rapid ET in disproportionation reactions[144]. Very little information is available on the chemical conditions controlling uranium ET kinetics in general due in large part to a limited number of reliable techniques for quantitatively identifying U(V)[132, 138, 145, 146]. Rates for the elementary U(VI)-U(V) self-exchange ET reaction are estimated to be slow[147].

While the electronic structure of U(VI) is well understood in solid oxide phases, it is unclear how this structure transforms upon step–wise reduction . U(IV) is found to

have little or no double bonding character of the ligating bonds in solid phase oxides such as UO_2, and pathways to octahedral, or higher, coordination from the linear uranyl molecule as a result of step-wise reduction of U(VI) are unknown. As will be shown in this study, the later stages of this process may involve protonation of axial oxygen atoms during the conversion from U(V) to U(IV). However, we will show below that for triscarbonato uranyl that this second ET step is thermodynamically uphill. Therefore the rate for the second ET step is not relevant here. Proton-coupled electron transfer (PCET) is an important aspect in the ET chemistry of many systems including, as will be demonstrated here, U(VI) to U(V) ET. As such, in part of this study we examine the role PCET mechanisms play in determining the ET rate. Although PCET is a very underdeveloped topic in geochemical systems, we note here that this aspect for the uranium system may demonstrate a possible tie between the ET behavior and solution conditions such as pH, a link that has been given very little previous attention in the uranium literature[87, 148].

In this study we present a detailed, theoretical analysis of the homogeneous ET behavior of uranyl carbonate in aqueous solution, specifically for the case where the reductant is Fe(II). The theoretical apparatus is based on Marcus' two-state ET model. The computational approaches involve the use of molecular dynamics (MD) simulations and Hartree-Fock (HF) and Density Functional Theory (DFT) molecular orbital calculations. The focus is to compute the step-wise ET kinetics for the reduction of triscarbonato U(VI) by two Fe(II) atoms. MD simulations are used to model the interaction between aqueous Fe(II) and triscarbonato U(VI). Predictions for the structure and thermodynamic stability of the ensuing ET encounter complex are given. While no

thermodynamic stability data for this particular complex is available to our knowledge, triscarbonato uranyl is known to form a strong complex with two Ca cations [117, 149]. Therefore it is likely that the complex with two divalent iron cations is similarly stable. Here will show this to be the case using MD simulations. Then we apply ab initio calculations to the computation of the two ET rates for step-wise intramolecular reduction of U(VI) by the two Fe(II) atoms. We compute the driving forces, reorganization energies, and electronic coupling matrix elements that enter into Marcus' ET model. This approach aims to determine a fundamental understanding of the kinetic behavior for uranium reduction by ferrous iron in the presence of carbonate.

2.1 Electron Transfer Model

The applied ET model is very similar to that reported by Rosso et al. in several earlier studies involving Fe(II/III) ET[109, 150-152]. For additional details, the reader is referred to those studies and to standard texts and reviews of modern ET theory. Primary categories of reactions in the current system are encounter complex formation, ET, and PCET. Because the relevant initial oxidation states in the encounter complex are two Fe(II) atoms and one U(VI) atom, we will use II/II/VI to denote the initial electronic configuration: Fe(II)/Fe(II)/U(VI), II/III/V for the intermediate configuration after the first ET step, and III/III/IV for the final configuration after the second ET step.

In all cases the iron atoms are treated as having a high-spin electronic configuration, such that Fe(II) is always in a $t_{2g}^4 e_g^2$ d^6 state, and Fe(III) is always in a $t_{2g}^3 e_g^2$ d^5 state. The majority electron spins on the two iron atoms were taken as spin-parallel (ferromagnetic), with the minority spin on each iron atom comprising the donor

electrons for the two ET reactions. Because these minority spin electrons each go into an empty U 5*f* orbital[153,154,155], the total spin multiplicity is preserved through ET (spin multiplicity = 9), hence the ET reactions are 'spin-allowed', which is a requirement in modern ET theory[156].

For each ET step, within the encounter complex, we utilize the approach outlined by Marcus[85] based on two diabatic ET states ψ_A and ψ_B. The state ψ_A corresponds to the electronic state of the ET 'reactants', and ψ_B corresponds to the electronic state of the ET 'products' (Fig. 1). Hence, for the first ET step, ψ_A is the II/II/VI state and ψ_B is the II/III/V state. For the second ET step ψ_A is the II/III/V state and ψ_B is the III/III/IV state.

ET is a Franck-Condon process, which means that ET is instantaneous relative to the rate of motion of nuclei. The potential energies of the three electronic states can be viewed as having approximately quadratic dependence on nuclear coordinates in the encounter complex, which we will refer to as the internal coordinates, and in the surrounding solvent water, which we will refer to as the external coordinates. For any of the three electronic states, at equilibrium their energies correspond to minima in their respective potential energy surfaces. Thermally promoted fluctuations in the nuclear coordinates can lead to nuclear configurations for which the energies of states ψ_A and ψ_B are equal, the condition required for ET to occur. This coincidence condition corresponds to a crossing point between two potential energy surfaces (Fig. II-1).

The height of the barrier at the crossing point is the diabatic activation energy ($\Delta G^{*\prime}$) for ET. For potential energy surfaces that are similarly parabolic with respect to the nuclear coordinates, the diabatic activation energy is related in a simple fashion to the

reorganization energy (λ) and the thermodynamic driving force for the ET step (ΔG^{o}) as given by

$$\Delta G^{*'} = \frac{(\lambda + \Delta G^{\circ})^2}{4\lambda} \quad (1)$$

The latter term, ΔG^{o}, is the free energy difference between the energies of the reactants and products in their equilibrium nuclear configurations (Fig. II-1). The reorganization energy is the energy to distort the reactants nuclear configuration into the products nuclear configuration without having moved the electron (Fig. II-1). It is comprised of two main contributions, one from distortion of bonds in the ET encounter complex, the internal part λ_I, and another from changing the polarization of the surrounding solvent, the external part λ_E.

Electronic interaction within the encounter complex between the donor and acceptor, such as that arising from superexchange interaction through bridging ligands, reduces the activation energy to ΔG^* (Fig. II-1). This effect is captured by the electronic coupling matrix element (V_{AB}), which is the interaction integral in a two-by-two configuration interaction problem for ψ_A and ψ_B at the crossing-point. V_{AB} effectively 'smoothes' the intersection region, reducing $\Delta G^{*\prime}$ by the amount equal to V_{AB}, which gives the adiabatic barrier height ΔG^*.

In the following section, we outline our methods for the calculation of, among other things, the reorganization energy, the electronic coupling matrix element, and the driving force for each ET step.

3. COMPUTATIONAL METHODS

3.1 Molecular Dynamics Simulations

All of the MD simulations presented in this paper were performed using the computer code DL_POLY[157]. These calculations are based on the Born model of solids[158]. In this model, atoms are represented as point-charge particles which interact via long-range Coulombic forces and short-range interactions. The latter are described by parameterized functions and include a representation of the electron cloud repulsion, van der Waals attraction, and, where appropriate, many-body terms such as an angle-dependent term reproducing covalent effects in the carbonate anion.

Our model also accounts for the polarizability of anions by means of a mechanical shell model which was first introduced by Dick and Overhauser[159]. In this model, a polarizable ion consists of two particles, a core and a shell, which are linked by a harmonic spring. All the simulations were performed in the NPT ensemble (constant number of particles, constant pressure, and constant temperature) and NVE ensemble (constant number of particles, constant volume, and constant energy) at 300 K and zero pressure. The Nosé-Hoover thermostat [160] and the Hoover barostat[160, 161] kept temperature and pressure constant with parameters for a relaxation time of 0.5 ps. The Ewald summation method[162] was used to calculate electrostatic forces. An 8 Å cutoff was used for the short-range interactions, and the real part of the Ewald sum. The Verlet Leapfrog algorithm was used to integrate the equations of motion with a time step of 0.2 fs. The shells were given a mass of 0.2 a.u., their motion treated as that of the cores, following the adiabatic shell model first introduced by Mitchell and Fincham[163].

The potential-based molecular dynamics approach relies upon the quality of the potential set employed; however, in most cases, we made use of previously tested potential parameters and where this was not possible, new or modified potential parameters were validated against relevant experimental and theoretical data. The intra- and intermolecular interactions of water were described by the shell model of de Leeuw and Parker[164] with the modified hydrogen bond potential of Kerisit and Parker[165]. The atomic charges and the potential parameters used to model the uranyl ion were taken from Guilbaud and Wipff[166, 167]. In addition, we converted this model to a polarizable model by adding shells on the uranyl oxygens. The core-shell spring constant was that of Lewis and Catlow[168]. The potential parameters for the water-uranyl interactions were based on those of Guilbaud and Wipff[166, 167]. The shell model version of the Guilbaud and Wipff uranyl model gives good agreement with theoretical and experimental characterizations of water coordination to the uranium ion in aqueous solution and the water cavity around uranyl oxygen ions as described by Hagberg et al.[169](see Supporting Information). The atomic charges, core-shell spring constant, and potential parameters employed for the carbonate molecule were derived by Pavese et al.[170] and have been used many times successfully, principally to model calcium carbonate minerals[165, 171-173] but also carbonate ions in aqueous solution[174]. This model has been used in combination with the de Leeuw and Parker water model on many occasions[165, 171, 174].

The uranium-carbonate oxygen potential was taken to be the same as the uranium-water oxygen potential. Furthermore, a four-body potential was added to keep the six carbonate oxygens, which are directly coordinated to the uranium ion, in the same plane during an energy minimization of the gas-phase triscarbonato uranyl complex. Many

times this was found to be the most stable configuration of the triscarbonato uranyl complex[175-177]. The predicted structures of the triscarbonato uranyl complex in the gas-phase and in solution compare well with experimental and theoretical values (see Supporting Information). The potential parameters for the interactions between iron(II) and water were based on the iron-water potential of Curtiss *et al.* [178] and have been described previously[62]. This potential was modified to be compatible with the water model used in this work. Finally, the iron(II)-carbonate oxygen potential was based on the iron(II)-oxygen potential of Lewis and Catlow[168] and modified to give a good estimate of the lattice parameters of siderite ($FeCO_3$) and its bulk modulus (see Supporting Information). All the potential parameters used in this work are reported in Table 1 of the Supporting Information.

3.2 Quantum Mechanical Calculations

The MD simulations predicted the most stable structure and composition for the encounter complex in the II/II/VI electronic state. The predicted composition was $[Fe(II)Fe(II)U(VI)O_2(CO_3)_3(H_2O)_8]^0$. Two coordinating sites in the six-fold coordination spheres of the two Fe atoms were occupied by carbonate oxygen atoms. The remaining Fe coordination sites were occupied by water oxygen atoms. The goal of the quantum mechanical calculations was to predict the minimum energy structures for this complex in the II/II/VI, II/III/V, and III/III/IV electronic configurations at the DFT level of theory. We used the code NWChem[179] for these calculations. In each of the three electronic configurations, the total charge on the cluster is zero. We performed the energy minimizations on each cluster in the gas-phase using the three-parameter hybrid HF/DFT exchange-correlation functional B3LYP[10, 180].

As mentioned previously, Fe(II) and Fe(III) atoms have high-spin d^6 and d^5 ground-states, respectively[181]. UO_2^{2+} has a closed-shell singlet ground state with 12 valence electrons originating in the O 2*p*, and U 5*f*, 6*d* and 7*s* atomic orbitals[153]. UO_2^{+} has a doublet ground-state with the additional electron occupying a U 5*f* orbital. UO_2 has a triplet ground-state in solid-phase UO_2 with two singly occupied U 5*f* orbitals. We optimized the II/II/VI, II/III/V, and III/III/IV configurations with a total spin multiplicity of 9, consistent with the transfer of iron atom minority spin electrons to open U 5*f* orbitals. The majority spins on the iron atoms have been assumed to align parallel.

We pre-optimized the three structures at the B3LYP level using the 6-31G(d) basis set for H, C, O, and Fe and the LANL2DZ basis set for U for computational expediency. The pre-optimized structures, and their wave functions, were used as the initial guess for final optimizations using a more robust basis set. The final basis set was as follows: 6-311++G(d,p) for H, O, and C, "Ahlrichs TZV" with Hay-Wadt diffuse and polarization functions for Fe, and the Stuttgart relativistic large-core basis set for U[100, 102, 104, 105, 107, 182-185]. Total electronic energy differences from the final optimized structures were used to compute the values of ΔG^{o} for the ET steps, assuming that these differences can be used to approximate the Gibbs free energy differences.

For each of the two ET steps, it is important to be able to predict the nuclear configuration at the curve crossing-points. To do this, we used the linear synchronous transit (LST) method to approximate the reaction coordinate. This approximation is reasonably accurate where relatively small nuclear displacements are involved[186], as has been shown for the separate iron[109] and triscarbonato uranyl components of our

system[187]. The LST method assumes that the ET reactants and products geometries can be linearly combined to produce intermediate structures, according to

$$X_n = \varepsilon X_p + (1-\varepsilon)X_r \,, \tag{2}$$

where X represents a set of nuclear coordinates for the reactants (r), and products (p), and their linear mixture (n), and ε is the mixing parameter that refers to the extent of progress along the reaction pathway. As was done for the equilibrium configurations, a spin multiplicity of 9 was used to compute the wave functions for the intermediate configurations by the LST method.

We used the quasi-diabatic method described by Farazdel et al.[108] to compute V_{AB}, as implemented in NWChem[179]. At the intersection, the splitting can be obtained by solving the secular equation

$$\begin{vmatrix} H_{AA} - E & H_{AB} - ES_{AB} \\ H_{AB} - ES_{AB} & H_{BB} - E \end{vmatrix} = 0 \,, \tag{3}$$

where $H_{ij} = \langle \psi_i | H | \psi_j \rangle$ and *i* and *j* are equal to A or B, H is the total electronic Hamiltonian, $S_{AB} = \langle \psi_A | \psi_B \rangle$, and E is the energy eigenvalue. The two roots of the secular equation give the upper and lower adiabatic surfaces (Fig. II-1). The energy difference between the two adiabatic surfaces at the crossing point is computed as

$$2V_{AB} = (1 - S_{AB}^2)^{-1} [¼(H_{AA} - H_{BB})^2 - (H_{AA} + H_{BB})H_{AB}S_{AB} + H_{AA}H_{BB}S_{AB}^2 + H_{AB}^2]^{½} . \quad (4)$$

For computation of λ, we took advantage of the separability of the internal and external parts. The internal part was computed using the 'direct' method described in Rosso et al. (2003)[150]. This involves calculating the energy of the products electronic state in the nuclear configuration of the reactants, the so-called 'charge-reversed' (excited-state) condition. However, in the current case, the appropriate wave functions for the 'charge-reversed' state could not be obtained; in practice, B3LYP seems to overestimate the delocalization of the electron, perhaps owing to the self-interaction error[188-193]. This made it difficult to obtain the pure products state in the reactants nuclear configuration, and vice versa. Attempts to obtain converged wave functions in the charge-reversed state often converged to the ground-state instead. So to approximate the diabatic surfaces, we fit parabolas through the minima in the DFT potential energy surfaces and estimated diabatic crossing-points as $\Delta G^* + V_{AB}$ where ΔG^* is the adiabatic crossing-point barrier height computed using DFT. We used these fit surfaces to estimate λ_I (Fig. II-1).

The external reorganization energy (λ_E) was computed using Marcus' continuum expression, which gives[110]

$$\lambda_E = (\Delta e)^2(1/2r_1 + 1/2r_2 - 1/r)(1/d_{op} - 1/d_{stat}) , \quad (5)$$

where r_1 and r_2 are radii for the donor and acceptor cavities, r is the distance between their centers, d_{op} is the optical dielectric constant (taken as 1.77 for water), and d_{stat} is the static dielectric constant (taken as 78.39 for water)[194]. Values of r were taken from the final optimized structures. Cavity radii were chosen by averaging the computed lengths of M-O bonds. We took the average of the λ_E values for both products and reactants evaluated at the adiabatic crossing point (Fig. II-1).

Given the computed values of ΔG^o (taken as $\sim\Delta E$), λ, and V_{AB} from the quantum mechanical calculations, first order ET rate constants were computed using

$$k_{et} = \nu_n \exp[-((\Delta G^o+\lambda)^2/4\lambda - V_{AB})/kT] \quad (6)$$

where ν_n is taken as a typical M-O stretching frequency 10^{13} s^{-1} [181]. This equation assumes adiabatic behavior, which is justified given the computed values of V_{AB} we will present below. It also assumes nuclear tunneling effects are negligible, a reasonable assumption at ambient temperature[195, 196].

4. RESULTS AND DISCUSSION

4.1 Encounter Complex Formation

We first equilibrated the triscarbonato uranyl complex in a cubic box containing 247 water molecules for 200 ps in the NPT ensemble. Then, an Fe(II) atom was introduced by replacing a water molecule in the vicinity of the triscarbonato uranyl complex and the system was equilibrated for 200 ps in the same conditions. We then carried out a series of independent molecular dynamics simulations in the microcanonical

ensemble (NVE) to determine the potential of mean force of the Fe(II)-triscarbonato uranyl ion pair.

In each calculation the distance between the centers of mass of the iron atom and triscarbonato uranyl complex was kept fixed. This means that we make the assumption that the reaction coordinate for the association process is the vector defined by the two centers of mass. As the triscarbonato uranyl complex can rotate with respect to the centers of mass vector, our choice of reaction coordinate is an approximation, which could result in the energy barriers being misrepresented slightly. However, this approach is sufficient to identify the preferred association sites, and compute the free energy change of the overall association process. This energy change is obtained by integrating the average force required to keep the two species at each set distance from the maximum separation to the point of interest.

A total of thirty calculations were performed to obtain points between 3.4 and 9.2 Å. In each calculation, the system is equilibrated for 2 ps and the average force collected over 100 ps. The potential of mean force is shown in Figure II-2. In the region between 9.2 and 8.6 Å, the hydration shells of the two species are complete, and there is some hydrogen bonding between the two shells. As the two species approach closer than 8.6 Å, a water molecule of the triscarbonato uranyl hydration shell is displaced and a water molecule from the iron hydration shell forms a hydrogen bond with a carbonate oxygen. As the two species draw nearer a second hydrogen bond is formed from about 6.8 Å. A minimum in the free energy, shown as "solvent-separated" in Figure II-2 (see Supporting Information for a figure of each complex mentioned in this section), is reached when a third hydrogen bond between a water molecule of the iron hexaaquo complex and a

carbonate oxygen is formed at a distance of 5.5 Å. However, this minimum is shallow, and our calculations suggest that the residence time of iron in this site is likely to be short. From there, there is a small energy barrier (~ 3 kJ/mol) for the hexaaquo iron complex to lose two water molecules and bind to a carbonate group in a bidentate fashion ("1×bidentate" in Figure II-2). According to Figure II-2, this is not a minimum in free energy but a short flattening of the curve. However, this might be due to our choice of the reaction coordinate. There is a strong driving force for the iron atom to then move to a position where it is coordinated to two oxygen atoms from two separate carbonate groups at a distance of about 3.6 Å, labeled "2×monodentate" in Figure II-2. In addition, the large energy barrier for dissociation suggests that the iron residence time at this site is remarkably long. The free energy change of the overall process is calculated, from the potential of mean force at 3.6 Å, to be −95 ± 6 kJ/mol. The error bars in Figure II-2 were estimated by calculating the standard deviation of the mean when the simulation was divided into 5 blocks. Furthermore, the overall interaction energy change can be computed from the difference in energy between the simulations at 9.2 and 3.6 Å and is found to be −157 ± 8 kJ/mol. Therefore, assuming that the interaction energy change is a good approximation for the enthalpy change, our calculations suggest a significant entropic contribution (about 60 kJ/mol) to the free energy change for complex formation.

There is a second possible route for the iron atom to attach at the 2×monodentate site. Rather than forming a third hydrogen bond the hexaaquo iron complex can lose a water molecule to bind directly to a carbonate oxygen atom that is not coordinated to the uranium ion, "1×monodentate" in Figure II-2. This minimum is relatively shallow too, and hence we expect this configuration of the complex to have a similar lifetime than that

of the solvent-separated ion pair. The small difference in free energy between the two routes for distances shorter than 5.0 Å is due to uncertainties. To conclude, the potential of mean force clearly shows that the 2×monodentate site is the most energetically favored site and is kinetically stable.

In order to give some approximation of the lifetime of iron in the association sites mentioned above, we carried out two MD simulations whereby the iron atom was initially positioned either at the 1×monodentate or at the solvent-separated site. Both simulations were run for 200 ps. Figures II-3a and b show the distance between the iron atom and three of the carbonate oxygen atoms for the first 60 ps of each simulation. In the first simulation (Figure II-3a), the iron atom escaped from the 1×monodentate site after 20 ps to bind to a second oxygen of the same carbonate group. After residing in this site for another 15 ps, it then moved again to bind at the 2×monodentate site where it stayed for the remaining of the simulation. In the second simulation (Figure II-3b), the iron atom first resided for about 15 ps at the solvent-separated site and then moved to the 1×bidentate site for 25 ps. Finally, it moved to the 2×monodentate site where it stayed for the remaining of the simulation. Although we cannot compute precise average residence times from so few events, these calculations show that the residence time of iron in the solvent-separated, 1×monodentate, and 1×bidentate sites is short and on the order of a few tens of picoseconds. In summary, these calculations confirm the main conclusion drawn from the potential of mean force: the 2×monodentate site is clearly the most favorable association site, and that iron and triscarbonato uranyl can form a very stable ternary complex.

Finally, we investigated the association of the iron triscarbonato uranyl complex with a second iron atom. We did not compute a second potential of mean force, as it was not expected to be significantly different. However, we calculated the energy change due to the second iron associating at the 2×monodentate site from three separate molecular dynamics calculations, namely that of Fe(II), $[FeUO_2(CO_3)_3]^{2-}$, and $[Fe_2UO_2(CO_3)_3]$ in solution. The energy change is reduced to -119 ± 21 kJ/mol. Although the energy change has slightly decreased, it is still large and negative, which strongly suggests that the association of an additional iron atom will result in the formation of a stable species.

4.2 Equilibrium Structures and Energies

Given the predictions of the MD simulations, we were led to conclude that the 2×monodentate docking structure was most appropriate for each of the two Fe(II) atoms complexing the triscarbonato uranyl molecule. This gave the final encounter complex a composition of $[Fe_2UO_2(CO_3)_3(H_2O)_8]^0$. This cluster then became the focal point of our intramolecular ET kinetic calculations performed using DFT. The initial goals of the DFT calculations were to 1) find minimum energy structures for the II/II/VI, the II/III/V, and the III/III/IV electronic configurations, 2) determine the relative energies of these electronic configurations, and 3) from these relative energies, infer pathways for ET. Here we first discuss structural details of the optimized clusters in the II/II/VI, II/III/V, and the III/III/IV electronic configurations.

Table II-1 lists selected structural parameters for the II/II/VI, II/III/V, and III/III/IV electronic configurations optimized using DFT. The initial energy minimization was performed on the II/II/VI electronic configuration, starting from a

nuclear configuration derived from the MD simulations. The iron atoms are bonded to two oxygens from two separate carbonates ("2×monodentate"), and the remaining four coordination sites on each of the two iron atoms are occupied by water molecules. The optimized geometry for the II/II/VI configuration consists of nearly the same bonding topology as suggested by the MD simulations, although the lack of hydrogen bonding to surrounding bulk water in quantum mechanical calculation leads to some subtle differences. The coordination of the uranium atom in the equatorial plane is five-fold, consisting of two pairs of oxygen atoms from two carbonate ligands, and the fifth equatorial oxygen atom is from the third carbonate ligand (Fig. II-4). This third carbonate ligand bridges the two coordination spheres of the iron atoms. These aspects are the same between the MD and DFT predictions (see Supporting Information). However, in the DFT calculations, an oxygen atom on the third carbonate ligand is the acceptor site of a proton transfer (PT), transforming it into a bicarbonate ligand; the proton originates from a nearby water molecule attached to an iron atom during the energy minimization process (Fig. II-4). Also, the planarity of the equatorial carbonates is slightly broken in the DFT calculation. Both the intramolecular proton transfer and the decrease in the planarity of the carbonate ring may arise from the gas-phase treatment in the DFT calculation. It is possible that inclusion of a polarizable continuum model (PCM) to describe the remaining absent solvent would have changed the propensity for the proton transfer to occur. However, we expect it to be of little consequence to the computed ET rate parameters such as the reorganization energies and electronic coupling matrix elements in this system due to the peripheral nature of the proton transfer. Use of a PCM model was also found to be computationally unwieldy.

Starting from the II/II/VI optimized structure, energy minimization of the II/III/V electronic configuration yields a structure that differs in four main respects (the initial asymmetry, specifically the OH ligand, determined which iron would oxidize when the electronic configuration was changed). First, one of the five equatorial U-OCO_2 bonds extends by 0.43 Å to 2.78 Å (Table II-1), effectively reducing the number of equatorial oxygen atoms to four, accompanied by slight adjustment of the other two carbonate ligand positions. Second, the average Fe-O bond distance decreases for the oxidized iron atom, as expected from the smaller ionic radius of Fe(III) relative to Fe(II). Third, the average U-O distance increases in accordance with the change in the oxidation state of the uranium atom from U(VI) to U(V). And fourth, a proton from a water ligand on the Fe(III) atom transfers to an oxygen atom on a carbonate ligand that bridges the Fe(III) atom to the U(V) atom (Fig. II-5). This is the second water molecule to undergo dissociation in the same iron solvation shell, in agreement with the tendency of Fe(III) to more readily hydrolyze than Fe(II)[181]. Hence, the comparison of the minimum energy structures for the II/II/VI and II/III/V configurations suggests that the first ET step is accompanied by an intramolecular PT that takes place between a water molecule of the first solvation shell of an iron atom and the carbonate ring.

For the III/III/IV configuration, two main features were found in this optimized structure. First, two protons, one from water ligands of each iron atom, transfer to the axial oxygen atoms of the central uranium cation (Fig. II-6). A second observation regarding this structure is that the coordination on one of the Fe atoms is reduced from six to five. This is a result of re-coordination of the third carbonate with the uranium; it might not have occurred if additional explicit waters of solvation were present.

In their minimum energy nuclear configurations, the computed energy difference for the first ET step (II/II/VI → II/III/V) is −30.4 kJ/mol, and for the second step (II/III/V → III/III/IV) it is +13.9 kJ/mol at the DFT level of theory. Assuming that the total electronic energy differences are reasonable estimates for the free energy differences, the calculations suggest that the III/III/IV configuration is energetically unfavorable relative to the II/III/V configuration and therefore the III/III/IV configuration will not be an end-product of ET in this system. In other words, we find that the II/III/V is the most stable electronic configuration in this ternary complex. This result is consistent with the well-established finding from experiment that the stability of U(V) is substantially enhanced by carbonate complexation of the uranyl cation[15,21,22]. Therefore, with respect to the reduction rate of U(VI) in this complex, the ET rate of primary importance is the first step, which is accompanied by a single PT.

4.3 Electron Transfer Pathways

To predict the kinetics of the first ET step, we need to compute the height of the ET barrier. This requires that we have an accurate nuclear configuration for the transition state. In the past we have had success using the LST approach to approximate the transition state structure for ET[197-199], and we apply this approach here. However, in this case, the DFT calculations just described suggest two possible pathways for the II/II/VI → II/III/V conversion. The first is a sequential ET/PT pathway, where ET is followed by PT, or vice versa. The second is a concerted ET/PT, where the transfers occur simultaneously. Both pathways fall under the general category of PCET. In his recent review on this topic, Mayer[200] outlines the distinction between the two pathways as

arising from whether or not a reaction intermediate must be invoked; i.e. an intermediate structure or reaction between the ET and PT. Concerted PCET is considered as not requiring an intermediate, but also does not require that the ET and PT occur simultaneously. Here we evaluate the barriers for both the sequential and concerted PCET pathways for the II/II/VI → II/III/V step, where again the ET is the transfer of an electron from the Fe(II) atom to the U(VI) atom and the PT is the transfer of a proton from a first shell water molecule to a carbonate ligand. We define the sequential pathway (hereafter $PCET_{seq}$) as the ET step followed by the PT step, with the ordering arising from the finding that the ET should be slower than the PT in this case and therefore is more likely to be rate-limiting for the sequence. We define the concerted pathway (hereafter $PCET_{con}$) as the ET and the PT occurring simultaneously.

By applying the LST approach to the optimized structures of the II/II/VI and II/III/V configurations, the potential energy surfaces for both PCET pathways can be estimated. Given the values computed for the electronic coupling matrix element, discussed below, we find that both PCET pathways fall within the adiabatic regime. Thus the potential energy surface on which the PCET reaction evolves is the adiabatic surface (Fig. II-7). For the $PCET_{con}$, the barrier maximum is located at an energy of 109.6 kJ/mol above the equilibrium energy of the II/II/VI configuration, and at a mixing parameter value of ~ 0.4 on the reaction coordinate (Fig. II-7a). Thus the $PCET_{con}$ is characterized by an adiabatic barrier height of +109.6 kJ/mol (relative to the potential energy of the reactants) and a driving force of −30.4 kJ/mol.

For the $PCET_{seq}$ pathway, we require an additional energy-minimized structure, which is the one in the II/III/V electronic configuration except without the accompanying

PT. To achieve this, we ran an energy minimization equivalent to the others starting from the optimized structure for the II/II/VI electronic configuration, except with the O-H distances fixed. We refer to this configuration as the II/III/V_{int}, where 'int' indicates intermediate. Selected structural details for this energy minimized structure are listed in Table II-1. In its equilibrium nuclear configuration, the energy of II/III/V_{int} was found to lie +6.9 kJ/mol higher in energy than the equilibrium energy for the II/II/VI configuration. Therefore, this is the energetic location for the intermediate in the $PCET_{seq}$ pathway. Application of the LST method to the ET step and separately to the PT step yields barrier heights of +51.0 kJ/mol relative to the II/II/VI configuration (for the ET step), and +24.2 kJ/mol relative to the II/III/V_{int} configuration (for the PT step). Thus the adiabatic potential energy surface for the $PCET_{seq}$ pathway is comprised of two barriers (Fig. II-7b), with the barrier for the ET step approximately twice as large as the barrier for the PT step.

4.4 Electronic Coupling

The electronic coupling at the crossing points for both the concerted and sequential PCET's is of interest for determining whether or not the ET components of these reactions fall under the adiabatic or non-adiabatic (also called 'diabatic') regimes. For the non-adiabatic regime, passage through the crossing-point does not necessarily lead to the ET products being formed, with the transition probability depending on the square of V_{AB}. For the adiabatic regime, the system evolves on an adiabatic potential energy surface resembling a double-well potential and the transition probability at the crossing-point is treated as 100%, independent of V_{AB}. Using the methods outlined

above, we compute V_{AB} values using HF wave functions at the crossing-point geometries derived using DFT. We do this because the DFT treatment leads to partial electron delocalization near the crossing-point regions, as is self-evident in the potential energy surfaces shown in Figure II-7, and therefore the diabatic states are not accessible in the DFT approach. For the crossing-point in the $PCET_{con}$, we compute V_{AB} = 85.8 kJ/mol, and for the crossing-point in the $PCET_{seq}$, we compute V_{AB} = 6.8 kJ/mol. Both values are above the typical room temperature adiabaticity criterion of 2.4 kJ/mol[201], which means that both forms of PCET can be treated as adiabatic.

4.5 Reorganization Energy

The above analysis indicates that both forms of PCET for the II/II/VI → II/III/V ET process are adiabatic. Therefore the ET rate can be determined directly from the potential energy surfaces simply by knowing the barrier height. However, because of the methodological approach taken, this would ignore the possibility that the external reorganization energy could be significant relative to the internal reorganization energy, and thereby modify the barrier height. Therefore it is of interest to evaluate both λ_I and λ_E, quantities related to the diabatic potential energy surfaces, to estimate the magnitude of this effect. As described in the Methods section, we approximated the diabatic potential energy surfaces by fitting quadratic functions to energetic minima and diabatic barriers estimated as the adiabatic barrier height plus V_{AB} (Fig. II-7). This allowed an estimate of λ_I, to which we added the value for λ_E computed using Marcus' continuum equation.

Values of λ_I computed using the DFT potential energy surfaces in combination with the computed values of V_{AB} are 242.5 kJ/mol (sequential) and 924.1 kJ/mol (concerted). The reorganization energy of the solvent λ_E was calculated to be 144.3 kJ/mol. The total values of λ then becomes 386.8 kJ/mol and 1068.3 kJ/mol respectively. The contribution of the solvent to the reorganization energy, and therefore the barrier height, is clearly significant.

5. OVERALL RATES OF REACTION

The calculated rate for the $PCET_{con}$ pathway is extremely slow, at ~7×10^{-17} s^{-1}, which is effectively zero. The calculated rates for the two-steps within the $PCET_{seq}$ pathway are 6×10^{-1} s^{-1} for the ET step and 9×10^{8} s^{-1} for the subsequent PT step. Hence, the $PCET_{seq}$ pathway is predicted to be overwhelmingly the faster of the two pathways, and therefore sequential PCET is the predicted mechanism. Given the sequential nature of the two elementary steps involved, the slower of the two rates is limiting. Thus we expect that the conversion of hexavalent uranium to pentavalent uranium in the current system occurs only at a rate of about 1 s^{-1}. Clearly the sequential pathway is also the chemically intuitive choice in this case, because the proton that transfers moves from a water ligand to a carbonate ligand, neither of which coincide with the electron donor and acceptor sites Concerted PCET is more likely to involve ET and PT with similar donor and acceptor locations[200].

The question of overall reduction rate (*k*) is important in light of the need to obtain values that can be compared directly with experiment. However, no experimental reduction rates for this system are yet available to our knowledge. A chemist's first

instinct might be to apply an equilibrium approximation for the formation of the encounter complex and assume steady-state as follows: $k = K_{eq}k_{et}[Fe]^2[U]$. However, given the −249 kJ/mol driving force predicted for the formation of the encounter complex, this approach is not appropriate. A more appropriate model[202] would assume that 100% of the available Fe and triscarbonato uranyl would form complexes, resulting in the following expression: $k = k_{et}[M]$ where [M] is the metal with a lower concentration.

Collectively, our analysis leads to the conclusion that the dominant final oxidation state of uranium in this system is pentavalent. Given that it is already well-known that carbonate complexation tends to stabilize pentavalent uranium[132, 138, 187, 203]; our calculations are consistent with this observation. Given, that the II/III/V → III/III/IV ET process was predicted to be strongly endergonic, and that this step apparently is coupled with protonation of the two axial oxygen atoms (complicating the use of the computational approach taken here), we are unable at this time to assess the potential for production of U(IV) and subsequent solid phases in this system. From our analysis, this ET system should steadily progress towards and stabilize primarily pentavalent uranium.

In summary, this study finds that Fe(II) should form stable ternary complexes with triscarbonato U(VI) in aqueous solution, and that within these complexes uranium should be reduced principally to the pentavalent uranium oxidation state. Two ferrous iron atoms are predicted to bind to the three-membered carbonate ring of the uranium-carbonate complex. ET from one of the iron atoms to the central uranium atom is thermodynamically favorable and should occur adiabatically by sequential ET coupled with a proton transfer, with a slow overall rate of ~ 1 s^{-1}. The subsequent reduction of U(V) to U(IV) has a significant thermodynamic barrier. This latter step also appears to

be coupled with the protonation of the axial oxygen atoms, as a possible precursor to the transformation of the uranyl moiety toward seven-fold coordinated U(IV). Thus, a major finding of this study is that pentavalent uranium is predicted to be stabilized in this system, likely on timescales that are amenable for experimental study.

Acknowledgements. MCFW and MAAS are grateful for financial support from NSF-Chemistry through the Center for Environmental Molecular Science at Stony Brook, Award #CHE-0221934 and a supplement that allowed MCFW to take up residence at EMSL to conduct part of this work. KMR and SK acknowledge support from the Stanford Environmental Molecular Sciences Institute, jointly funded by NSF-Chemistry and the U.S. Department of Energy, Office of Biological and Environmental Research. This research was performed in part using the Molecular Science Computing Facility (MSCF) in the William R. Wiley Environmental Molecular Sciences Laboratory (EMSL) at the Pacific Northwest National Laboratory. The MSCF is funded by the Office of Biological and Environmental Research in the U.S. Department of Energy. Pacific Northwest National Laboratory is operated by Battelle for the U.S. Department of Energy under Contract DE-AC06-76RLO 1830.

Supporting Information Available: Table of the potential parameters. Tables comparing the structural parameters of the uranyl ion in aqueous solution, the triscarbonato uranyl complex (both MD and DFT), and siderite mineral obtained in this work with published experimental and theoretical data. Figures of the four iron triscarbonato uranyl complexes shown in Figure II-2. Table showing a comparison of the distances calculated from the potential model and DFT calculations for the II/II/VI iron triscarbonato uranyl complex. This material is available free of charge via the internet at http://pubs.acs.org.

Table II-1: Metal-Oxygen Distances and ET(Fe-U) distances (Å)						
II/II/VI	**Fe1**		**Fe2**		**U**	**Fe1-U**
O_{H2O}	2.344	O_{H2O}	2.302	O_{UO}	1.780	3.864
O_{H2O}	2.220	O_{H2O}	2.113	O_{UO}	1.775	
O_{H2O}	2.163	O_{H2O}	2.200	O_{CO}	2.454	**Fe2-U**
O_{OH}	1.950	O_{H2O}	2.277	O_{CO}	2.362	4.065
O_{CO}	2.761	O_{CO}	2.090	O_{CO}	2.352	
O_{CO}	2.010	O_{CO}	2.018	O_{CO}	2.434	
				O_{CO}	2.493	
Average	**2.241**	**Average**	**2.167**	**average**	**2.236**	
II/III/V	**Fe1**		**Fe2**		**U**	**Fe1-U**
O_{H2O}	2.218	O_{H2O}	2.287	O_{UO}	1.827	3.856
O_{H2O}	2.118	O_{H2O}	2.234	O_{UO}	1.826	
O_{OH}	1.896	O_{H2O}	2.189	O_{CO}	2.486	**Fe2-U**
O_{OH}	1.896	O_{H2O}	2.231	O_{CO}	2.422	3.973
O_{CO}	2.026	O_{CO}	2.070	O_{CO}	2.776	
O_{CO}	2.233	O_{CO}	1.980	O_{CO}	2.557	
				O_{CO}	2.622	
Average	**2.065**	**Average**	**2.165**	**average**	**2.359**	
II/III/V_{int}	**Fe1**		**Fe2**		**U**	**Fe1-U**
O_{H2O}	2.224	O_{H2O}	2.239	O_{UO}	1.833	3.747
O_{H2O}	2.117	O_{H2O}	2.185	O_{UO}	1.827	
O_{H2O}	2.109	O_{H2O}	2.270	O_{CO}	2.486	**Fe2-U**
O_{OH}	1.896	O_{H2O}	2.184	O_{CO}	2.440	4.047
O_{CO}	1.923	O_{CO}	2.132	O_{CO}	2.518	
O_{CO}	2.061	O_{CO}	1.970	O_{CO}	2.530	
				O_{CO}	2.968	
Average	**2.055**	**Average**	**2.202**	**Average**	**2.372**	
III/III/IV	**Fe1**		**Fe2**		**U**	**Fe1-U**
O_{OH}	1.879	O_{H2O}	2.417	O_{UOH}	2.077	4.073
O_{OH}	1.878	O_{H2O}	2.209	O_{UOH}	2.098	
O_{OH}	1.928	O_{H2O}	2.105	O_{CO}	2.437	**Fe2-U**
O_{H2O}	2.342	O_{OH}	1.843	O_{CO}	2.522	3.991
O_{CO}	2.046	O_{CO}	2.001	O_{CO}	2.454	
O_{CO}	3.283	O_{CO}	1.922	O_{CO}	2.537	
				O_{CO}	2.537	
Average	**2.226**	**Average**	**2.083**	**Average**	**2.380**	

Figures

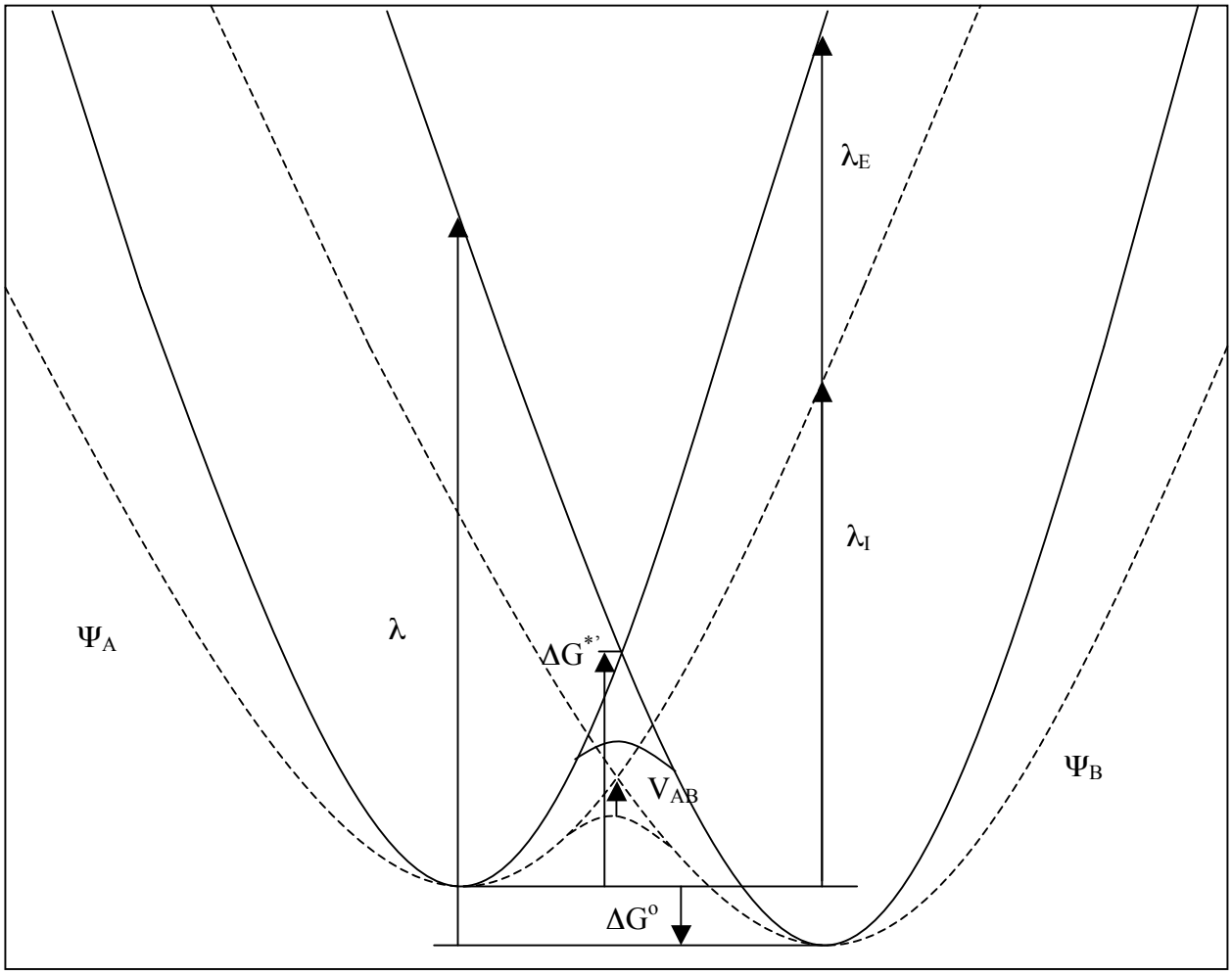

Figure II-1: Diagram showing the specific application of Marcus Theory to this system. Diabatic potential energy surfaces are shown as parabolic functions, separately for both the intrinsic (dashed line) and solvent (solid line) contributions. The thermodynamic free energy is shown as ΔG^o. Since the adiabatic curve does not account for solvent, we added the solvent component to estimate the total diabatic energy barrier, which is represented as the difference between the two horizontal lines in the crossing region.

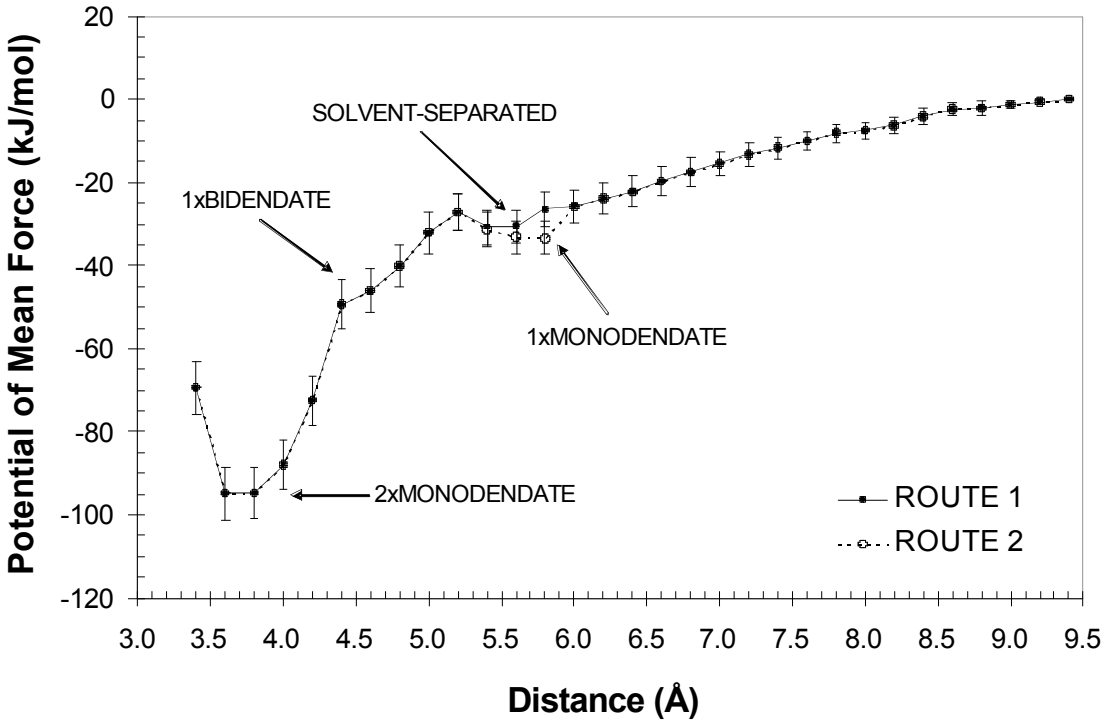

Figure II-2: Potential of mean force of the Fe(II)-triscarbanato uranyl ion pair. Routes 1 and 2 represent two possible association mechanisms. "1×" and "2×" indicate how many carbonate groups are binding the iron atom in a monodentate or bidentate fashion. See text for a more detailed description of the labels and Supporting Information for figures of the complexes.

.

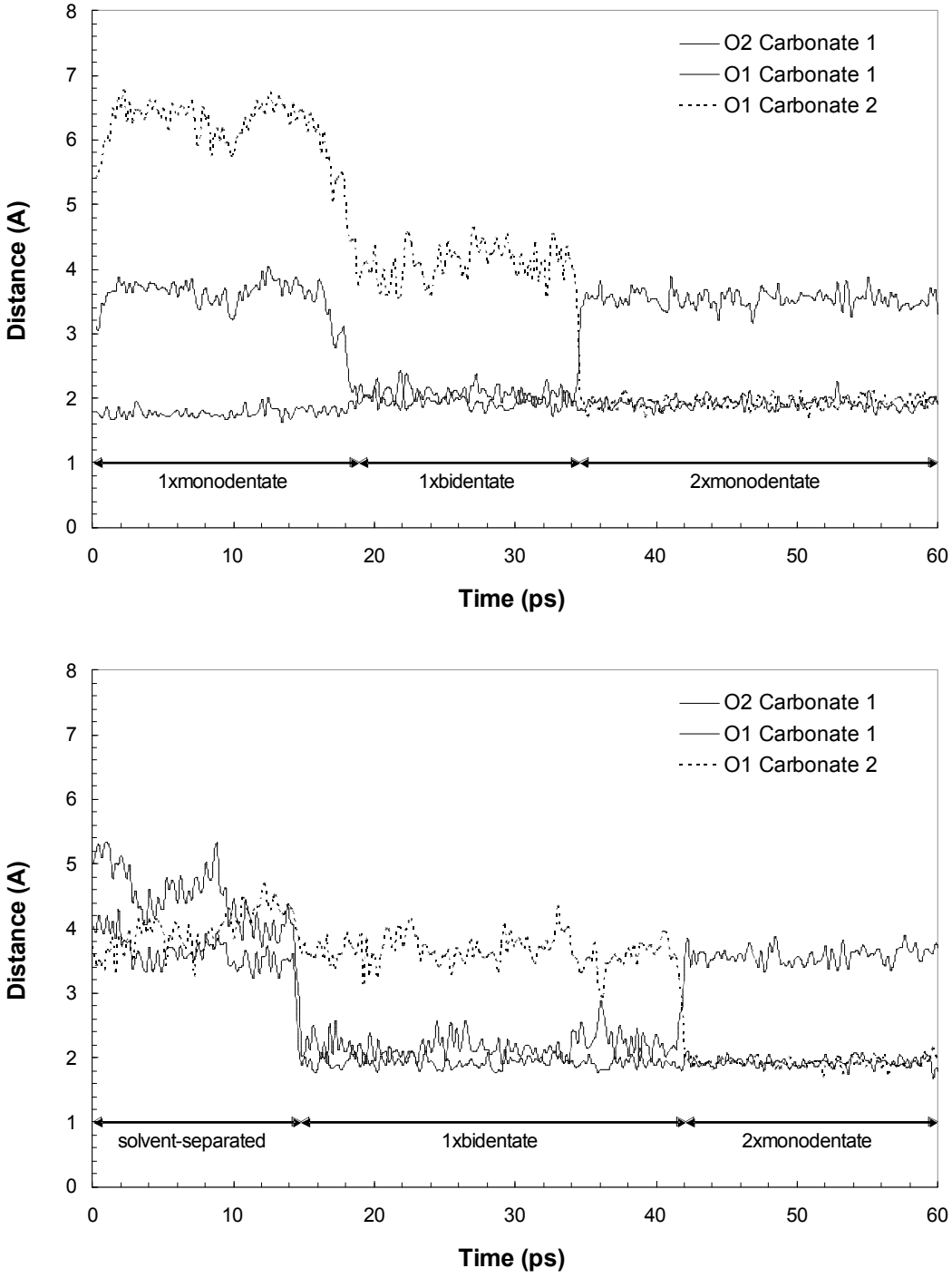

Figure II-3a & b: Graphs showing the distance between iron and three carbonate oxygens in two simulations of $[FeUO_2(CO_3)_3]^{-2}$ in solution. Figure 3a (top) where the iron atom is initially placed at the 1×monodentate site, and Figure 3b (bottom) where the iron is initially placed at the solvent-separated site.

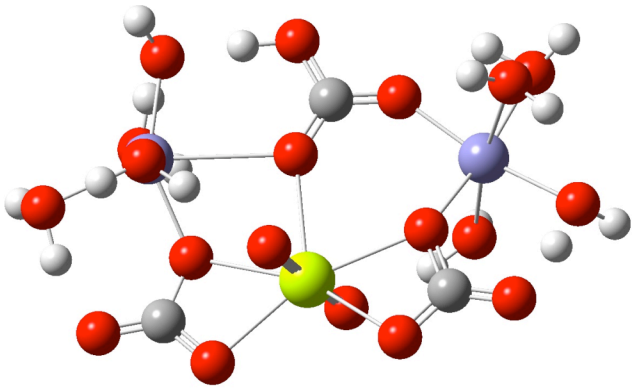

Figure II-4: Diagram of the computed minimum energy structure for the II/II/VI electronic configuration, showing the protonated bridging bicarbonate. The yellow sphere is the uranium atom, red spheres are oxygen atoms, blue spheres are iron atoms, grey spheres are carbon atoms, and white spheres are hydrogen atoms.

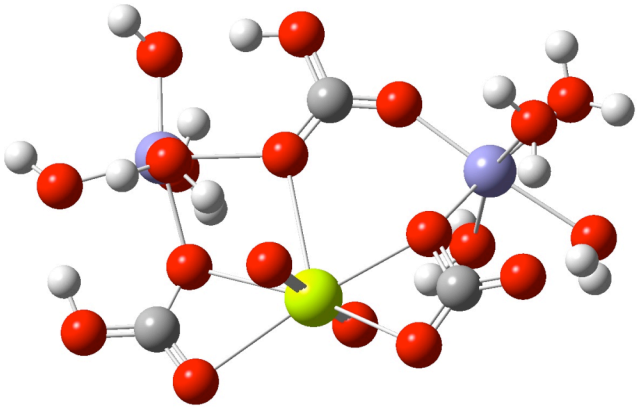

Figure II-5: Diagram of the computed equilibrium structure for the II/III/V electronic configuration. See Figure II-4 caption for atom legend. The monodentate carbonate bond is extended. The protonated carbonate in the upper right is transferred during the II/II/VI → II/III/V ET.

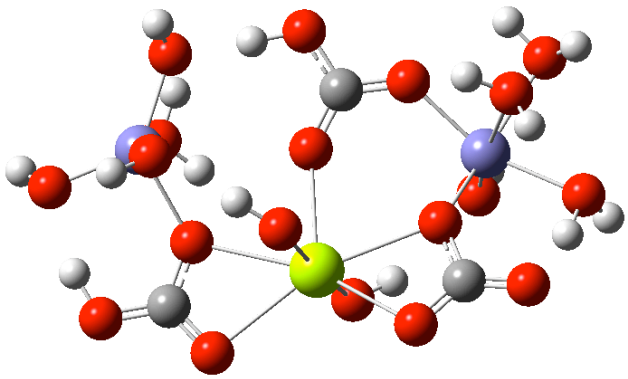

Figure II-6: Diagram showing the computed minimum energy structure of the III/III/IV electronic configuration. See Figure 4 caption for atom legend. Protons have transferred to the axial oxygen atoms on the uranium cation.

Concerted PCET Coordinate for FeFeU(CO $_3)_3(H_2O)_8$ System

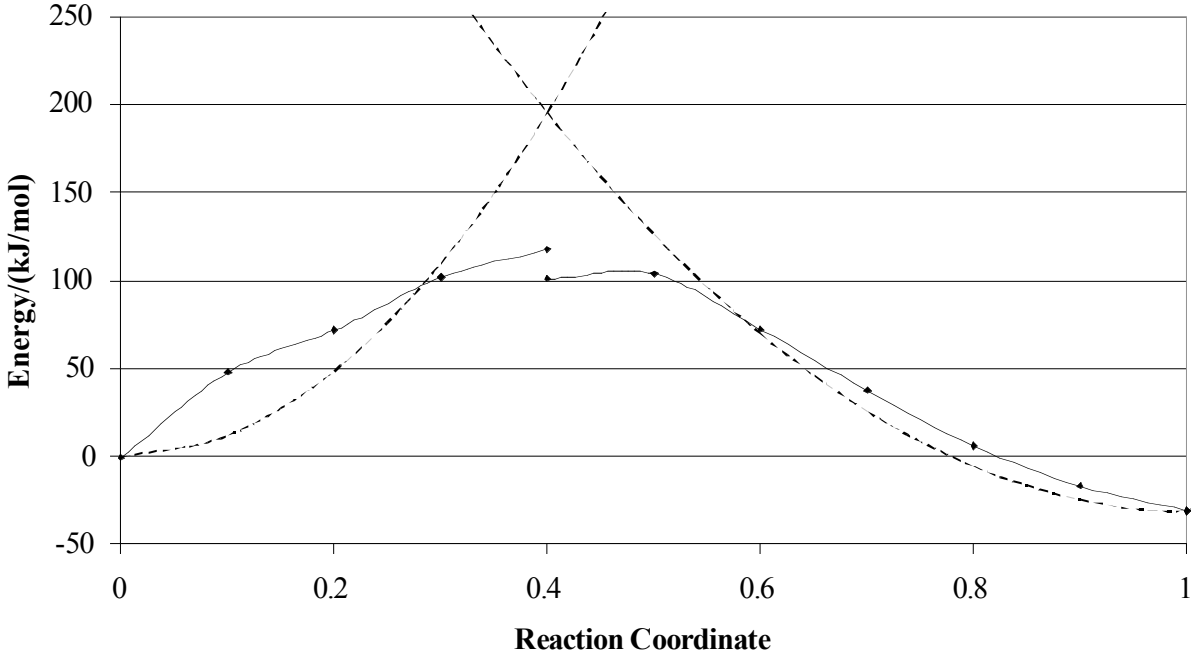

Sequential PCET Coordinate for FeFeU(CO $_3)_3(H_2O)_8$ System

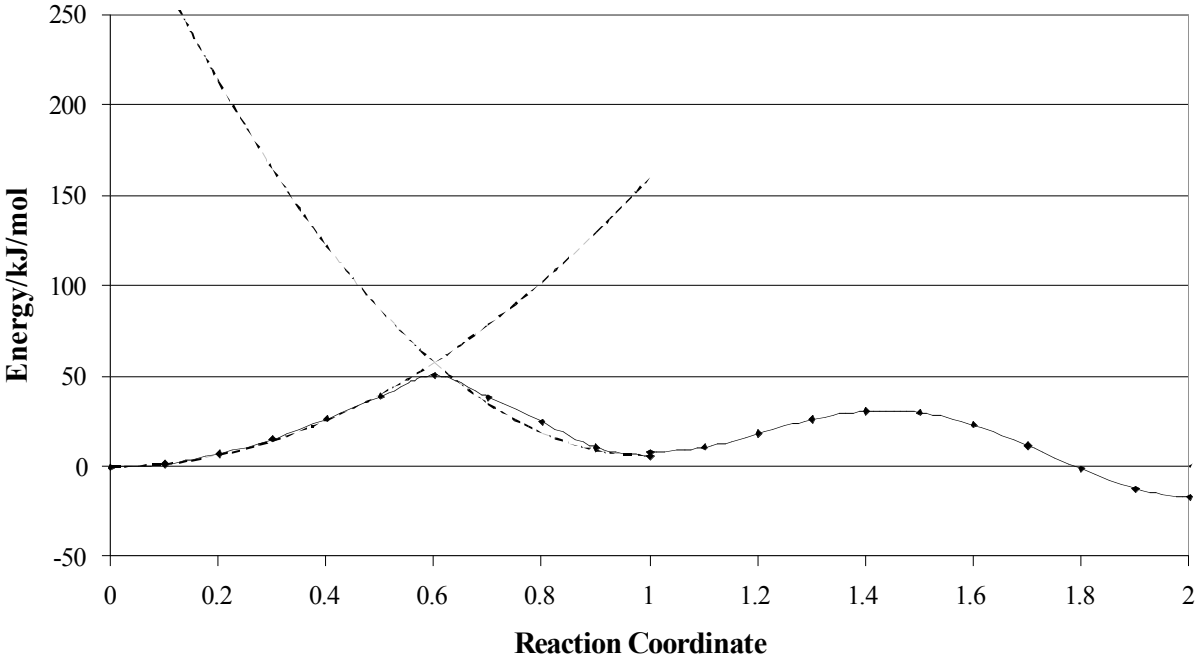

Figure II-7: Adiabatic (solid) and diabatic (dashed) potential energy surfaces for the concerted (upper figure) and sequential (lower figure) proton-coupled electron transfer pathways. The adiabatic curves were computed at the DFT level of theory using a reaction coordinate based on the LST method. The reaction coordinate scales from 0 to 1 for the $PCET_{con}$ pathway. For the $PCET_{seq}$ pathway, the reaction coordinate scales from 0 to 1 for the ET step, and 1 to 2 for the PT step. The diabatic curves were approximated as parabolas passing through the sum of the adiabatic barrier height plus the calculated values of the electronic coupling matrix elements.

The Intrinsic Electric Double Layer at the Oxide-Water Interface

Matthew C. F. Wander[1], and Louise J. Criscenti[2]

[1]CEMS (Center for Environmental Molecular Science), Department of Geosciences, Stony Brook University, Stony Brook, NY 11794

[2]Department of Geochemistry, Sandia National Laboratories, Albuquerque, NM

Abstract In this paper we present a new approach, and results, for calculating the dielectric constant of water above a surface, the (110) face of goethite. Three versions of the surface were made: positively charged, neutral, and negatively charged, representing the goethite surface equilibrated with water at pH 6, 9, and 12 respectively. The simulation cells consisted of one of these three surface slabs overlain by a 36Å layer of water. Classical molecular dynamics simulations were performed for 1 ns at 300^{o}K. For each goethite-water interface, the electrical and structural properties of water were calculated. The calculations show the presence of an electrical double layer at the goethite-water interfaces with clearly defined structured and diffuse layers, and dielectric constants ranging from 45-80. Water formed the classic electric double layer without the presence of any screening ions. This double layer results from hydrogen bonding between water molecules and the (110) surface. The screening of the surface charge was performed by water dipole reorientation at the interface. The work required to bring an ion to the goethite surface is discussed for all three cases.

Introduction

The surfaces of oxides hydroxylate upon exposure to water. Water molecules are attracted to the hydroxide groups on the surface, resulting in a three or more molecule thick layer of interfacial water that has properties different from bulk liquid water[204]. Each oxide has a characteristic point of zero charge (PZC) that is defined as the pH at which the oxide surface is neutral, i.e., the concentration of positively-charged surface sites is equal to the concentration of negatively-charged surface sites in a simple oxide-water system. Surface charge increases as solution pH changes away from the pH_{PZC}[204].

The term "electric double layer" (EDL) was originally coined to describe the arrangement of charges and oriented dipoles constituting the interphase region at the boundary of an electrolyte. The term is a legacy from an early stage in understanding when the interphase was pictured as always consisting of only two layers, or sheets of charge, one positive and the other negative. Double layers are a general consequence of the meeting of two phases at a boundary, and have two fundamental aspects, the electrical aspect and the structural aspect. The electrical aspect concerns the magnitude of the excess-charge densities on each phase. It also concerns the variation of potential with distance from the interface. The structural aspect is a matter of knowing how the particles of the two phases (ions, electrons, dipoles, neutral molecules) are arranged in the interphase region so as to electrify the interface. The charge or potential difference is characteristic of the particular structure and vice versa[205, 206].

The electric double-layer at mineral-water interfaces, including the goethite-water interface, is described by (1) a structured layer that is 4-6 Å thick and consists of water molecules and adsorbed ions oriented according to the surface charge[207], and (2) the

diffuse layer which contains charge-balancing counterions and has a non-zero electric potential. Although the conceptual model for the EDL has always included changes in water structure from the mineral surface into bulk solution, EDL-model equations define the charge distribution and potential from the surface into bulk solution to be a function of only the surface charge and ion distribution in the interfacial region.

Four models of the EDL are shown in Figure III-1[208-213]. These models include: the Helmholtz single layer model, the Gouy-Chapman diffuse layer model, the Stern double layer model, and the triple layer model. Within these four models, two different types of potential behavior as a function of distance are exhibited in these diagrams. The Stern and Helmholtz models assign the distribution of charge at the surface to planes of charge analogous to the planes in a parallel-plane capacitor. The Gouy-Chapman model describes the distribution of charge in the diffuse layer by the exponential decay of the electric potential from the surface into the bulk solution due to a greater concentration of counter-ions close to the surface

$$\Psi_z = \Psi_o \, e^{-\kappa z} \qquad (2)$$

where κ is the debye length, Ψ_o is the potential at the solid surface, z s the distance away from the surface and Ψ_z is the potential at a distance z from the solid surface. In the triple layer model[214], adsorbed ions reside in two planes, the 0-plane and the β-plane; and, the distribution of charge in the diffuse layer, starting at the d-plane, is described by a modified Gouy-Chapman equation. The regions between the 0 and β-planes and the β- and d-planes are characterized by constant capacitances, C_1 and C_2, respectively:

$$\Psi_0 - \Psi_\beta = \sigma_0 / C_1 \qquad (2)$$

$$\Psi_\beta - \Psi_d = -\sigma_d / C_2 \qquad (3)$$

where Ψ_0, Ψ_β, and Ψ_d represent the potentials for each plane and σ_0, σ_β, and σ_d represent the corresponding charges on each plane. The capacitance is defined by Gauss's Law:[213]

$$C_i = \varepsilon_i \varepsilon_0 / 4\pi\beta \quad (4)$$

where ε_i is the dielectric constant of interfacial water, ε_o is the permittivity of vacuum, and β is the distance between planes of electric potential in the structured interfacial region. The dielectric constant of interfacial water and the distance between planes cannot be measured through bulk experiments; therefore, the capacitances are usually treated as fit parameters. Direct measurement or calculation of the dielectric constant of interfacial water as a function of distance would provide valuable constraints on these models.

For the mineral-water interface, another potential, the zeta (ζ) potential, is defined. This potential corresponds to the electrical potential at the effective shear, or slipping plane, between the moving and stationary phases[215, 216]. The zeta potential is measured using electrophoresis. The behavior of ions from the zeta-plane into bulk water is well characterized by the Gouy-Chapman model. However, because this potential is based on macroscopic hydrodynamic measurements, there is no direct evidence that the ζ-plane is equivalent to the d-plane of the triple-layer model. In fact, there is some debate in the literature regarding the position of the ζ-plane, suggesting that it may occur midway into the diffuse layer at distances further away from the surface than the d-plane. Nonetheless, we expect that there should be some consistent physical relationship between the d- and ζ-planes that is dependent on interfacial water structure.

The EDL has also been investigated experimentally. Atomic Force Microscopy (AFM) has been used to investigate changes in surface charge as a function of pH.

Scanning Tunneling Microscopy (STM) has also been used to examine the dielectric properties of water[217]. However, it is difficult to establish a value for the static dielectric constant of water at the surface primarily due to problems in separating the dielectric contributions of the solid surface from those of the structured, interfacial water. In one study,[218] the dielectric constant of water was measured for the first and second monolayers of water on silica at 25°C and 1 bar. The first and second monolayers of water were reported to have dielectric constants of 5 and 30 respectively. A third analytical approach to investigating the properties of interfacial water is crystal truncation rod (CTR) diffraction. CTR data provides the location of water molecules with respect to specific mineral surface sites and height above the surface for potentially several layers of structured interfacial water. This approach has been used to study the calcite-water interface[219, 220], and the aqueous interface of several metal oxides[221-224].

In summary, the dielectric constant of water on charged surfaces is essentially unknown despite recent analytical advances in studying the solid-water interface. Numerous estimates have been made [225-228] and various approaches to calculating the dielectric constant of water have been presented[229-238]. The most common computational approach treats the dielectric constant as a function of the 3D polarization tensor with parallel and perpendicular components to the field[237]. This approach assumes that the dielectric is anisotropic in three dimensions, and utilizes the polarization density to compute the bulk value[233, 234, 237]. This approach has been applied to a water box simulation with hard boundaries meant to represent a platinum electrode[235] where a dielectric constant ranging from 5-30, depending on induced voltage, was calculated for the direction perpendicular to the hypothetical surface. Using a similar approach,

interfacial water at a dipalmitoylphosphatidylcholine (DPPC)[236] surface was calculated to have a dielectric constant of 5. These studies show fluctuations in the polarization density for electrode-water systems near the electrode surface, but do not address why interfacial water exhibits different properties than the bulk.

Although scientists have been conceptually aware that water is more structured, more viscous, and has a lower dielectric constant than bulk water at mineral surfaces, the surface-charge-screening capacity of interfacial water has never been considered a major player in creating the EDL. One work assumed a greater distribution of protons and hydroxyls near the surface for charge shielding[239]. Only recently, have Stern-Guoy-Chapman(SGC) models or surface complexation models(SCM), started to consider that the charge associated with the orientation of water dipoles at a solid surface may play a secondary role to shielding surface charge [227]

In this work, we calculate the dielectric constant of water as a function of distance from the goethite mineral surface at three different pH values. Our results suggest that the key features of the EDL can be attributed solely to the interactions between the mineral surface and the water molecules adsorbed to this surface. The SCG or SCM models used today incorporate th effect of structured water indirectly by fitting surface titration data to obtain values for the capacitance. The interlayer capacitance is assumed to be constant for a particular solid-water system, regardless of surface charge. Then the ions in solution play the primary role in screening the charge at the mineral surface. The picture that emerges from our study suggests that the structure of water at mineral surfaces plays a key role in screening surface charge. In addition, it reconciles the physical properties of the double layer with its electrochemical behavior.

Classical Molecular Dynamics (MD) Methods

Simulation Cell Construction

We chose to study goethite (α-FeOOH) because of its environmental ubiquity and we chose to focus on the (110) surface because it is the dominant crystal face of microcrystalline goethite[240] in the environment. In order to build a molecular dynamics simulation cell, we cleaved a model of the goethite unit cell[241] along the (110) growth plane using the Surface Builder module of Cerius[2] [242]. To create a neutral surface we singly-protonated all surface oxygens. We used a goethite surface slab approximately 36Å or 5 unit cells thick. We added a 36Å vacuum gap above the (110) surface which we filled with 586 water molecules, giving a bulk water density of approximately 1 g/L, which was subsequently refined through an NPT simulation. The overall initial simulation cell was approximately 24Å x 22Å x76Å (Fig. III-2).

The neutral goethite surface was modified to create positively- and negatively-charged goethite (110) surfaces by adjusting the surface proton count according to the MUSIC model[243], with one difference that is discussed below. In order to examine changes in interfacial water structure over a range of pH values, we chose to bracket the neutral goethite surface (pH 9) with charged goethite surfaces corresponding to pH 6 and 12. Figure III-3 illustrates the three surfaces. The five oxygens on the surface are unique. Looking at the neutral surface shown in Fig. III-3A, from left to right, the first two surface oxygen atoms are both triply-coordinated by iron atoms (Fe_3O_{II}-H and Fe_3O_I) and correspond to a hydrogen bond donor and acceptor pair. The I and the II refer to the fact that in the bulk crystal there are two different, triply-bonded oxygens at this surface:

I is an H-bond receiver, while II is a proton donor, both in the bulk and at the neutral surface. These are followed by a hydroxylated, bridging oxygen atom (Fe_2O-H), a triply-coordinated hydroxyl group (Fe_3O_{II}-H), and a monodentate surface hydroxyl group (Fe_1O-H). The oxygen atom in the second (Fe_3O_{II}-H) surface site is H-bonded to the (Fe_1O-H) site. We added one proton per unit cell at the Fe_1O-H site to form $Fe_1OH_2^+$ on the positive slab (right most oxygen in Fig. III-3B) and removed one proton from one Fe_3O_{II}-H site to form $Fe_3O_{II}^-$ on the negative slab (left most oxygen in Fig. III-3C).

The one difference between our representation of the goethite surface and that of Hiemstra et al.[244] is in our treatment of one of the two Fe_3O_{II}-H sites for the negative slab (Fig. III-3C). Hiemstra et al.[244] postulated that the second deprotonated $Fe_3O_{II}^-$ group in a negative surface unit cell would H-bond with water. However, our initial energy minimizations resulted in severe surface distortions if this proton was removed, because $Fe_3O_{II}^-$ remained H-bonded to the neighboring Fe_1O-H site (Fig. III-3C second oxygen from the right). In order to preserve the surface structure and design negative and positive surfaces that have the same charge magnitude, we removed only one proton from the neutral unit cell to create a negatively-charged unit cell.

Molecular Dynamics Simulations

After an initial Cerius[2] minimization of 500 steps, classical molecular dynamics (MD) simulations were performed using the program LAMMPS[245, 246] and the CLAYFF forcefield. For complete details on the CLAYFF force-field see Cygan et al.[247]. See Table III-1 for all force-field parameters used in this study. CLAYFF uses a flexible SPC water model[248-250] We used CLAYFF partial charges for the Fe, O, and H in the bulk

goethite structure. For surface oxygens and hydrogens, we used charges from hybrid Density Functional Theory (DFT) Natural Bond Order (NBO) calculations on large goethite clusters. These charges are provided in Table III-2. The differences in CLAYFF partial charges for atoms in bulk goethite and water reported in Table III-1, and those calculated for the surface groups (Table III-2), are on the order of ~0.1.

These small perturbations in surface group charges and the need to create surfaces with a positive and negative net charge, initially made all of our simulation cells charged. The overall charge of the simulation cell must be neutral in order to use the Ewald summation method[162] to calculate Van der Waals forces during a molecular dynamics simulation. The charge module of Cerius[2] was used to average the total charge of the surface slabs to zero. This procedure modified the partial charges of all atoms in the goethite surface slabs by < 0.1 in all cases, and often by < 0.05.

LAMMPS calculations were performed on the three surface slabs and a reference water box with the same dimensions as the water layer in the goethite-water simulation cells. The time step for all MD simulations was one femtosecond. First, a 50 picosecond (ps) equilibration NVE (NVE: constant number, volume, and energy) MD simulation was performed, then a 500 ps NPT (NPT: constant number, pressure, and temperature) simulation at one bar (P = 0 GPa) and 300 K. In the latter simulation, only the z-direction of the simulation cell was allowed to vary. This allowed the water in the simulation cell to reach a density appropriate to the surface conditions. The final z dimensions for the neutral, positive, and negative goethite-water simulation cells were 76.5443 Å, 76.97 Å, and 77.589 Å, respectively. Dipole orientation and other position data were sampled for each goethite-water system in a subsequent simulation that ran for

1 nanosecond using an NVT ensemble (T=300 K). XYZ coordinates for all atoms were tabulated at every time step.

Analysis Approach

We used two Fortran codes to analyze the trajectory files from the MD simulations. The first code, written by Kalinichev [251], was used to determine the vertical atomic density profile, cross-sectional surface maps for the atoms, and average dipole directions for the water molecules.

We used the truncated Kirkwood method, introduced by Richardi[252], to calculate the dielectric constant of water. The Kirkwood method calculates the dielectric constant by taking the dot product of each water molecule dipole with all of its nearest neighbors[232]. The truncated approach reduces the number of steps required for equilibration, by avoiding the need for long-range convergence, which only takes place after several nanoseconds. The radial Kirkwood factor, $G_k(r)$ is a measure of the local effective dielectric at radius r and is given by:

$$G_k(R_{ij}) = \frac{1}{N\mu^2}\left\langle \sum_{i=1}^{N}\sum_{j=1}^{N} \vec{\mu}_i \bullet \vec{\mu}_i \right\rangle, R_{ij} < R_{Trunk} \qquad (4)$$

where N is the number of water molecules in the box or layer of interest, μ^2 is the norm of the dipole of water squared in this case: $(0.41*e/3.33564x10^{-20})^2$ debye^2, i is the index corresponding to the molecules in the box or layer of interest, j is the index corresponding to the nearest neighbors of water molecule I, and $\left\langle \sum_{i=1}^{N}\sum_{j=1}^{N} \vec{\mu}_i \bullet \vec{\mu}_i \right\rangle$ is the time averaged sum of the dot products of all pairs of water molecule dipoles. R_{trunk} is the truncation distance and corresponds to the first maximum of the Kirkwood function. Figure III-4 shows our

approach to calculating the radial Kirkwood function for our goethite surface water boxes. The maximum of the Kirkwood function at R_{trunk} = 6 Å is consistent across all of our simulations. The Kirkwood factor G_k is related to the static dielectric constant (ε_s) as follows:

$$y_D G_k = (\varepsilon_s + 1)(2\ \varepsilon_s - 1)/9\varepsilon_s \quad (5)$$

Since the static dielectric constant (ε_s) of water is much greater than one, we can simplify Eqn. 5 as follows:

$$y_D G_k = (2\varepsilon_s + 1)/9 \quad (6)$$

The constant, y_D is equal to $4\pi\rho\mu^2/(9k_bT)$ in cgs (centimeter-gram-second) units[232], and has a value of 4.347 for water at 298.15 K. Dipole-dipole correlations inherent in this calculation are slow to reach a dynamic equilibrium and require simulation times on the order of tens of nanoseconds to produce a statistically significant value. Therefore, it is necessary to calculate the dielectric from short-range interactions, which converge faster. This method, while approximate, should provide estimates within 10% of the real value[252].

In order to apply this method to measure the relative dielectric constant of water above a surface slab as compared to that of bulk water, the water in the box was divided into thin layers that were treated as individual units. The double sum whole box was reduced to a series of double sums, one for each layer to determine how the dielectric

changed with distance from the surface. We reduced the second sum to include in the product only those waters that were within a given radius illustrated by the large circle. These waters could be, and frequently were, in different layers. Waters in the mirror, *i.e.* those outside the thick dashed lines in Figure III-4, were not included in the dipole dot product, even if they were within the circle.

There is no information *a priori* as to what would make a good box size for calculating a dielectric constant. Given that Richardi[252] collected water dipole data for 100,000 timesteps for simulation cells containing 256-512 water molecules to determine the dielectric constant of bulk water, we assumed that we could determine the dielectric constant as a function of distance away from the goethite-water interface if we collected data for 1,000,000 timesteps, and divided the water in the simulation cell into 10-20 thin slices parallel to the goethite surface (each thin layer contains approx. 586/12 or ~50 H_2O molecules). We started with 3 Å thick layers, and later determined that using thinner layers did not increase the uncertainty proportionally; if we take 1/10 the slice thickness, the uncertainty only increases by a factor of 2.5.

During the MD simulations, images of the primary simulation cell are maintained in all directions so that forces are felt in all directions and an approximation of infinite size is maintained. The method for incorporating these images into the dielectric was to compute the closest distance of approach between two water molecules. This prevented double counting and ensured that the analysis was reliable up to a truncation distance of half the smallest box length, which is double the 6Å cutoff actually used.

Results

During the course of the simulations, we noticed some minor distortion of the goethite lattice structure at the interface in both the negative and positive slabs, but not in the neutral slab. On the negative slab this distortion affected only the position and bond lengths for one Fe atom on each surface and the associated surface OH groups. On the positive slab the loss of an adsorbed water molecule caused the Fe atom to settle into the bulk crystal. In each instance these distortions moved one Fe completely out of position. However, they appeared to have only a trivial effect on the structure of interfacial water, as they affected only one site in 16 unit cells. Therefore, we felt that these minor surface discrepancies would not have a significant effect on our overall results.

Water Box

In order to validate our method, we used the truncated Kirkwood approach[252], both on the whole (35.76 Å x 21Å x 23.1Å) water box and for 3Å slices in the same box. The calculated dielectric constant for the whole box is 84.7±2. This is the same as when the box is sliced into layers. The error for each individual slice increases to 5. This value is taken to be our reference bulk water value for our goethite-water slab calculations. There is no overall trend among the slices. The flexible SPC water model is reported to give a dielectric constant of ≈84[253].

The Neutral Slab

For the neutral slab, first we looked at the atomic density profiles for water oxygen and hydrogen as a function of distance away from the goethite surface. These profiles are illustrated in Fig. III-5A. The number density is calculated as the average

number of atoms over the simulation time in ~0.2Å slices parallel to the goethite surface. Three distinct peaks for oxygen and four for hydrogen, including the shoulder in the first hydrogen peak, indicate the presence of more O or H atoms at specific distances from the goethite surface than occur in unstructured bulk water. The charge density in water, as a function of distance from the goethite surface, was calculated as the difference between the number density of hydrogen atoms and double that of oxygen atoms, which takes into account the opposing charges. The water oxygen and water hydrogen atomic density profiles and the charge density profile were highly stable throughout the entire simulation. Calculated standard deviations over groups of 10000 steps for points along these profiles were only slightly larger than the line thickness in Fig. III-5.

Figure III-5 also shows the average magnitude of the water dipole vector projected in the z direction. Like the atomic density profiles, the dipole vector was averaged over increments of ~0.2 Å. The calculated profile for the water dipole vector z projection (z-dipole) possessed a standard deviation that approached half the magnitude of the property itself due to large variations in magnitude from step to step. The maximum was always around the same distance from the surface, indicating that this is a physical result even if the magnitude was not significant. Although the z-dipole curve could not be used as a primary indicator of the water's electric field, the difference between the vertical profiles of hydrogen density minus twice the oxygen density form the basis of that field which would be felt by an adsorbing anion. Due to the fact that an adsorbing ion only feels forces on the same scale as its size ~1-3Å, these fluctuations would be more like a magnetic disturbance rather than electric repulsions. This charge density variation will affect both surface charge screening and ion adsorption.

Figure III-6 illustrates the calculated, truncated dielectric constant for water as a function of distance from goethite for neutral, positively, and negatively-charged surfaces. The dielectric constant at each point in the profile is averaged over an approximately 1.5Å thickness. This layer thickness was found to perform better than a 3Å thickness, because each structured layer has a slightly different dielectric constant. We subdivided the dielectric constant profile into layers of approximately 1.5Å that were aligned with the peaks in atomic density in order to calculate specifically the dielectric constant of each structured water layer. This approach reduced substantially the corresponding standard deviations for the averaged dielectric constants. In the structured region of the interface, (Fig. III-6A) the dielectric constant is 65-85. Averaging a bicameral distribution from two different structured layers produced meaningless results in all cases *i.e.* 30$\pm$ 30. While the distinction between the diffuse layer and bulk water is less obvious, the diffuse layer has a dielectric that is $\approx$ 4 lower than that of the bulk, indicating an effect from the surface potential. This difference is consistent for the positive and negative goethite surface slabs as well.

Figure III-7 illustrates surface maps for the first 6Å above the neutral goethite surface. These maps represent six unit cells in the x-direction and two unit cells in the y-direction. We see three structured layers of oxygen and three of hydrogen, just as in the atomic density profiles. The first water oxygen layer (Fig. III-6A) consists of definitive rows of oxygen atoms on the goethite surface. In the trough**,** corresponding to the first two oxygens Fe_3O_{II} and Fe_3O_I in Figure III-3, the water oxygen atoms in this layer are H-bonded to two surface oxygens, one donating a proton, the other receiving a proton to form hydrogen bonds. The first layer of water hydrogen (Fig. III-7E) corresponds to the

solvating water donating a hydrogen bond. In both cases, for the first layer of H and O, there appears to be two, slightly separated, alternate adsorption sites, in the case of oxygen they are almost overlapping. The second layer of water oxygens (Fig. III-7B) is hydrogen bonded to the surface hydroxyl groups and forms two diffuse parallel rows per unit cell. The second layer of hydrogen atoms appears to point down toward the first layer of water, forming H-bonds between water layers 1 and 2. Water-oxygen layer 3 is directly above layer 1. In this case, the structure appears to be a broad, double row of oxygen atoms. Figure III-3, shows a schematic representation of what the simplified surface looks like.

The Positive Slab

Turning first to the water atom density profiles in Fig. III-5, we see that the water oxygen and hydrogen peaks are more tightly spaced (1.2 Å) at the positive goethite surface (Fig. III-5B) than at the neutral goethite surface (Fig. III-5A). The second layer is actually a doublet, and behaves electronically as two separate layers, apparent from the large standard deviation in the dielectric value for this layer. At the positive goethite surface, there are five structured layers of water, including the $-OH_2$ group of the doubly-protonated surface sites. This $-OH_2$ group was treated as flexible SPC water in the simulations; therefore it is included in our analyses. The first peak is hydrogen, which is the exception because thereafter the oxygens align themselves closer to the surface. Five distinct oxygen peaks and four hydrogen peaks are apparent in the graph, indicating an increase in surface structure. The charge density oscillations are faster at first but slow down as the diffuse layer is reached. Correspondingly, the z dipole projection is

consistently positive, reflecting the charge on the surface and the directionality of the water as expressed in the charge density. The magnitude is two orders higher than that of the neutral case. Whether the split peaks are significant is unclear.

The calculated dielectric constant profile illustrated in Fig. III-6B shows four distinct regions. Moving outward from the surface, Fig. III-6B illustrates the surface dielectric due to the $–OH_2$ functional groups, then the dielectric constants of the, interfacial structured and diffuse layers and, finally the dielectric constant of bulk water. The calculated dielectric constant for the surface layer of $–OH_2$ groups is small ($\varepsilon \approx 25$). Overall, the dielectric for the structured or Stern layer is lower ($\varepsilon \approx 54$) than that of bulk water. This change is on par with changes associated with increases in ionic strength rather than prior predictions of charging surfaces[254]. Given the increase in orientation along the z direction to mitigate charge in the structured layer, the lowering of a coupled property, the dielectric constant, is unexpected in this context; the reason must be anti-correlation of the x-y vectors. As vectors line up to mitigate one charge, their ability to dynamically shield a second charge is reduced. The diffuse layer here is similar to the diffuse layer in the neutral case. It may be slightly thinner, but here too differentiating between diffuse and bulk layers is difficult. Additionally, there is a delayed transition, of a few angstroms thickness, between the structured and diffuse layers where the dielectric remains low despite the loss of structure of the water. The fact that there is no significant expansion of the structured and diffuse layers indicates that the polar nature of water is capable of shielding the surface charge.

The surface maps provided in Fig. III-8 give a more detailed picture of the water structure resulting from the charging of the interface as well as hydrogen bonding to

surface groups. The first layer of oxygen atoms represented in Fig. III-8A are the oxygen atoms of the $–OH_2$ surface functional groups. The hydrogen layer closest to the goethite surface (Fig. III-8G) are not the hydrogen atoms in these surface functional groups, but but rather the hydrogen atoms of the first structured layer of water indicating that this water is pointing in a nearly identical configuration to the first structured layer in the neutral slab (see Fig. III-3B). There is a second, more poorly-filled oxygen site in this layer, but how it is binding is unclear. The second hydrogen layer (Fig III-8H) corresponds to the hydrogen atoms of the $–OH_2$ groups, that point upward into the solution. Subsequent structured layers of water display a tree-like bifurcation with subsequent layers oriented with both hydrogen atoms pointed away from the goethite surface. Since this initial orientation of the hydrogen bonds, combined with charge reinforces the surface structure, an additional structured layer is favored over diffuse water.

The Negative Slab

The atomic density profiles for the negative slab (Fig. III-5C) look similar to those of the neutral slab. The difference in the atom density is a doublet in the hydrogen density profile, and the first two peaks of negative charge in the neutral case have been merged into one big peak. In the dielectric z direction function there is a stronger negative peak before the directionality of the dipole turns positive. The overall direction is surprising, as it would only serve to reinforce the charge potential rather than shield it.

The dielectric constant profile exhibits layering similar to that for the neutral slab with much wider swings in variations. The structured layer is thinner than in the positive

slab, about 4.8Å. The overall dielectric constant of water in the structured region is higher than both the neutral and positive cases, a result that is surprising. The transitional behavior appears again, with a dielectric constant calculated to be as great as bulk water consistent with the structured layer dielectric. The diffuse layer is thicker than in the other profiles, stretching out to approximately 16Å above the surface.

The surface maps show a nearly identical arrangement of both oxygen and hydrogen atoms as for the neutral slab, with one key difference. In the first layer of water molecules, both water hydrogen atoms point toward the surface. Since the trough, corresponding to the first two oxygens Fe_3O_{II} and Fe_3O_I in Figure III-3C, is only large enough to allow for one water molecule, the other molecules will not be able to take advantage of the deprotonation on the surface to reorient and shield the charge. The next layer of water is hydrogen-bound to the surface hydroxyl groups. As a result, it must, to some degree, point its hydrogens towards the bulk liquid. Since more hydrogens than oxygens are pointing out to the bulk, the third layer is forced to reinforce the positive z dipole.

Transitional Behavior or a Shear Layer

There appears to be an electrical lag between the structured water layer and the diffuse water layer in all three slabs. In this region the dielectric constant profile is similar to that in the structured layer, however the water structure is disordered. This region may correspond to the shear layer, which is the first layer of water that is able to be pulled away from the goethite surface into a flowing system[216]. For proof that this is what we are observing, a direct confirmation of the relationship between the Stern plane and the

plane of zeta potential, formally the shear layer, would be required. However, what we can say is that the electronic transition between the structured and diffuse layers may not be sharp but rather may take place over a few angstroms.

Discussion

The charge-density profiles and z dipole profiles shown in Figs. III-5A-C, and the dielectric constant profiles shown in Figs. III-6A-C allow us to create a complete picture of the electrochemical structure of the goethite-water interface. Physically, our calculated interfacial water structure matches that seen experimentally on hematite (1 -1 2) surface perfectly which is similar to the (110) surface on goethite [223]. This experimental method cannot be used for some minerals, like goethite, because large single crystals of these minerals cannot be obtained. Both our calculations and the CTR results show a staggered first monolayer of water whose structure is determined by the topography of hydrogen bonding between the water molecules and the surface. We treated this monolayer as two slices in our dielectric constant calculations because it corresponded to two peaks in the vertical atom density profile. The calculations show more structure than the experimental results; however, the layer beyond the first staggered monolayer is poorly resolved in the surface maps of the neutral goethite surface. Therefore, it is no surprise that it was not resolved experimentally.

The first point that can be addressed with regards to the SGC models is that the dielectric constant of the structured or Stern layer and the capacitance of this layer can be calculated from our simulation results. We present these values in Table III-3. We

assumed that Ψ_d is determined based on the vertical water structure rather than the dielectric value. Division of the structured layer can also be made based on electrochemical rather than physical grounds, in which case, the slices which show transitional shear behavior would be included as part of the structured layer based on their dielectric values. This was not done for two reasons: 1) the divisions between layers based on the dielectric alone are subjective at best and, 2) we want to be able to compare our model results to the SGC model as well as possible. Overall, we can align the SGC picture with ours reasonably well. The capacitances in Table III-3 correspond well to the predictions of Sverjensky,[228] but for different reasons.

Without any ions in solution, we observe an electric double layer at the goethite surface. This result does not imply that ions in solution will not contribute to the EDL surface structure. They would, if present, likely reduce the dielectric screening capacity of the interface further than the effect of just the charged surface[254]. The SGC conceptualization of physically adsorbed ions in the structured water layers of the interface, and a weighted distribution in the diffuse layer is perfectly consistent with our structure. Likewise, if we separate each calculated structured monolayer of water, we effectively match the structure of triple and higher layer models. This work provides a comprehensive picture that matches experimental observations. The one big limitation is the inability to include the net vertical dipole of the water in this picture.

The effect of the net dipole

Due to the net vertical dipole, the calculated electronic behavior of the positive and negative surface slabs is entirely different. The effects of changes in water

orientation as a function of surface charge are completely neglected in the SGC model. In the positive case, the water dipole orientation attenuates charge in conjunction with the dielectric constant, while the negative case the dielectric constant is doing the attenuation as the dipoles would only reinforce the potential resulting from the surface charge. If we used any sort of SGC formulation we would predict that the thickness of the double layer would be exactly the same in the positive case than the negative one, which is the clearly different from what we observe.

In the SGC models, the potential energy or work function is defined as a measure of the required work to bring an ion to the surface. In the neutral slab, this potential is entirely a result of charge separation in the structured water layers. The magnitude of the electric potential energy barrier required to bring both positive and negative ions is small and symmetric, but the maximum in the electric potential gradient from the surface into solution occurs at different distances for negative and positive ions.

The electric behavior of the positive slab looks similar to schematics of the SGC models. The structured layer can be divided into additional layers corresponding to each individual layer of water, but the basic double layer structure is clear. The influence of the net dipole is not shown, as it would only create a small overlying wiggle in the potential, but as the dipoles attenuate charge, the potential slope declines to zero.

For the negative slab, the combination of surface charge and water molecule adsorption is counter productive. Hydrogen-bonding of water molecules to the surface orients the molecules in the direction opposite to the charge shielding direction. This is why there is no shoulder to the first water hydrogen atomic density peak as seen in the positive case. The corresponding increase in dielectric constant between the structured

and diffuse layers is also a result of this unfavorable juxtaposition, as is the extension of the diffuse layer an additional 6Å to shield the surface charge. Thus the behavior of a 16Å-thick layer of water is determined solely by the surface charge and the hydrogen-bonding pattern of the first monolayer of water to the surface. The positive and negative surface slabs illustrate extremes of when these two factors (i.e. surface charge and dipole orientation) align together and when they oppose each other.

Mathematical Representation

We can write the potential of our electric-double layer as a sum of two components. The first is the charge on the surface as screened by the dielectric constant. The second is the net water dipole orientation resulting from charge separations of the water oxygen and hydrogen atoms in the structured water layer. In both cases, because the charge distributions are approximately uniform in the xy plane, we considered the problem as one of stacked disks of charge for purposes of mathematical integration. For the surface component:

$$\Psi_s = \frac{\sigma_s}{2\varepsilon_0\varepsilon_s}(\sqrt{z^2+\kappa^2} - z) \tag{8}$$

This assumes that $z \geq 0$, $\kappa = (\varepsilon_o\varepsilon_s T/2e_0^2 N_A I)^{1/2}$ the Debye length, σ is the charge per area of the unit cell, z is the distance above the surface, ε_0 is the permittivity of the vacuum, ε_s is the dielectric constant of the water above the surface in the interfacial region, N_A is Avagadro's number, and I is the ionic strength. To use this function it is necessary to assume that the dielectric constant is the same for all z, or at least a smoothly varying function of z; otherwise the function will be discontinuous. For the charge separations in the water we used a similar form:

$$\Psi_w = \frac{\sigma_w}{2\varepsilon_0\varepsilon_s}\left(\sqrt{\left(z-z^+\right)^2+R^2}-\sqrt{\left(z-z^+\right)^2}-\left(\sqrt{\left(z-z^-\right)^2+R^2}-\sqrt{\left(z-z^-\right)^2}\right)\right) \quad (9)$$

where σ_w is the charge density of the water and is equal to $0.81/(\pi R_w^2)$, where 0.81 is the charge of the oxygen used in this simulation, or twice the hydrogen atom charge, and R_w is the radius of one water molecule. In this case, we consider only one layer of hydrogens and one layer of oxygens. This approximation is consistent with multiple clusters of positive and negative charge, if one considers z^+ to be the z position of the average of positive charge density, and z^- to be the z position of the average of negative charge density. Optionally, one could consider extra terms for every layer of oxygens and hydrogens, making sure to use the correct sign for σ in each case. In this case, we can include other charges (i.e., from aqueous ions) as well:

$$\Psi_c = \sum_{charges} \frac{\pm\sigma_c}{2\varepsilon_0\varepsilon_s}\left(\sqrt{\left(z-z^\pm\right)^2+R^2}-\sqrt{\left(z-z^\pm\right)^2}\right) \quad (10)$$

In either case, the long distance behavior matches the sort of exponential decay, i.e. it asymptotically approaches 0, which is predicted by the Gouy-Chapman model (eq. 2). The unusual form of Eqn. (10) was selected to match the potential behavior of the near surface structured water given that the charges are not point charges and that the potential must be continuous. While this model has significant underlying assumptions, it fits the observed behavior well, and can be expanded with greater mathematical accuracy if so desired. For example, it is possible to divide the system into two layers with different dielectric constants, such as a diffuse layer with approximately a bulk dielectric (ε_2), and a structured layer with a lower dielectric (ε_1) with a plane dividing them at z = d. Two assumptions must be maintained: first, that $\Psi(\infty) = 0$ and, second, that $\Psi(z)$ is everywhere continuous. For z > d this just reverts to our constant solution:

$$\Psi_{z>d} = \frac{\sigma_s}{2\varepsilon_0\varepsilon_2}(\sqrt{z^2 + R^2} - z) \tag{11}$$

The surface charge is still used, as it is not dependent on the dielectric constant. For z < d, we need to make sure that the function depends not on ε_2 but on ε_1 and that this expression is equal to eq. 11 at z = d. This is achieved as follows:

$$\Psi_{z<d\text{-two }\varepsilon}(z) = \Psi_{z<d\text{-constant }\varepsilon}(z) - \Psi_{z<d\text{-constant }\varepsilon}(d) + \Psi_{z>d}(d) \tag{12}$$

Therefore:

$$\Psi_{z<d} = \frac{\sigma_s}{2\varepsilon_0\varepsilon_1}(\sqrt{z^2 + R^2} - z) - \frac{\sigma_s}{2\varepsilon_0\varepsilon_1}(\sqrt{d^2 + R^2} - d) + \frac{\sigma_s}{2\varepsilon_0\varepsilon_2}(\sqrt{d^2 + R^2} - d) \tag{13}$$

It is trivial to see that if z = d the first two terms cancel and eq. 13 equals eq 11. This approach can be applied analogously to a system with charged ions or with water molecules with a net dipole at z.

Conclusions

This simulation indicates that the dielectric constant of water in the interfacial region is sufficient to ameliorate surface charge without additional assistance from ions. For the structured region it varies from 45 to 4 above bulk depending on surface charge and hydrogen bonding to the surface; the two factors that give rise to the double layer in the first place. The diffuse region dielectric is consistently 4 points below bulk water. The double layer structure of water is a result of the surface charge and hydrogen bonding to the surface. The net water dipole is a result of hydrogen bonding to the surface and can either be aligned or opposed to the potential. The high fluctuations in the average z projection of the water dipole vector indicate that longer time may be required for subtler equilibration, which would improve on current uncertainties.

Ions could still affect the shielding capability in a secondary capacity, but would trade off with reduced dielectric capacity. The physical behavior of ions is not contradicted in this work, only their importance in charge screening. This work represents a fundamental re-envisioning of the assumptions underlying the layered interface models, including the double and triple layer models. Finally, it restores the original mathematical models to a clear physical basis.

Acknowledgements: MCFW are grateful for financial support from NSF-Chemistry through the Center for Environmental Molecular Science at Stony Brook, Award #CHE-0221934 and a supplement that allowed MCFW to take up residence at EMSL to conduct part of this work. MCFW also wishes to thank Martin Schoonen for the opportunity afforded during his PhD to complete this project. LJC wishes to acknowledge support from the U.S. Department of Energy, Office of Basic Energy Sciences, Division of Chemical Sciences, Geosciences, and Biosciences. Sandia National Laboratories is a multi-program laboratory operated by the Sandia Corporation, a Lockheed Martin Company for the United States Department of Energy's National Nuclear Security Administration under Contract DE-AC04-94AL85000.

Table III-1. CLAYFF Parameters		
Element	**Mass**	**Charge**
Goethite H	1.00797	0.4268
Goethite Fe	55.8470	1.5768
Goethite O (H-Donor)	15.9994	-0.9482
Goethite O (H-Acceptor)	15.9994	-1.0482
Water O	15.9994	0.82
Water H	1.00797	0.41
Lennard Jones 12-6	**Pair Coefficients**	
Parameters	σ_{12}	σ_6
Goethite H	0.0000	0.0000
Goethite Fe	0.90298×10^{-6}	4.9062
Goethite O (H-Donor)	0.1554	3.1655
Goethite O (H-Acceptor)	0.1554	3.1655
Water O	0.1554	3.1655
Water H	0.0000	0.0000
	Bond Coefficients	
Goethite O-H	554.1349	1.0000
Water O-H	554.1349	1.0000
	Angle Coefficients	
H-O-H	45.7696	109.4700

Table III-2. Atom partial charges for surface groups		
Group	**Oxygen**	**Hydrogen**
$=OH_2^+$	-0.95	0.5
=OH	-1.05	0.45
$=O^-$	-1.15	N/A

Table III-3: Calculated Capacitances for the structured layers from our calculations			
Slab	**Distance/Å**	**Average Dielectric**[a]	**Capacitance/(**$\mu F/cm^{-2}$)
Neutral	4.8	**76.2 (1.9)**	**140.6 (3.5)**
Positive	5.3	**54.2 (3.5)**	**90.5 (5.7)**
Negative	4.9	**68.3 (3.1)**	**123.4 (5.7)**
[a]The values in parenthesis are uncertainties. Remember dielectrics are relative to a bulk value of 84.			

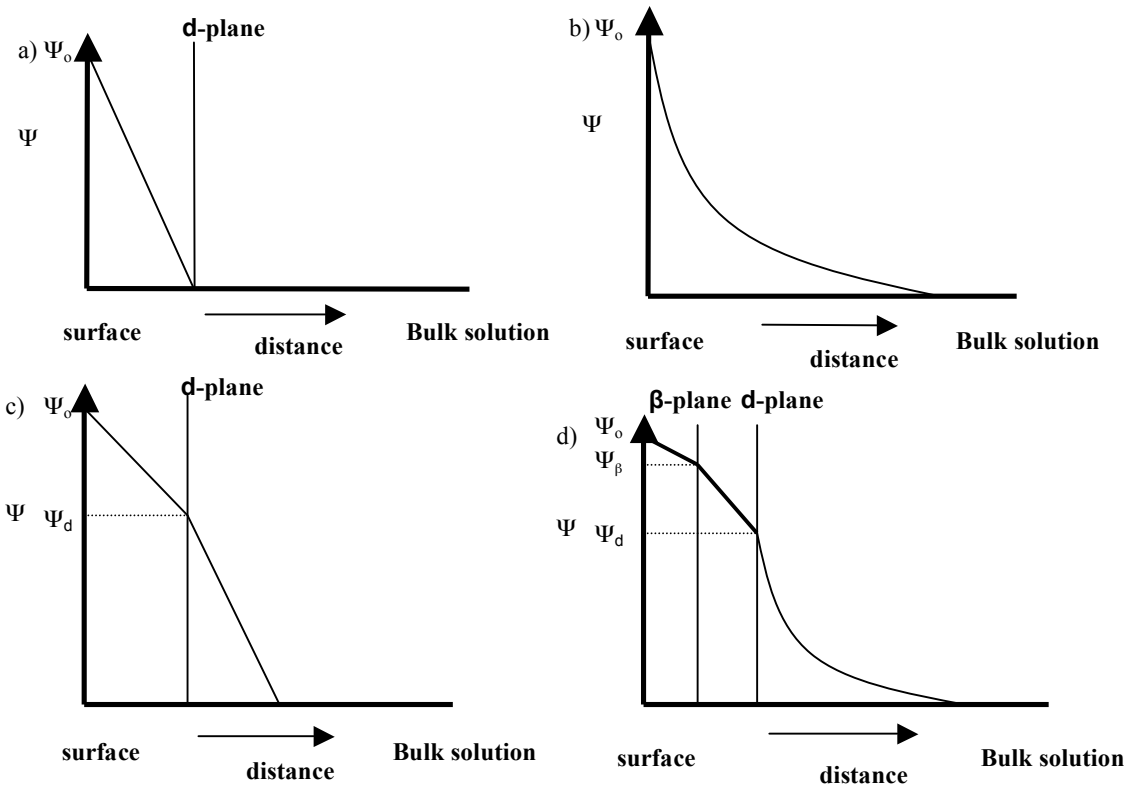

Figure III-1: Historical models of the interfacial region above a charged surface: a) Helmholtz single layer model[208, 209] b) Gouy-Chapman diffuse layer model[210, 211] c) Stern double layer model[212] d) triple layer model[255] showing Stern and Helmholtz layers.

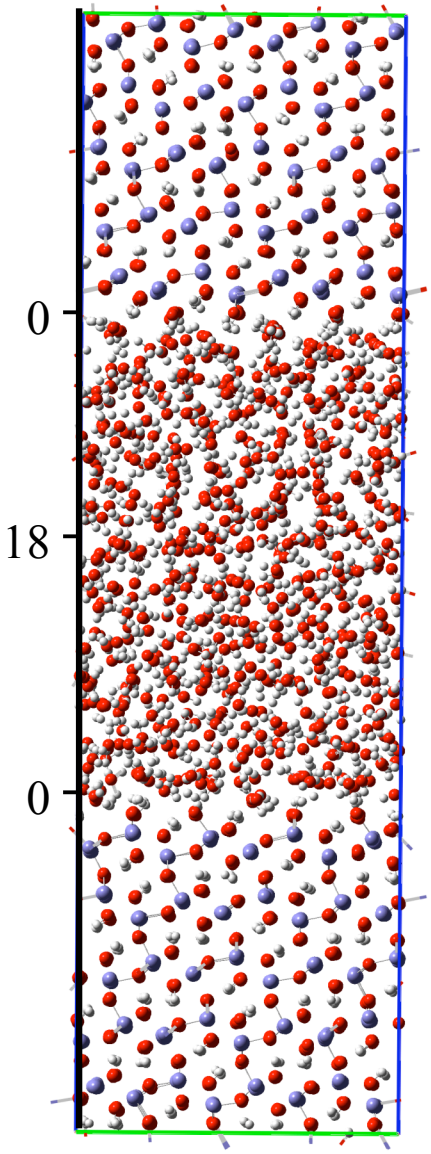

Figure III-2: Slab used in this simulation. Protons were added or removed from this slab to make the positive and negative surfaces. Blue = Fe, Red = O, and White = H.

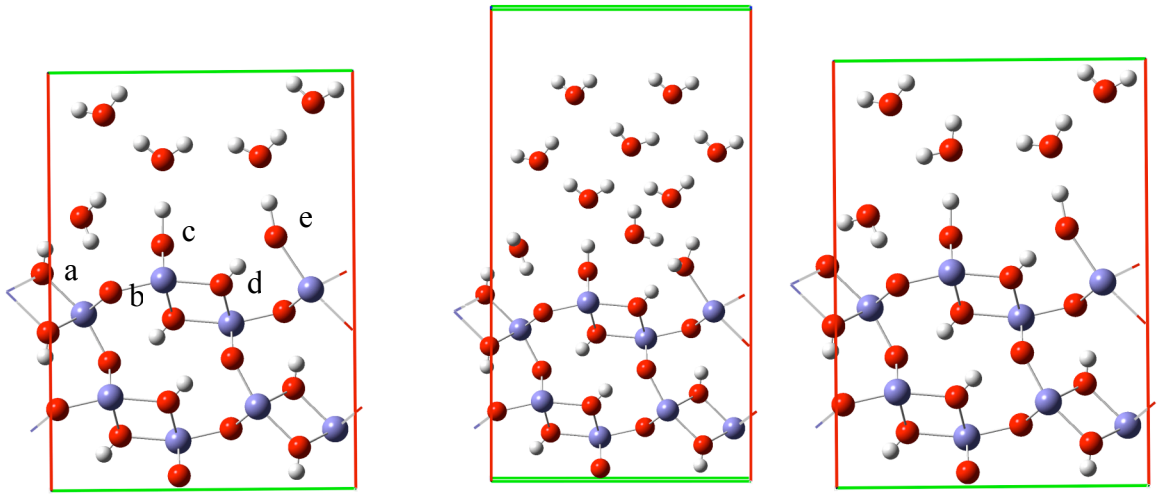

a) **b)** **c)**

Figure III-3: Diagrams of the surface unit cells for the a) neutral, b) positive, and c) negative (110) goethite surface. The vertical depth of the cell corresponds to approximately 1 unit cell. Each diagram includes a schematic of possible structured solvent layers determined from surface density maps. In (a) the surface oxygen atoms correspond to the descriptions in the text as follows: a = Fe_3O_{II}-H, b = Fe_3O_I, c = Fe_2O-H, d = Fe_3O_{II}-H, and e = Fe_1O-H. In (b), a = Fe_3O_{II}-H, b = Fe_3O_I, c = Fe_2O-H, d = Fe_3O_{II}-H, and e = Fe_1O-H_2^+. In (c), a = $Fe_3O_{II}^-$, b = Fe_3O_I, c = Fe_2O-H, d = Fe_3O_{II}-H, and e = Fe_1O-H. (Blue = Fe, Red = O, White = H).

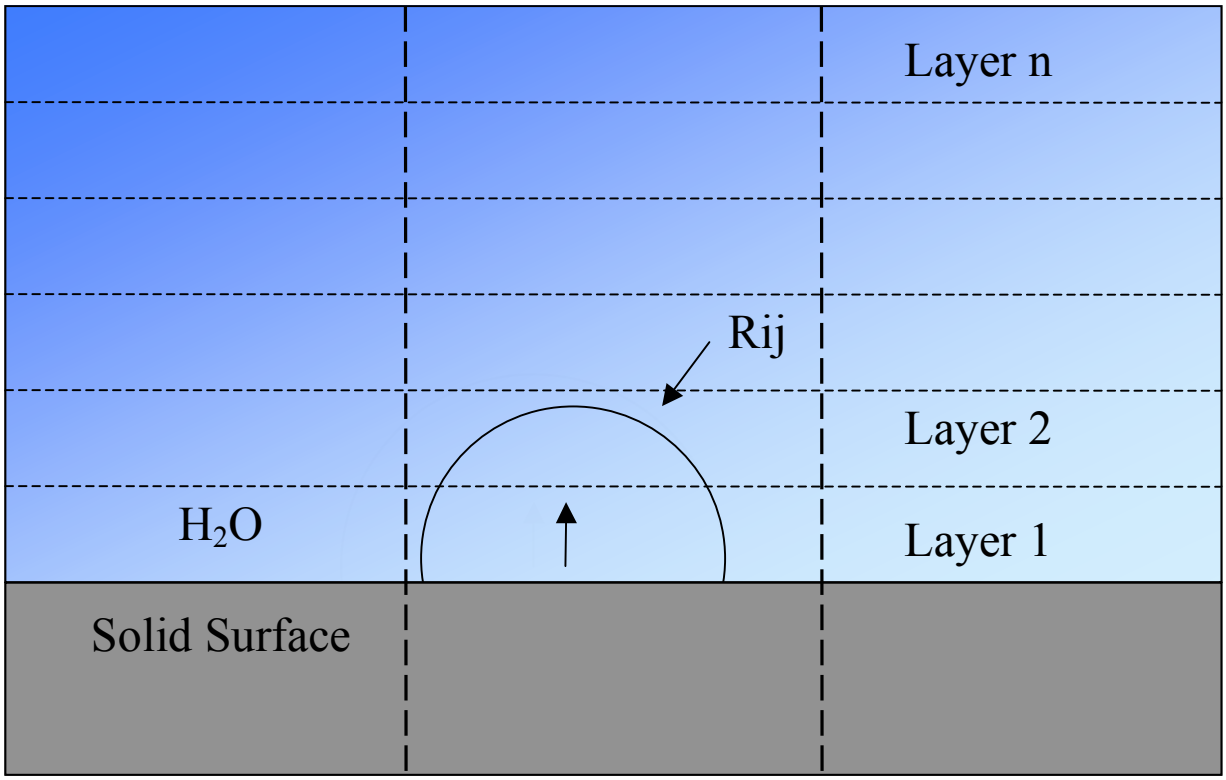

Figure III-4: Diagram that illustrates the truncation approach used in this paper. The solid circle indicates the radius of truncation. The thick dashed lines are the periodic boundaries of the simulation cell, and the thin dotted lines separate the layers.

A)

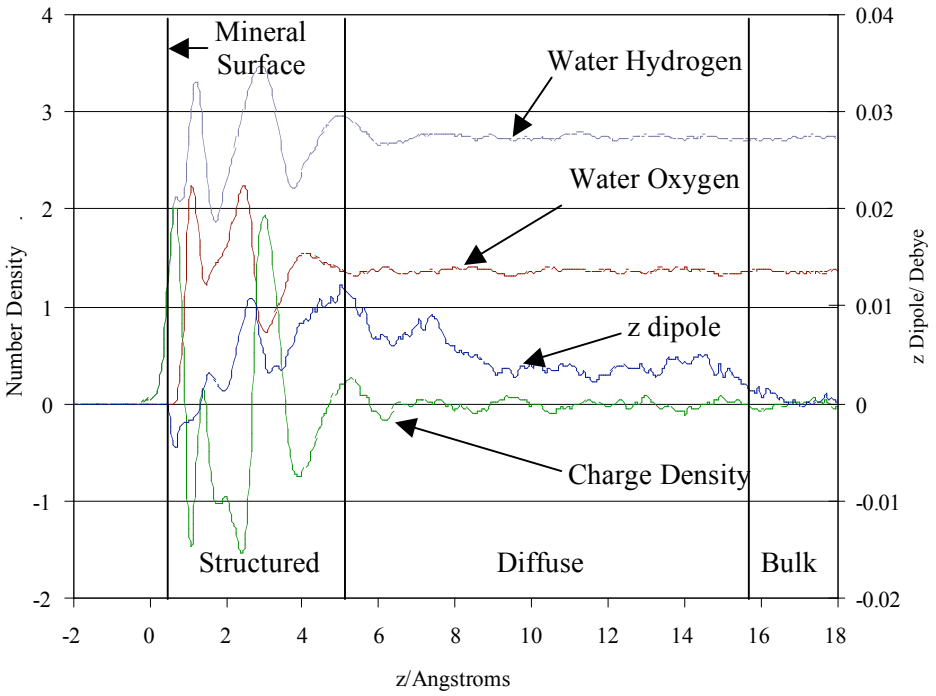
Mineral Surface
Water Hydrogen
Water Oxygen
z dipole
Charge Density
Structured
Diffuse
Bulk
Number Density
z Dipole/ Debye
z/Angstroms

B)

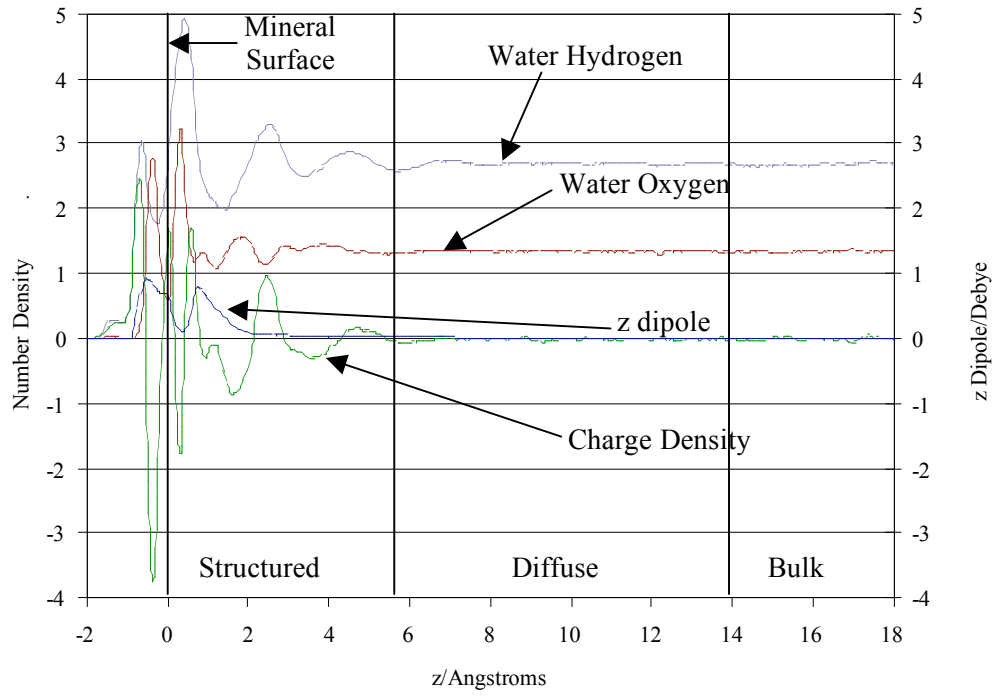
Mineral Surface
Water Hydrogen
Water Oxygen
z dipole
Charge Density
Structured
Diffuse
Bulk
Number Density
z Dipole/Debye
z/Angstroms

C)

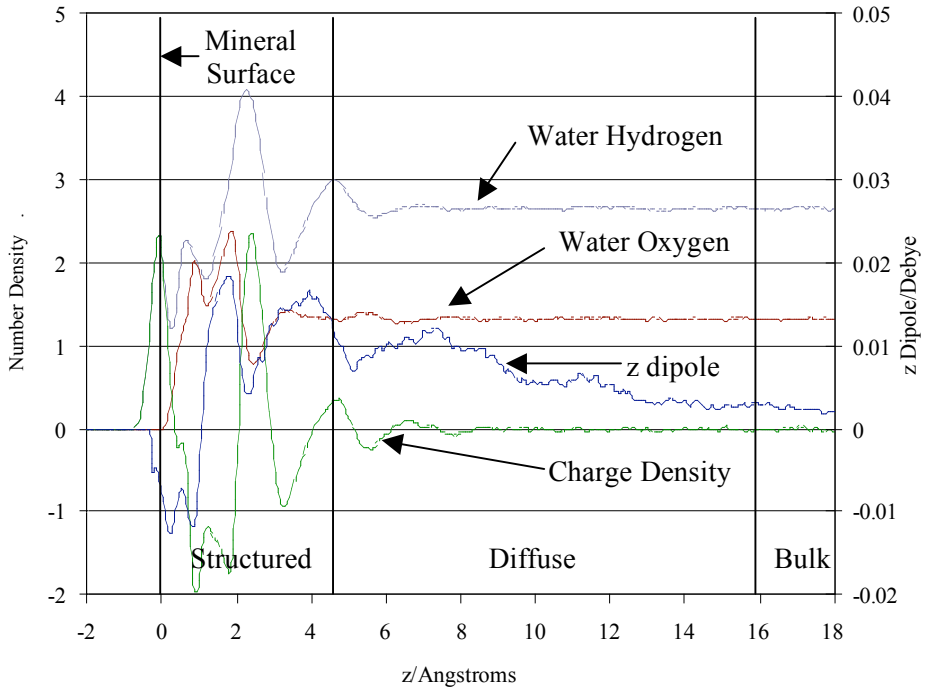

Figure III-5 (A Neutral, B Positive, C Negative): Atom number density, charge density, and projections of the z component of the water dipole for the neutral, positive and negative slabs. The x-axis corresponds to the vertical of the goethite-water slab shown in Fig. III-2: the goethite surface ends at 22 Å and 40 Å represents the midpoint of the H_2O in the simulation cell. The scale on the left axis corresponds to the H, O and charge densities. The scale for the z-dipole is provided on the right axis. The magnitude of the H_2O z-dipole is most strongly affected by the positively-charged goethite surface; note that the scale in B is 100x that in A and C.

a)

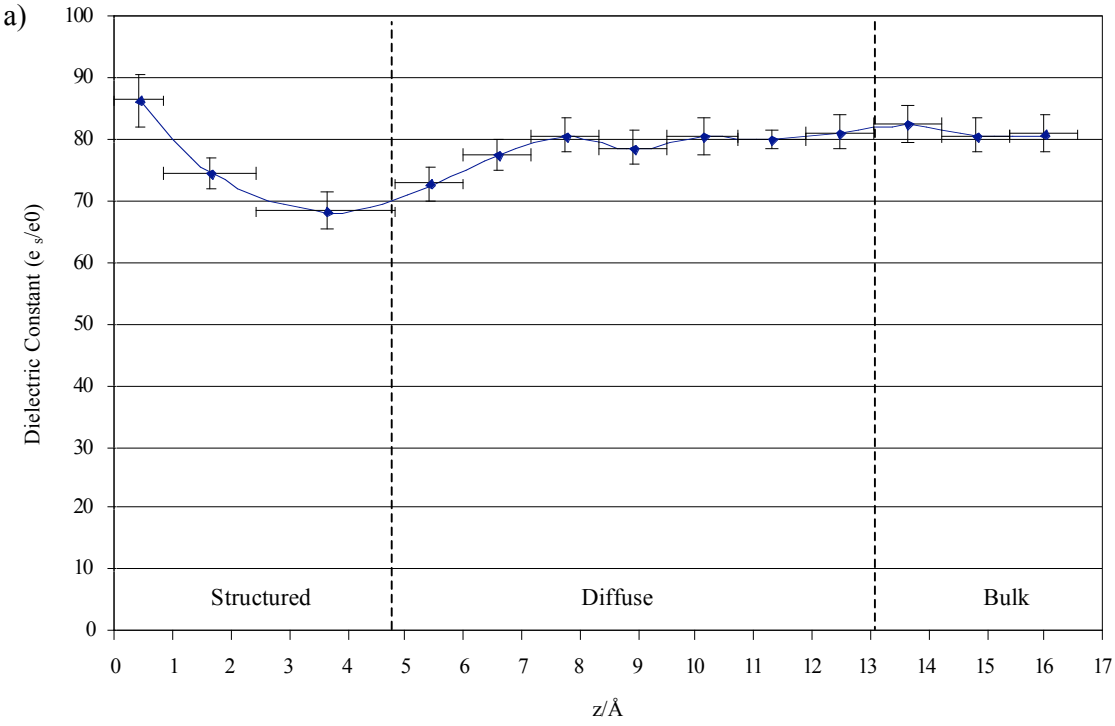
Dielectric Constant (e s/e0)
100
90
80
70
60
50
40
30
20
10
0
Structured
Diffuse
Bulk
0 1 2 3 4 5 6 7 8 9 10 11 12 13 14 15 16 17
z/Å

b)

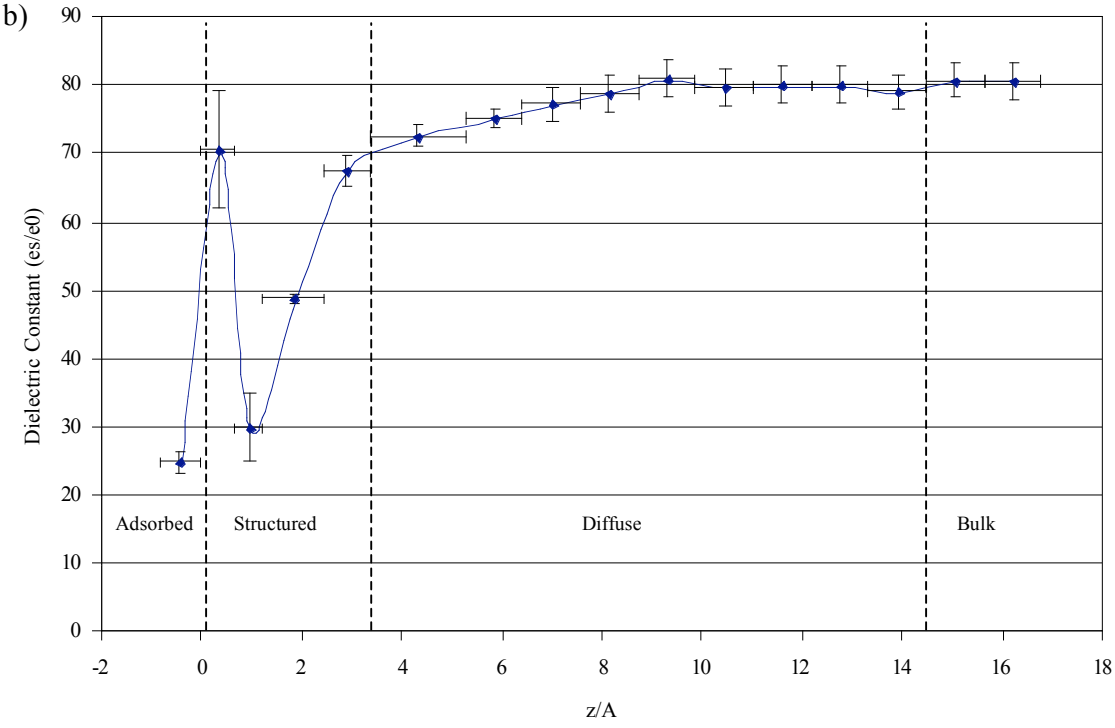
Dielectric Constant (es/e0)
90
80
70
60
50
40
30
20
10
0
Adsorbed
Structured
Diffuse
Bulk
-2 0 2 4 6 8 10 12 14 16 18
z/A

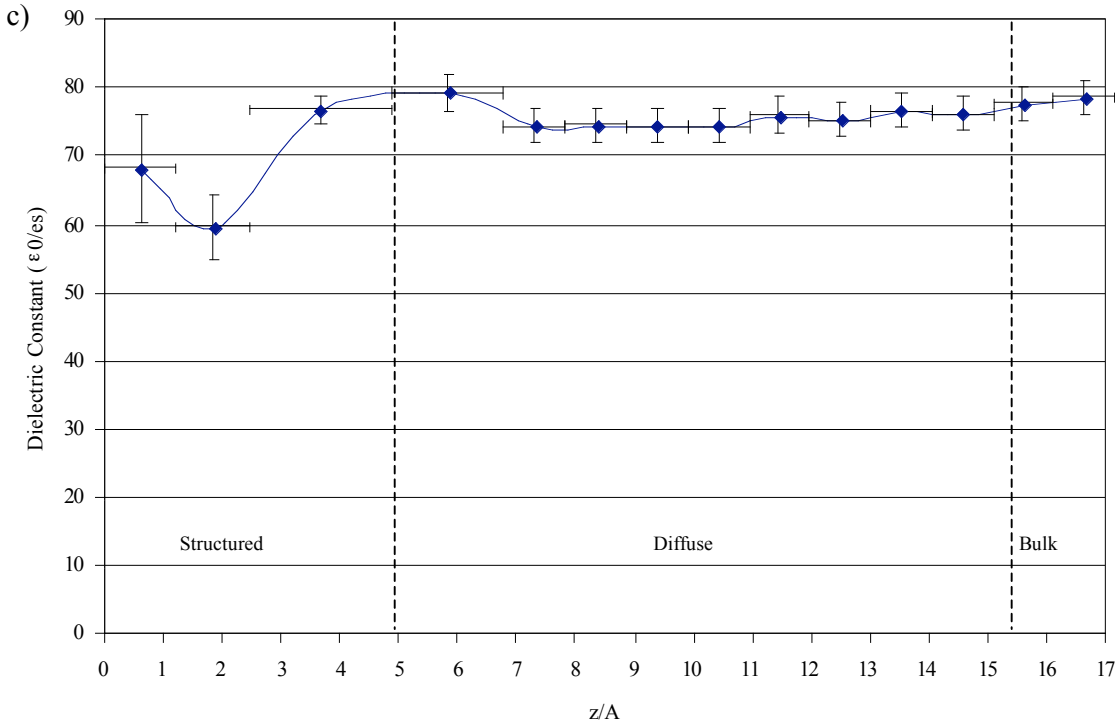

Figure III-6 (A top: Neutral, B middle: Positive, C bottom: Negative): Dielectric behavior of the water layers. Dotted lines indicate divisions between the different water types. The x-axis corresponds to the height above the surface (z), where z=0 is about 22 Angstroms on the box. The shear zone may be a transitional region with properties between those of the structured and diffuse regions.

A) Water Oxygen Slice 1 Neutral Slab

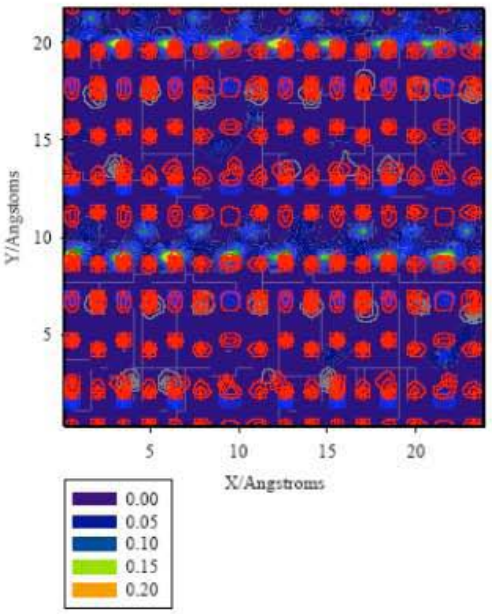

B) Water Oxygen Slice 2 Neutral Slab

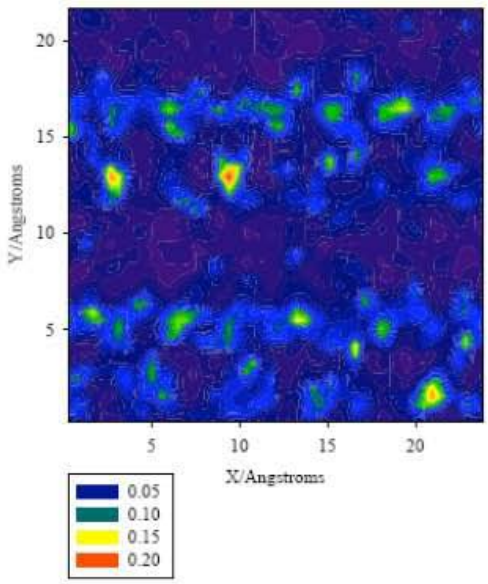

C) Water Oxygen Slice 3 Neutral Slab

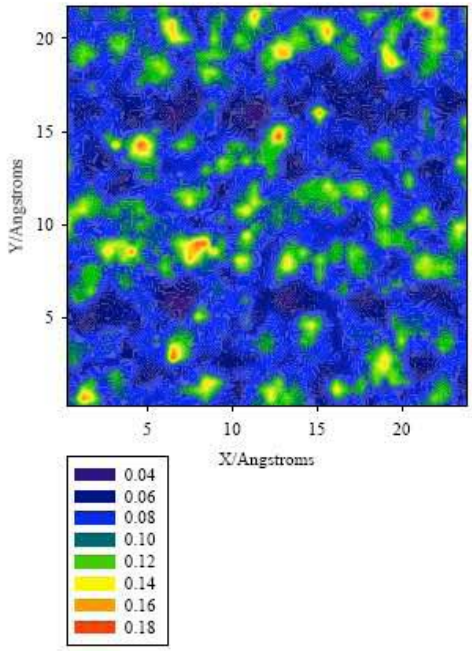

D) Water Oxygen Slice 4 Neutral Slab

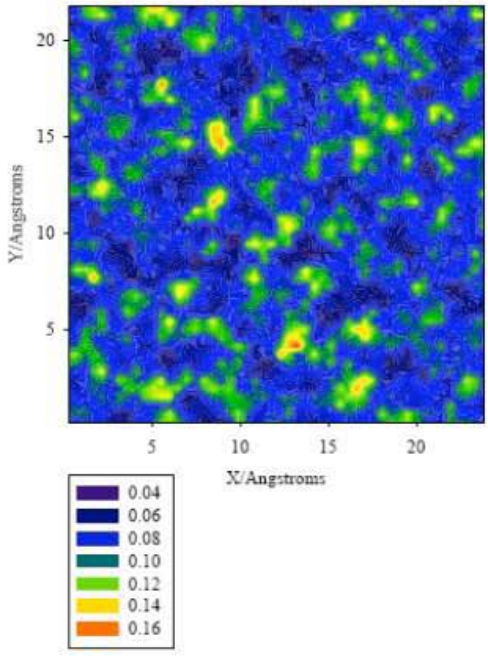

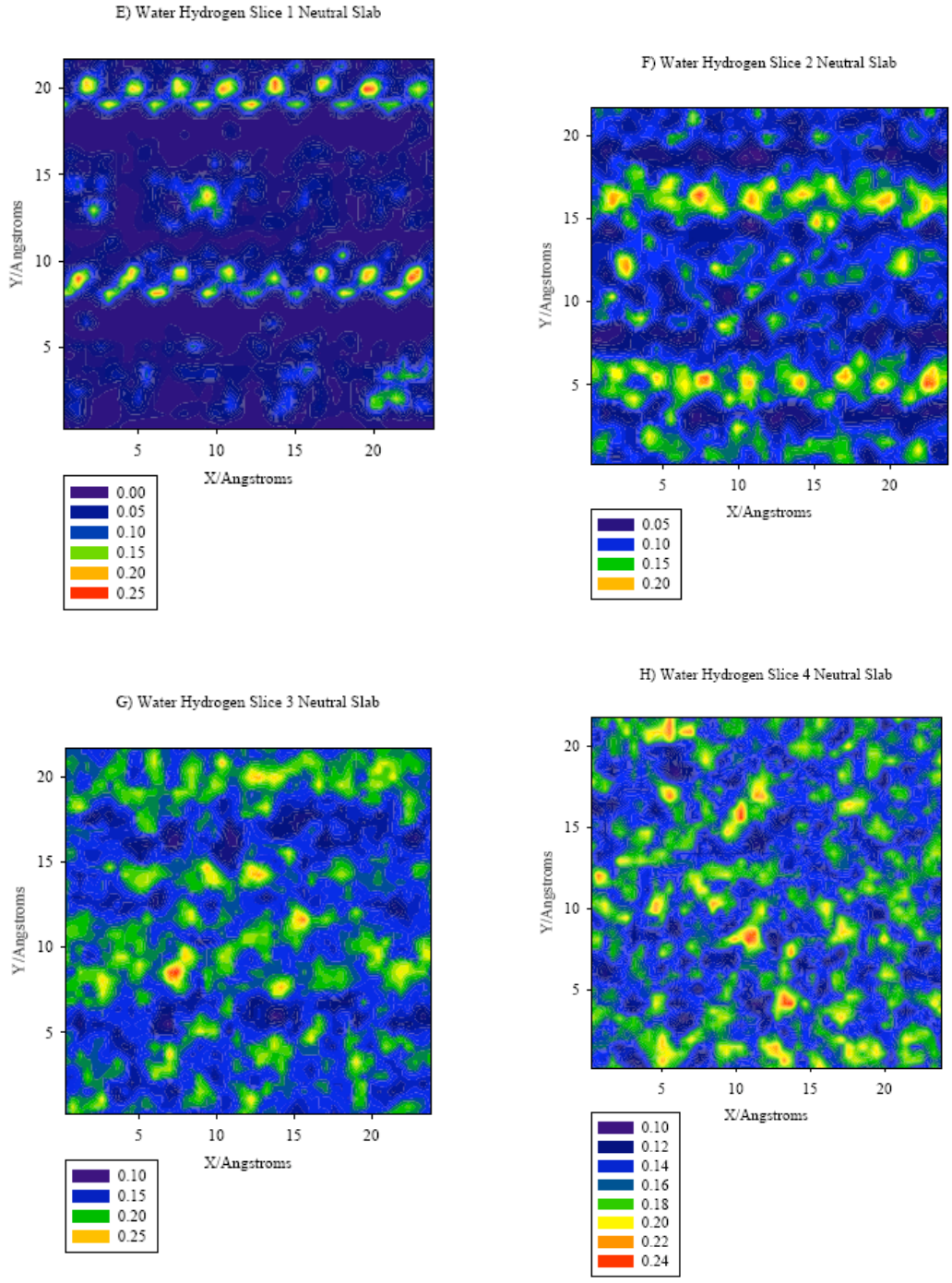

Figure III-7: Contour Maps of Water on the Neutral Goethite Surface. Figs. III-7A-D illustrate water structure based on the location of the water oxygen atoms and Figs. 7E-H illustrate water structure based on water hydrogen atom locations. For the oxygen maps, the vertical slice of the slab and corresponding thickness for each water layer from the goethite surface (z=0) are: A. 0Å – 0.9Å (0.9Å), B. 0.9Å – 1.5Å (1.5Å), C. 1.5Å – 4.0Å (2.5Å), and D. 4.0Å – 5.6Å (1.6Å), based on the oxygen atomic density peaks provided

in Fig. III-5A. For the hydrogen maps, the vertical slices and corresponding layer thicknesses, also determined from Fig. 5A are E. -1Å – 0.2Å (1.2Å), F. 0.2Å – 2.2Å (2.0Å), G. 2.2Å – 4.4Å (2.2Å), and H. 4.4Å – 6.0Å (1.6Å), respectively.

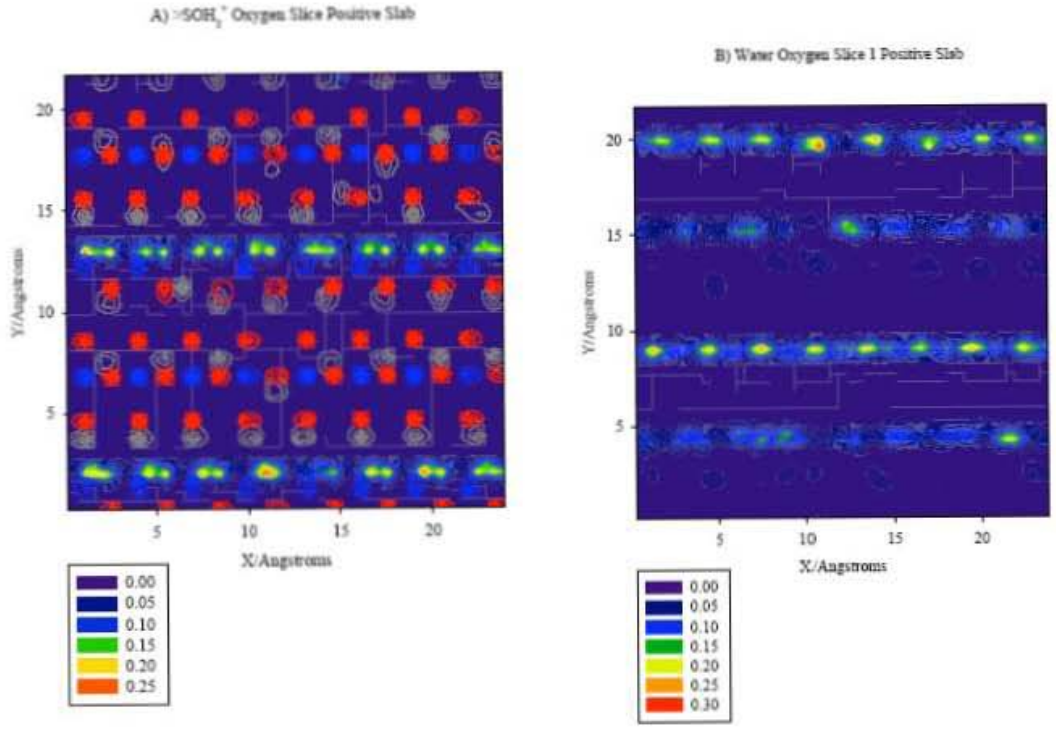
A) >SOH2+ Oxygen Slice Positive Slab
B) Water Oxygen Slice 1 Positive Slab
Y/Angstroms
X/Angstroms
5
10
15
20
0.00
0.05
0.10
0.15
0.20
0.25
0.30

C) Water Oxygen Slice 2 Positive Slab

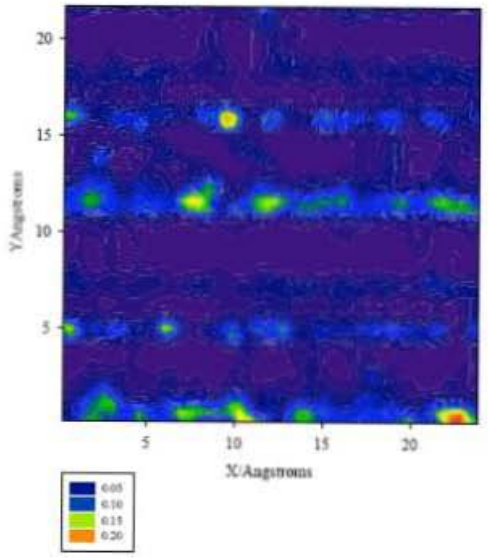

D) Water Oxygen Slice 3 Positive Slab

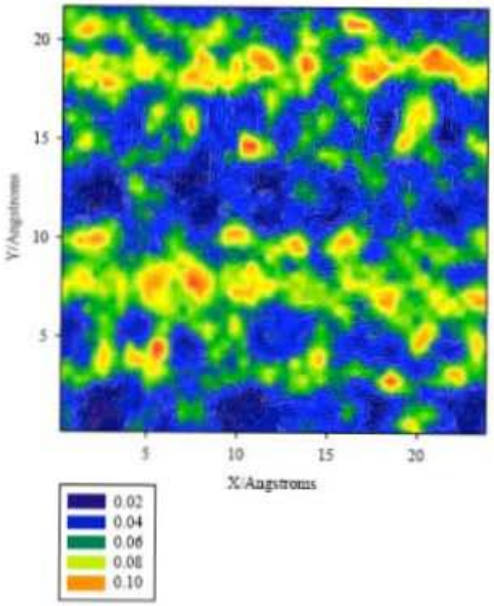

E) Water Oxygen Slice 4 Positive Slab

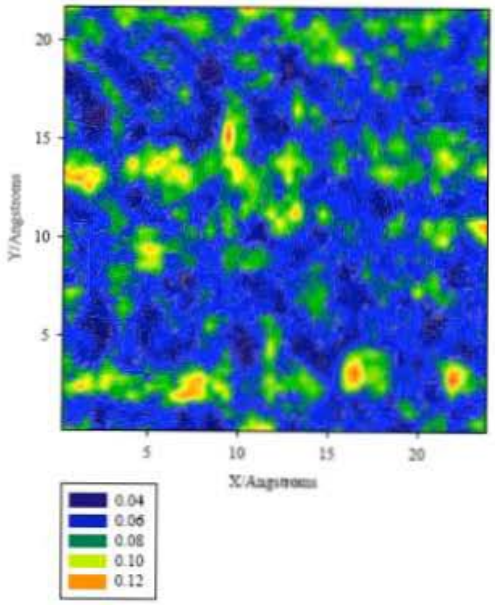

F) Water Oxygen Slice 5 Positive Slab

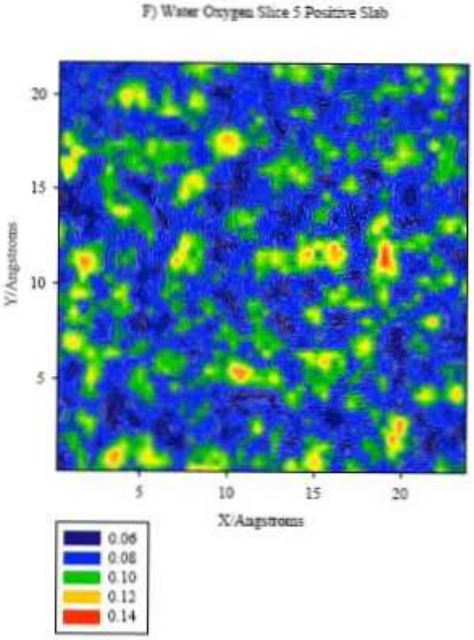

G) Water Hydrogen Slice 1 Positive Slab

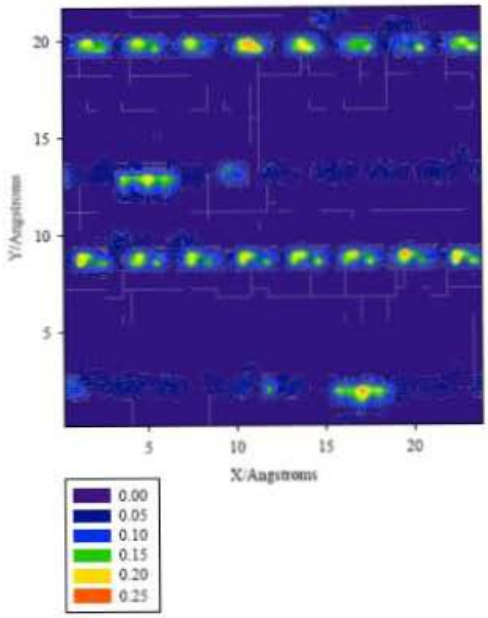

H) Water Hydrogen Slice 2 Positive Slab

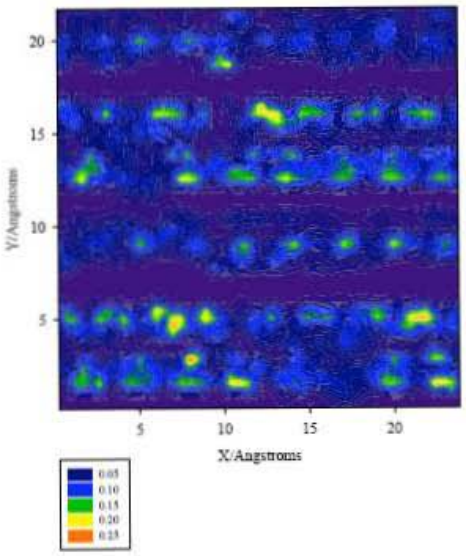

I) Water Hydrogen Slice 3 Positive Slab

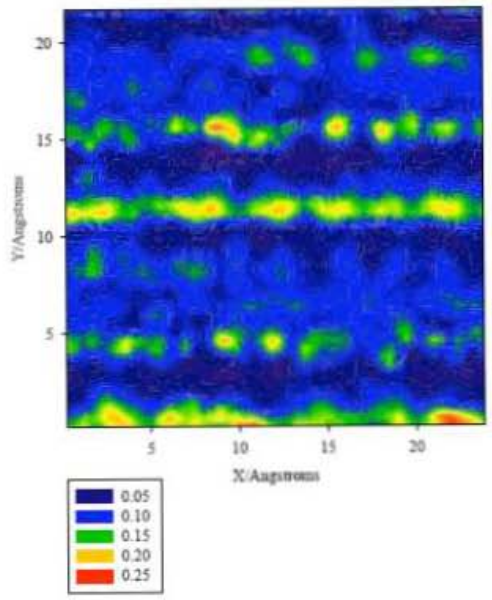

J) Water Hydrogen Slice 4 Positive Slab

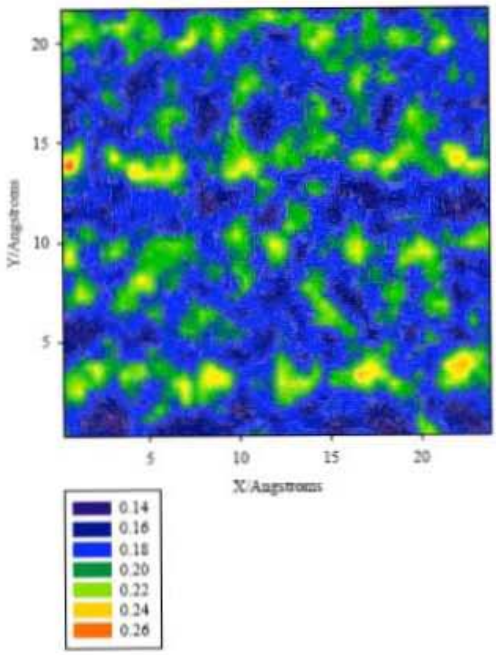

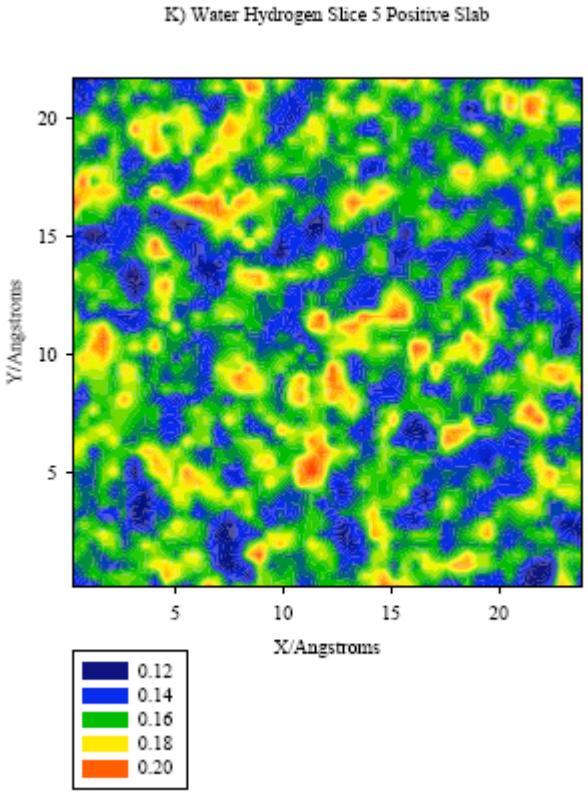

Figure III-8: Contour Maps of Water on the Positive Slab. Figs. III-8 A-F illustrate water structure based on the location of the water oxygen atoms and Figs. III-8G-K illustrate water structure based on hydrogen atom locations. For the oxygen maps, the thickness of each water layer in the z-direction is -1.6Å – 0Å (1.6Å), 0Å – 1.2Å (1.2Å), 1.2Å – 2.5Å (1.3Å), 2.5Å – 4.0Å (1.5Å), 4.0Å – 5.3Å (1.3 Å), and 5.3Å – 6.8Å (1.5Å). For the hydrogen maps: -1.7Å – -0.2Å (1.5Å), -0.2Å – 1.5Å (1.7Å), 1.5Å – 3.3Å (1.8Å), 3.3Å – 5.8Å (2.5Å), and 5.8Å – 7.2Å (1.4Å).

A) Water Oxygen Slice 1 Negative Slab

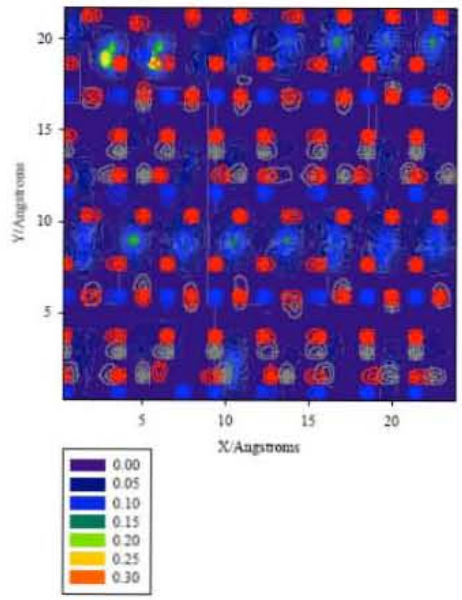

B) Water Oxygen Slice 2 Negative Slab

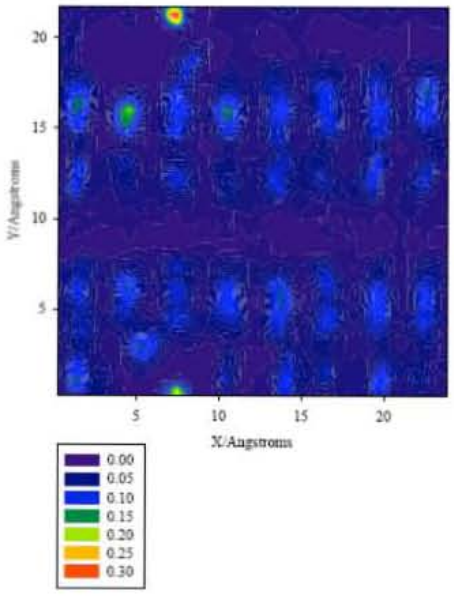

C) Water Oxygen Slice 3 Negative Slab

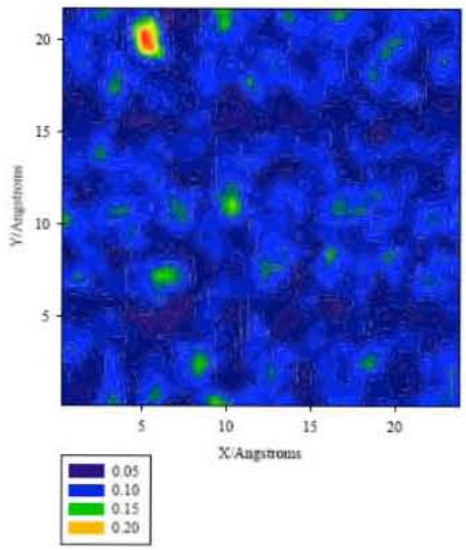

D) Water Oxygen Slice 4 Negative Slab

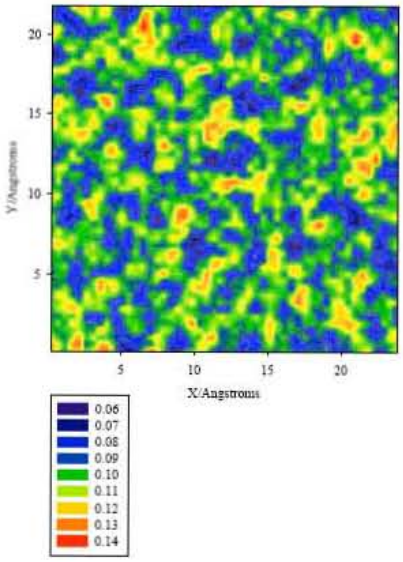

E) Water Hydrogen Slice 1 Negative Slab

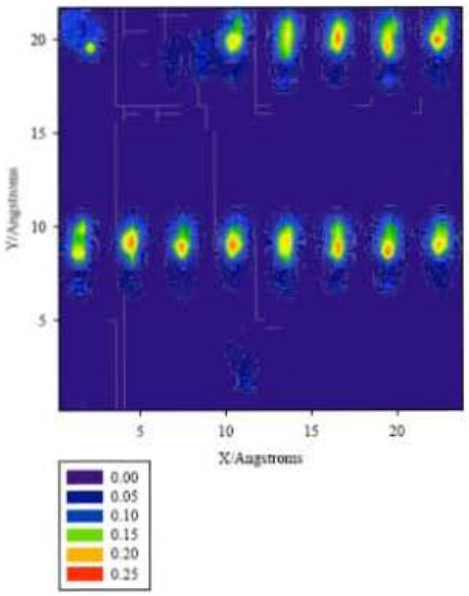

F) Water Hydrogen Slice 2 Negative Slab

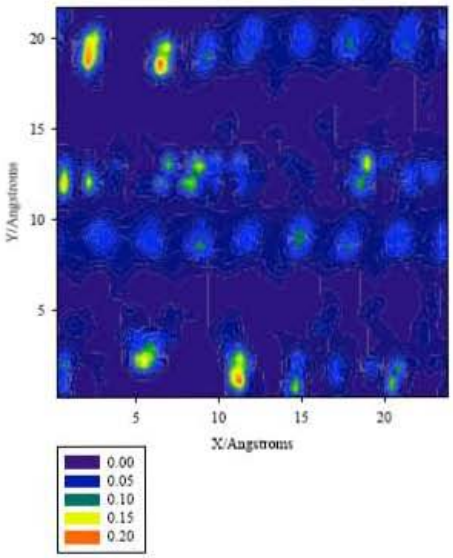

G) Water Hydrogen Slice 3 Negative Slab

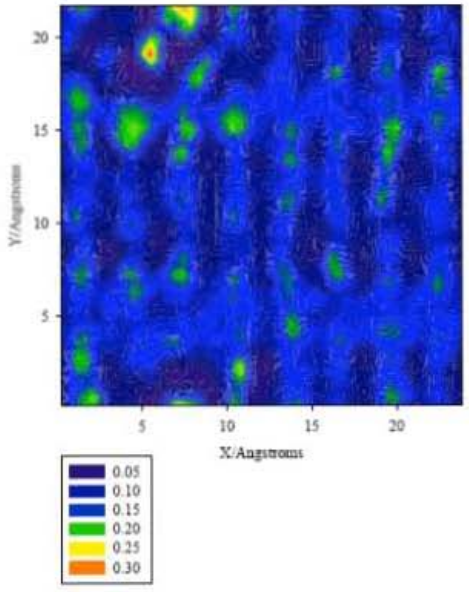

H) Water Hydrogen Slice 4 Negative Slab

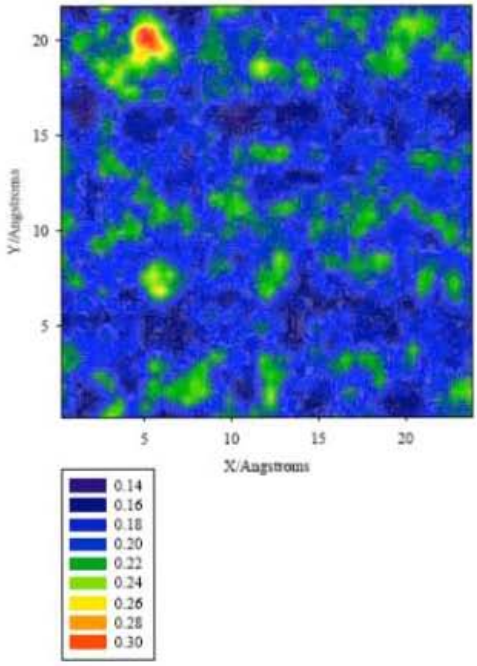

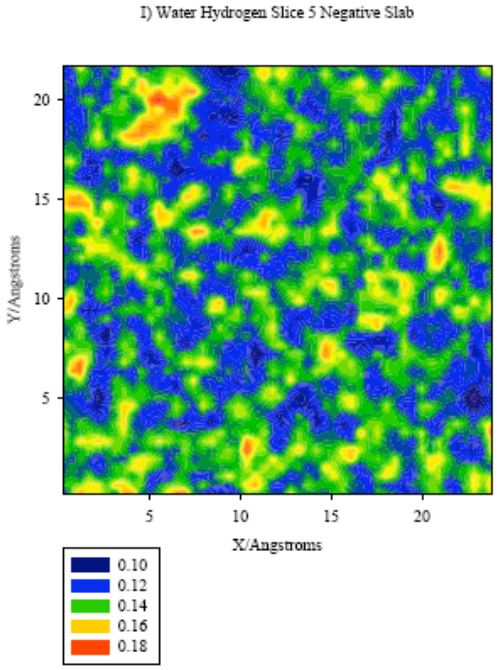

Figure III-9: Surface Maps for the Negative slab. The first four are the oxygen maps and the second four are the hydrogen maps. For the oxygen maps a) diagrams 0Å – 1.2Å (1.2Å), b) 1.2Å – 2.4Å (1.2Å), c) 2.4Å – 4.8Å (2.4Å) and d) 4.8Å – 6.7Å (1.9Å). For the hydrogen maps a) diagrams -0.7Å – 0.2Å (0.9Å), b) 0.2Å – 1.2Å (1.0Å), c) 1.2Å – 3.2Å (2.0Å) and d) 3.2Å – 5.9Å (2.7Å).

Reduction of N_2 by Fe^{2+} via Homogeneous and Heterogeneous Reactions

Part 1: evaluation of aqueous photochemical, pre-biotic pathways

Matthew C. F. Wander[1] and Martin A. A. Schoonen[1]

[1]Penn State Astrobiology Research Center(PSARC), Department of Geosciences, Stony Brook University, Stony Brook, NY 11794-2100

Abstract: Photochemical approaches appear ideally suited to the direct reduction of solvated nitrogen gas, because of their high kinetic barrier and thermodynamic favorability under moderately reducing atmospheric composition. Ferrous iron has been investigated as an electron donor, as it has a highly tunable redox character and is environmentally ubiquitous. Recent advances in environmental remediation have led to the identification of a class of materials that provide reductive potentials comparable to Fe(0). These materials are a set of reduced rusts of metallic iron whose redox couples are potentially capable of overcoming the kinetic barrier to the production of NH_3. In this study, we attempted to produce ammonia from N_2 by oxidizing white rust both photochemically and in the dark. All results indicate inhibition by competing reactions; primarily the reduction of H_2O to H_2. Due to the high thermodynamic energy of the $N_2^{-\bullet}$ intermediate, we conclude that aqueous photochemical reduction is an unlikely prebiotic source for reactive, *i.e.* reduced, nitrogen. Instead we turn to identifying a minimum temperature of rapid reaction based on a choice of reductant.

Key Words: Nitrogen Reduction, Photochemistry, prebiotic chemistry, ammonia, ferrous iron, heterogeneous, White Rust, Green Rust

Introduction: One of the many outstanding questions regarding the origin of life is how dinitrogen could have been converted to ammonia under moderately reducing conditions thought to have prevailed during the Hadean. This conversion is of importance as ammonia (and ammonium) are thought to be essential reactants in the formation of building blocks of life. Lightning could have produced nitrate and nitrite[256], the latter being easier to reduce to ammonia.[257-260] The potential for this mechanism alone to yield

sufficient quantities of ammonia for prebiotic synthesis of amino acids is unlikely[260]. Dinitrogen is generally thought to be by far the most abundant form of nitrogen in the atmosphere under moderately reducing conditions, but its reduction to ammonia is inhibited due to the strong triple bond in the dinitrogen molecule. Based on the realization that the rate of dinitrogen reduction on a moderately-reducing, prebiotic Earth may very well have been one of the severe limits on the origin of life, several abiotic mechanisms that may promote this reaction have been explored. After briefly reviewing proposed abiotic dinitrogen pathways, we will evaluate one of these proposed pathways, photochemical reduction of dinitrogen, in detail.

For reactions with high barriers, like the reduction of dinitrogen to ammonia and carbon dioxide to methane, a number of possibilities exist to overcoming that barrier. Each of these will alter the chemistry differently, changing the nature of the reaction process:

1) Change the thermodynamics: including altering the reductant or pH other reactant conditions which alter the side products.
2) Photochemically drive the reaction: this will not change the thermodynaics of the reaction but may help increase the kinetics of reaction.
3) Raise the temperature. This will speed up all reactions in the system and change the thermodynamics to a lesser extent.
4) Alter the nature of the barrier itself. This is a question of catalysis.

Primarily the focus in this work will be on 1 & 2. Without having to derive complex conditions to change the nature of the transition state we would like to know if the reaction can be driven by a combination of photochemistry and powerful reductants.

Dinitrogen reduction requires an electron donor. Over the years a number of electron donors have been proposed, including: Fe(II), S(-II), H(0), Fe(0). In the Haber-Bosch process, which is widely used to convert atmospheric dinitrogen to ammonia, atomic hydrogen is the reductant. In the process, molecular hydrogen dissociates over an iron catalyst to form atomic hydrogen. Potassium plays a role in catalytic enhancement in this process[261]. It is not clear that atomic hydrogen would be widely available on a moderately reducing prebiotic world; it is only likely as an short-lived intermediate of some reductive process. Sulfide emanating from submarine hydrothermal vents is abundant in those environments, but experimental work by Dorr and our group [262, 263] have shown that the reaction yields are far lower than expected on the basis of a total conversion of sulfide to sulfate. Instead Schoonen and Xu concluded that sulfur is the likely end product in the reaction. Overall the reaction of sulfide to sulfate, which has a large driving force, is not realized. This indicates that nitrogen reduction to ammonia, although thermodynamically favorable and spontaneous, can be inhibited kinetically, even at elevated temperatures of a few hundred degrees Celsius. This leads us to the hypothesis that photochemical approaches might have the potential to overcome the apparent barrier.

Combining sulfide, a powerful reductant and photochemical approaches could hold promise. A photochemical approach to the synthesis of prebiotic building blocks has shown potential for reducing C(IV) [264], but the yield of methane is limited to the estimated concentrations of available $S^{-2}_{(aq)}$. Since the barriers are similar the results are likely to be similar in the N_2 case. One important limitation that sulfide may have over iron is the inability to ligate the N_2.

Early attempts to produce reduced nitrogen under environmentally reasonable conditions have proven to produce very small yields for both dark and photochemical reactions. Attempts to reduce N_2 on magnetite and Fe(0) show inhibition by water in the dark [260]. Schrauzer and Guth [265], attempted nitrogen reduction via $Fe(OH)_{2(ppt)}$, an environmental corrosion product of Fe(0), also known as white rust both photochemically and as a dark reaction. They proposed a mechanism which would disproportionate $Fe(OH)_2$ into magnetite and Fe(0). Denisov et. al. [266] challenged their work soon after. Among the ambiguities in Schrauzer and Guth's work was whether or not borate was used as a buffer, in the nitrogen experiments or solely in the hydrogen synthesis. Systems containing $Fe(OH)_{2(ppt)}$ will robustly oxidize and produce H_2 in a large variety of water chemistry and pH ranges from 7-9 [267, 268]. Not until the discovery of green rust was the role of the buffer's anion understood [48, 269].

Green rust differs from white rust in two critical aspects: (1) it is solid material containing iron in both the ferrous and ferric state and (2) it has an aqueous interlayer with anions that balance the net positive charge within the brucite-like sheets. Its general formula is: $Fe(II)_2Fe(III)(OH)_6An(H_2O)_n$ where An = Cl-, ½ CO_3^{-2}, ½ SO_4^{-2} and potentially ½ HBO_3^{-2}. See chapter 1 for more detail. This phase has a large stability field relative to white rust [33, 59, 78]. Oxo-anion forms have the greatest reductive potential. A new mechanism for the Schrauzer and Guth reaction based on the thermodynamics by Trollard and Bourrrie [34] is presented,:

$$3Fe(OH)_2(ppt) \rightarrow Fe(II)_2Fe(III)(OH)_6An(H_2O)_n + e^-_{(aq)} \quad \text{where} \qquad (1)$$

$$\Delta G_{ox} = -45 \text{ kJ/mol}(An=Cl^-, \text{Oxid.} = 25\%)$$

$$\Delta G_{ox} = -105 \text{ kJ/mol}(An=CO_3^{-2})$$

$$\Delta G_{ox} < -105 \text{ kJ/mol}(An=HBO_3^{-2})$$

Ambiguity in the method employed is a critical loophole in Schrauzer and Guth's work. The controversy rests on the fact that the presence of significant amounts of borate in the experimental system could have led to the incorporation of the anion in the interlayer of green rust and, thereby, raising its reductive power. The above potentials are comparable to reduction by Fe(0), which has been shown to be sufficient to reduce N_2 at high temperatures [260, 270]. They exceed the range of thermodynamic reduction potentials encountered in biological systems.

$$R\text{-}MoFe_7S_9^{0} \rightarrow R\text{-}MoFe_7S_9^{+1} + e^- \qquad \Delta G_{ox} = -38.88 \text{ kJ/mol } [271] \quad (2)$$

A clear thermodynamic picture, afforded by eq. 2 above, allows us to benchmark the role photochemistry can play a role in aqueous environments. That is, any driving force more reducing than the above has the potential to reduce N_2. Whether in reality the reaction proceeds at a significant rate depends on the kinetics. A high activation energy may inhibit a thermodynamically favorable reaction. The presence of a catalyst may lower the activation energy.

A study by Shilov and coworkers illustrates the importance of catalysis in the reduction of N_2. While not conducted under environmentally relevant conditions, Shilov et. al. [272] showed the role that increasing the ionic strength of LiCl solutions has on the reduction of N_2. Binding the nitrogen to lithium in addition to the reducing metal center facilitates the reduction. The role of lithium in the reduction mechanism is unknown, but it is reasonable to speculate on the basis of his results that increased electrophilicity and reduced N-N bond strength are responsible. At present, we can only address this work and its suggestion that catalysis of the reaction through the formation of a complex that

weakens the triple bond in N_2 is a necessary condition in addition to providing a suitable reductant. On the basis of this second requirement, we postulate that only those photochemical reduction experiments in which the activation energy for N_2 reduction is lowered by binding the N_2 on a substrate have any of the potential to produce ammonia at a significant rate. Hence, the focus in this contribution is on heterogeneous photochemical systems. Of particular interest are systems with solid phases containing ferrous iron, which was abundant in seawater in the Hadean

Interest in white rust reduction mechanisms was renewed in the form of Fe/Mo/Ti solid solutions of the form $(Fe,Mo,Ti)(OH)_{2(ppt)}$ [273]. These experiments, performed in darkness at a pH=13.87, examined ratios of Fe and Mo for maximum N_2 production. NH_3 was produced in all cases where Mo $\geq$ 1%. It is important to note the similar ionic strengths to the Shilov paper, and that Mo is a superior N_2 ligator and reducer [274, 275]. For this mixed metal system reaction is essentially the same as eq. 1, and the oxidation states are +3 for both the Mo and Ti.

In summary, N_2 reduction by means of photochemical oxidation of Fe^{+2} and $Fe(OH)_2$ is largely unexplored and therefore a promising way to overcome the formidable the barrier to producing $N_2^{-\bullet}$ and $N_2H^{\bullet}$ radicals. Depending on the specifics of the redox environment, the overall reaction can be favorable. Photochemistry with its excitation of an electron to energies that can exceed those barriers has the potential to bypass adiabatic rate limitations. Photons excite electrons to excited states in the reactant molecules which can then follow adiabatic pathways down to ground states which are not necessarily the starting ground state (See figure IV-1). The combination of a thermodynamic favorability with high kinetic barriers makes this an ideal candidate for NH_3 production. Ferrous iron

oxidation is tunable: adsorption on ferric oxides and precipitation of $Fe(OH)_2$ are two extreme examples of reduction enhancement, with the latter lying outside the stability field for water. In this study we will examine a range of reductive forms of ferrous iron: $Fe^{+2}_{(aq)}$, Fe^{+2} adsorbed on Goethite, and $Fe(OH)_{2(ppt)}$ spanning a comprehensive range of reductive potentials both as photochemical and dark reactions; we can test the key hypothesis of direct photochemical reduction.

Methods

Our approach was a simple procedure designed to minimize sample handling and reduce ammonia contamination. It was necessary to eliminate both $O_{2(aq)}$ and its subsequent product $Fe^{+3}_{(aq)}$ as potential inhibitors of the redox chemistry of interest.

Materials

Glass and plastic tend to absorb ammonia, and washing increased ammonia contamination by substituting protons for Na^+ sites in the glass. The protonated sites would then absorb air-born ammonia. Therefore, all beakers, tubes, ion chromatograph (IC) capsules, and glassware not used for stock purposes were considered disposable.

Stock Solutions

All of the wet chemistry was performed in an anaerobic glove box, under a combined atmosphere of nitrogen and 1-3% hydrogen. The glovebox is equipped with two sets of pelleted palladium catalysts placed in a fan box to promote the rapid removal of any molecular oxygen from the atmosphere. Oxygen levels were continuously measured with a COY™ H_2/O_2 meter. Throughout the study the oxygen content in the

glovebox was kept below 0.01ppm, the detection limit of the meter. Solutions were prepared in the glove box with ultra-pure 18MΩ deionized water, which had been degassed of $O_{2(aq)}$ in the glove box by purging with U.H.P. N_2. Samples were removed from the glove box in 8ml Corning borosilicate glass tubes sealed with septum caps. The tubes are gas-tight for at least a few hours according to the manufacturer. Solution volumes were 5ml, leaving approximately 3ml of head space.

The stock $FeCl_2$ was green indicating that it contained enough Fe^{+3} to, possibly, inhibit reactions. Our solution to this problem was to equilibrate the $FeCl_2$ with Fe(0)[276]. In a 100 ml stock solution of 0.1M $FeCl_2$ we would add 1g of powdered Fe(0). Commercially available Fe(0) powder contains reduced nitrogen, specifically, in the case of Fisher, approximately 170ppm [260]. This could potentially increase background levels of NH_3 if the iron-bound ammonia was to be released. However, the Fe(0) settles to the bottom of the bottle. Given the limited solubility of Fe(0) and the short duration of the contact, it is unlikely that when the solution is extracted carefully by pipette from the top of the stock solution much F(0) would be pulled into the pipette. The dissolved N from the F(0) did not represent a significant contribution to the chemistry of our samples. Furthermore, the effect overall was trivial as it would be subtracted out using the following procedure. Every yield is calculated from a difference of final and zero sample each with exactly the same amount of initial Fe^{+2} solution and therefore with the same amount of ammonia contamination. A zero sample is produced exactly the same way as the final samples except that the sample is quenched by oxygen before any reaction either photochemical or dark is allowed to proceed.

The other stock solutions were 0.1M H_3BO_3, 0.1M $NiCl_2$, and 0.1 M KOH. They were made by weighing an appropriate quantity of powder and mixing it in 100g of deionized water.

Goethite was synthesized according to the procedure outlined by Schwertmann et al. [277], which was reported to produce a surface area of approximately 90m^2/g. No surface area measurements were taken.

Experiments

Solution compositions were designed in PhreeqcI with a buffer concentration to have a pH of 8 or 9. No actual pH measurements were taken at any time during the experiment. This was because any pH measurements would have been less accurate and potentially exposed the samples to O_2 and CO_2. This leaves open the possibility of pH fluxuations during the experiment. These would have been buffered by the borate and so were unlikely to be important.

Each run had a total solution volume of 100ml, divided into 5ml samples. For each experimental condition there were three different treatments (dark, UV-illuminated, and zero). Each treatment was conducted in triplicate. Hence, for a given experimental conditions a total of nine tubes with the same composition were prepared. Reported yields are differences between zeros and final results for dark and UV-illuminated experiments, respectively. A zero result was prepared identically as the final samples, including identical amounts of stock solutions and in the same tubes. The only difference was that the zeros were exposed immediately to oxygenated atmosphere after removal from the glove box in order to inhibit any possible reaction. Time from removal from the

glove box to the analysis in the IC was approximately the same for both the zeros and the final results samples. Photochemical exposures were four hours long unless stated otherwise, and dark reactions were 24 hours long. The concentration of the goethite slurry was 17g/L, and the volume used in all cases was: 1μL as measured by pipette.

The UV lamp setup consisted of a 450W medium pressure UV Hg arc lamp, which rested in a quartz immersion well water jacket (ACE glass, Vineland, NJ), with continuous water circulation through a chiller. This chiller actively maintained the temperature of the water at 25(2) ^{o}C. The tubes were held upside down in a rotating carousel to minimize loss of volatiles. The rotation of the carousel ensure every tube received equal light exposure. The selection of borosilicate tubes limited the light frequencies to 300 nm or less, or about 300 kJ/mol. This reduced the intensity somewhat and limited our light to frequencies with good depth penetration in the ocean. Light below 300 nm penetrates anywhere from 10 m to 100 m in the ocean depending on sediment loading [278]. This would provide environmentally reasonable light conditions as the Pyrex™ in the tube mimics overlying sea water.

Analysis

Ammonia analysis was performed on a Dionex DX500 Ion Chromatograph with a CS-16 column. This column was selected for its high selectivity for ammonia. The column has the ability to separate ammonium in a sodium-rich solution up to a ratio of 1:10,000 NH_3-Na. This was essential as stock chemicals contain enough Na^+ to interfere with detecting sub-micromolar NH_3 separation on a standard column. While sea water possesses similar ionic strengths to those in the Shilov paper [272], sodium obstructs signals

from ammonium, and even the CS-16 column would not be able to perform the separation. With the CS-16 column our lowest quantifiable concentration was ≈0.5μM, and our experimental errors were on the same order ≈ 0.1 - 0.3μM. The actual sodium was on the order of 10 μM.

Results

Table IV-1 summarizes the results of the various combinations of reactants tested. These results indicate the failure of photons to further the reduction of $N_{2(aq)}$ to NH_3 under the studied conditions. 100% reduction would correspond to 0.7mM ammonia. However, dark reactions showed productivity though in amounts that would not be considered significant. This is observed in reactions 3 and 6, in table IV-1. In particular, the production in reaction 6 is nearly three times the uncertainty almost enough to be considered qualitative production less that 1% yield. Furthermore, direct reduction of N_2 by ferrous iron at STP (25^{o}C, 1 atm) is unlikely to produce more than trace quantities of NH_3. Both the final results and the zeros are differences of small but quantifiable amounts of ammonia. In most cases the differences were insignificant.

Discussion

It is known that H_2 is produced via the oxidation of ferrous iron compounds photochemically [276] and by white rust as a dark reaction [279], so the reduction of protons is, potentially, a competing reaction. The thermodynamics of hydrogen atom radical formation and solvated electrons have been determined [280, 281] and can be compared to an estimate of the thermodynamic energy requirements of N_2 radical production [282].

Solvation of the electron is not a competing reaction, but it is worth consideration as any system which is capable of reducing water will have no control over the products produced [280, 281]: c

$$e^- + H^+_{(aq)} \rightarrow H^{\bullet}_{(aq)} \qquad \Delta G=221.0kJ/mol \qquad (3)$$

and

$$e^- + N_{2(aq)} \rightarrow N_2^{-\bullet}{}_{(aq)} \qquad \Delta G\approx299kJ/mol \qquad (4)$$

and

$$e^- + H_2O_{(l)} \rightarrow H_2O^{-\bullet}{}_{(aq)} \qquad \Delta G=274.5kJ/mol \qquad (5)$$

Even in alkaline media $Fe(OH)_2$ appears to reduce protons faster than it reduces N_2. Photochemical excitation could enhance this competing pathway; exciting electrons from d orbitals on the iron to σ* OH anti bonding orbitals. This would break the oxygen-hydrogen bond leaving Fe-O and a hydrogen atom. The fact that the ΔG of reaction for solvating H radicals is significantly lower than either of the N_2 radical species indicates that competition by H^+ in any aqueous system, whether a dark reaction or a photochemical reaction, will be significant. This will be explored further in part two where we will examine the kinetic barrier to the reduction of N_2. Raising temperature or ionic strength may help, but this still relegates this class of reactions to niche environments in the pre-biotic earth.

Photochemical and dark reactions at STP failed to reduce N_2. While the production of NH_3 was not significant in experiment 6 in table IV-1, it may indicate that this reaction has potential to operate at higher temperatures. As such, the emphasis must shift to lowering the temperature where nitrogen reduction can occur by changing the reductant. The temperature of this transition is called a closure temperature; below that

temperature the system is closed or blocked to a particular reaction. This closure temperature can be derived from introductory chemical kinetics. Starting with the standard rate expression $k=Ae^{-Ea/RT}$ and rearranging it we get $T = Ea/R(\ln A - \ln k)$. Assuming a value of k=1M/s for fast equilibration, and setting $A=10^{13}$, we get a good upper limit of the critical temperature for redox equilibration:

$$Tc \approx 4Ea(^{o}K/(kJmol^{-1})) \quad (6)$$

Tc is the temperature above which the reaction becomes possible, and Ea is the overall reaction barrier. At a value of 3Ea the kinetics are sluggish; in environmental conditions it is likely to show some disequilibrium, but over longer geologically relevant time periods should show equilibrium. This result, general to any redox disequilibrium, is of particular interest to this problem. Given the half-cell energies presented above we can estimate that since the initial reaction is extremely uphill we can use the initial ΔG_{rxn} in conjunction with equation 1 to estimate the closure temperature for a variety of potential reactants:

$$\Delta G_{rxn} = \Delta G_{red} + \Delta G_{N2\text{-}N2\bullet} \quad (7)$$

ΔG_{rxn} is the approximate Ea of the barrier height, and the total energy of reaction for the first ET step, ΔG_{red} is the half-cell energy of oxidation for our reductant of interest (*e.g.* $Fe^{+2}_{(aq)}$, $Fe^{+2}_{(ads)}$, $Fe(OH)_2$ etc.). $\Delta G_{N2\text{-}N2\bullet}$ is the value of equation 4. This allows us to examine Tc in terms of individual reductants:

$$Tc = 4*(\Delta G_{red} + 300)(^{o}K/(kJmol^{-1})) \quad (8)$$

We can see that adsorbed Fe^{+2} with a ΔG_{red}=-25kJ/mol at pH 7 (Data from: [283]) would have an approximate closure temperature of 1100°K and $Fe(OH)_2$ would have one of 480-1000°K, depending on available anions. The lower end estimate would apply to the

Schrauzer and Guth result for GR-borate. These then can be compared to estimates of Hadean temperature with its "hot" ocean. Temperature estimates for the ocean are from 100°C [284] based on surficial boing point estimates to 350°C for modern hydrothermal vents [280, 281, 285]. Experimental dinitrogen reduction has been studied any where from 100°C to 1000°C with particular emphasis on the range of 300 °C to 800°C [270]. Even at hydrothermal vent conditions, we still only have a small set of acceptable redox couples, even considering that salinity would reduce this temperature. However, high temperature works differently than photochemistry, photons can swamp certain pathways over others while high temp each pathway is followed equally.

Conclusion

Even under what should be ideal conditions photochemical reduction of dinitrogen by ferrous iron does not proceed, indicating that as a possibility for prebiotic synthesis it is not a likely mechanism. Given the failure of photochemistry on this set of ferrous iron reagents, it is clear that N_2 production from white rust or other pure ferrous iron oxidation must occur only under hot, saline, and low CO_2 conditions. While the temperature is substantially lower than that of many other reactions, it is still hot enough to limit it to hydrothermal vent systems. Increasing salinity will lower the temperature of redox equilibrium, but with little effect. Trace metals capable of binding N_2 are essential to reducing the temperature to near STP. While 1% Mo incorporated in $Fe(OH)_2$ has proven to promote the reaction, it is unreasonable to expect Mo to be present at sufficiently high levels in the Hadean oceans to promote the reaction by producing Fe-Mo solids. The precipitation of carbonate phases represent an additional constraint. If

dissolved CO_2 concentration is greater than about 1 mM then siderite production will dominate over white rust, a valid concern at the higher end of predictions of between 1 to 10 bars CO_2 [286]. These factors relegate this process to niche environments within the oceans, and suggest that direct N_2 reduction is a minor player in the production of ammonia in the prebiotic earth, which is unlikely to be dominated by any one process.

Acknowledgements: NASA Astrobiology support via PSARC

Table IV-1: Results for the photochemical reduction of N_2.							
Solution	ml of 0.6M H_3BO_3	ml of 0.1M $FeCl_2$	ml of 0.1M KOH	~pH	Light (hν)	Solid Phase	Yield/μM
1	0.6	0.1	0.2	8	Yes	No	0.07±0.14
2	0.0	0.1	0.2	8	Yes(1hr)	No	0.13± 0.14
3	0.0	0.1	0.2	8	No(1hr)	No	0.61± 0.52
4	0.0	1.1	2.0	8.7	Yes	$Fe(OH)_{2(ppt)}$	0.00± 0.18
5	1.0	1.1	2.2	8.7	Yes	$Fe(OH)_{2(ppt)}$	0.22± 0.22
6	1.0	1.1	2.2	8.7	No	$Fe(OH)_{2(ppt)}$	1.41±0.50
7-(75% Fe-25% $NiCl_2$)	0.0	0.75/0.25	2.2	8.7	Yes	$Fe(OH)_{2(ppt)}$	0.28± 0.23
8	0.6	0.1	0.2	8	Yes	Goethite	0.01± 0.25
9	0.6	0.1	0.2	8	No	Goethite	0.18± 0.42

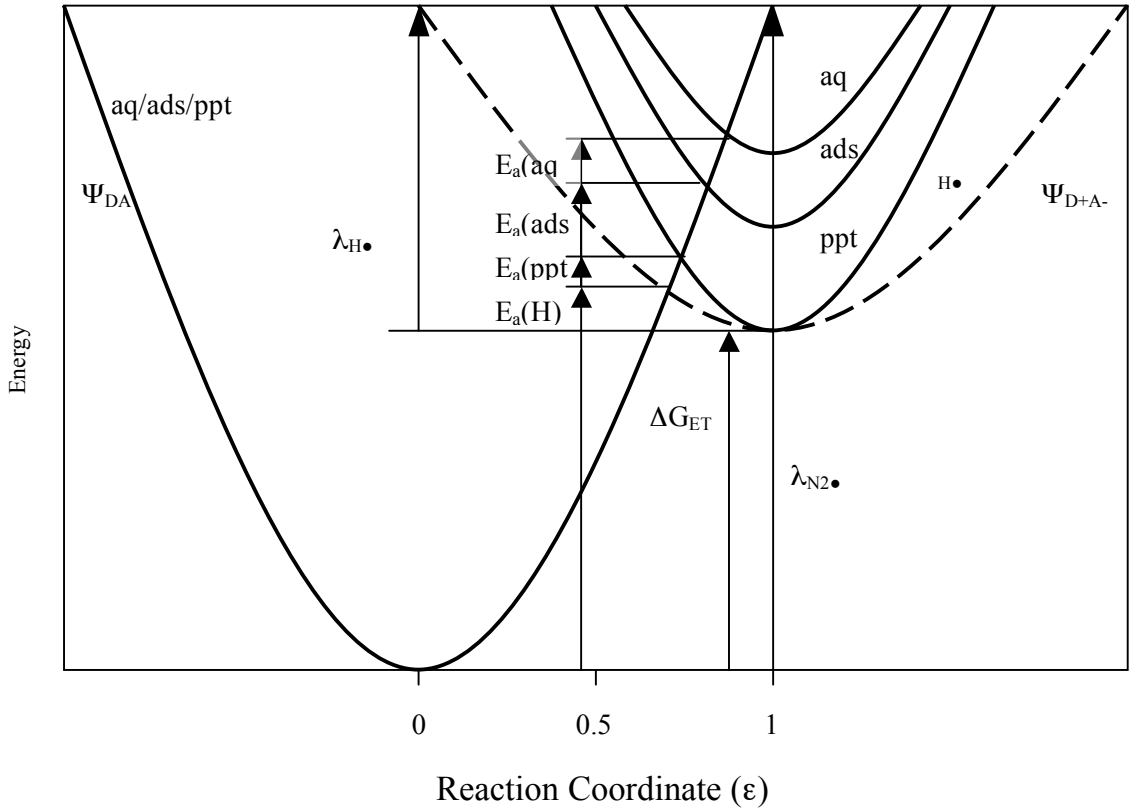

Figure IV-1: Demonstrating the effect of changing the reductive potential of iron on the reaction to produce N_2 radicals. As the thermodynamic energy is reduced to produce those radicals the kinetic barrier drops as well. However, due to the extraordinarily high reaction barrier to produce those radicals this reaction will always be out competed by reactions with a lower reorganization energy such as $H^+ + e^- \rightarrow H^\bullet$ because that reaction kinetic barrier drops as well. In this figure Ea refers to the activation energies of each of the energy reactions: ppt refers to $Fe(OH)_2$, ads for Fe^{2+} on goethite, and aq for aqueous Fe^{2+}. l refers to the electronic reorganization energy for the reacton which controls Ea in conjunction with ΔG. F is the energy of the two state reactants and products designated by DA and D^+A^-.

Reduction of N_2 by Fe^{2+} via Homogeneous and Heterogeneous Reactions Part 2: a Theoretical comparison of abiotic and biological requirements

Matthew C. F. Wander[1], James D. Kubicki[2], Martin A. A. Schoonen[1]

[1]PSARC, Department of Geosciences, Stony Brook University, Stony Brook, NY 11794-2100

[2]Department of Geosciences and the Earth & Environmental Systems Institute

The Pennsylvania State University, University Park, PA

Abstract: Nitrogen reduction by ferrous iron has been suggested to be important in the formation of ammonia on early Earth. In this paper, we examine the effect of adsorption of ferrous iron onto a goethite substrate on the thermodynamic driving force, and possibly the kinetics, of a ferrous iron-mediated reduction of N_2. Sorption of iron on a surface such as goethite alters the oxidation products and as a result the thermodynamic driving potential. Utilizing density functional theory (DFT) and Marcus Theory of Proton Coupled Electron Transfer (PCET) reactions, it is possible to characterize the differences between the following two reactions:

$$Fe^{2+}_{(aq)} + N_{2(aq)} + H_2O_{(aq)} \rightarrow N_2H^{\bullet} + FeOH^{2+}_{(aq)}$$

and

$$\equiv Fe^{2+}_{(ads)} + N_{2(aq)} + 2\ H_2O_{(aq)} \rightarrow N_2H^{\bullet} + \alpha\text{-}FeOOH_{(s)} + 2H^{+}_{(aq)}$$

While the rates of both reactions are essentially zero at 298°K, we have determined that adsorption simply alters the thermodynamic driving force for the reaction but has no other effect on the direct ET kinetics. It is possible to utilize the failure of simply altering the thermodynamic driving force to reduce dinitrogen, in order to make mechanistic connections between possible prebiotic pathways and existing mechanisms for biological N_2 reduction. The key to reduction in both cases is N_2 adsorption to multiple transition metal centers in competitive conjunction with hydrogen production.

Key Words: DFT, Marcus theory, heterogeneous redox, nitrogen reduction, ammonia, prebiotic chemistry, nitrogenase, iron, goethite.

Introduction: The possible prebiotic reduction of N_2, and breakage of the N≡N triple bond by iron, is compelling because ferrous iron is a ubiquitous reductant. The weak standard reduction potential of $Fe^{2+}_{(aq)}$ stands in stark contrast to its central role in

biological activity [287]. Environmental mechanisms for direct N_2 reduction do exist, but all have severe limitations which eliminate the possibility of any of them being more than just niche reactions. First reduction, of N_2 by metals at high temperature and pressure by H_2 gas, the Haber-Bosch process, was the critical industrial source but unless this is a source of mantle out gassing, it is irrelevant; even then extremely high temperatures favor N_2 over NH_3 [262]. Further work with metallic iron has promise, but in excess of 800^oC [288]. Work on mixed metal ferrous hydroxide rust are promising when Mo or V is included [273, 289]. A third series of work focused on N_2 bridged between ferrous iron and lithium in solutions with 0.2 M to 1 M Li. The proposed structure, in this case, was a lengthwise bridge; the high Li concentrations utilized to overcome the suspected weakness of N_2 as a ligand [272]. Sulfide will reduce N_2 but with only limited yields [262, 290]. Further work on magnetite and Fe(0), showed inhibition by water [260, 270]. Taken together, these studies indicate that there is no dominant, direct reduction pathway to ammonia.

Mechanistic examinations have been speculative; putting N_2 into a classical Electron Transfer Marcus theory paradigm in order to understand precisely why some modes work while most fail has proven problematic [291, 292]. The first step is to try to define the nature of the electron transfer; whether the reduction is through an outer-sphere mechanisms where the donor (Fe) and receptor (N_2) are not bound to one another; or a variety of inner-sphere mechanisms, with N_2 ligated to Fe(II) and N_2 sandwiched between two Fe(II) atoms either lengthwise or side-on. These latter mechanisms present the possibility for destabilization of the N_2 triple bond, a critical consideration given the enormous kinetic barrier to the production of $N_2^{-\bullet}$ radicals. A key consideration in any prebiotic environmental mechanism is to understand how it might connect to the

mechanism of biological nitrogen reduction. Biological systems do not emerge from nothing; their underlying chemistry must follow in some way from available analogues.

The key to understanding the evolution of nitrogenase's reductive mechanisms may lie in nitrogenase's reductive mechanism, in so far as it is possible to return to a strict Marcus theory/ET framework see figure V-1. Three mechanisms for nitrogenase's reductive process will be discussed: hydrogen atom/hydride addition, Mo binding, and multi site binding. All of these mechanisms fit with what little is known about the nitrogenase cofactor experimentally [293-297].

Hydrogen addition is probably the most widely examined mechanism in recent years and follows from the discovery of a central ligand believed to be fixed at the core of the nitrogenase MoFe structure [293, 298-302]. It was first speculated that this atom was nitrogen. This would have interesting mechanistic implications given that the nitrogen would have to be fixed in the structure [303-305]. While this central atom was eventually shown to be either O or C [306, 307] a framework for an H-atom transfer class of approaches had developed. This began with an examination of favorable adsorption sites on the FeMo cofactor [299, 308-310]. H atom and H- transfers to the N_2 were studied [293, 300] under the basic principle that in an inner sphere mechanism, it was possible to bypass the N_2-intermediate by jumping directly to N_2H^- as follows:

$$R\text{-}MoFe_7S_9{}^0 + N_{2(aq)} + H^\bullet \rightarrow R\text{-}MoFe_7S_9{}^{+1} + N_2H^- \quad [271] \qquad (1)$$

This is, potentially, a one electron transfer because it uses the hydrogen as an atomic unit within the inner-sphere framework. While certain to be high, it is not clear what the kinetic barrier for such a reaction is, but it is not an a priori impossibility. The hydride reaction is similar, but requires the prior formation of a hydride:

$$R\text{-}MoFe_7S_9^0 + N_{2(aq)} + H^- \rightarrow R\text{-}MoFe_7S_9^0 + N_2H^- \quad (2)$$

While complicated, requiring the simultaneous arrival of three different species, they bypass the $N_2H^\bullet$ barrier.

A second class of reactions focuses on the binding qualities of Mo [311-314]. Mo is a superior reductant of N_2 to iron due to its bonding properties [274]. In this mechanisms the N_2 binds directly to the Mo [315, 316]. These mechanisms can involve π-Mo-N bonded intermediates [311]. F-orbitals on the metal can bind to π* orbitals and stabilize them relative to the HOMO, lengthening the N-N bond [317]. Mo binds edge on rather than end on in the case of iron in most chemically relevant forms [275]. N_2 binding to Mo has been proposed early on due to the superiority of Mo and V nitrogenases over pure Fe nitrogenases.

The multi-site binding model is, perhaps, the most intuitive, but is also probably the least explored. If binding to one metal could reduce N_2 in a limited way, and two metals can produce stoichiometric but not catalytic reduction [318], then the more metals that can bind to N_2 the more reductive potential there is [319]. In this approach, the FeMo cofactor opens up partially releasing the central atom [320, 321]. This allows for the N_2 molecule to be bound to a minimum of 3 Fe atoms, each of which helps in the reduction by destabilizing the triple bond [322].

In this work we will apply robust Marcus theory approaches to two simple classes of N_2 reduction reactions: homogeneous and heterogeneous. The purpose of this is to elucidate the role in heterogeneity in the direct ET. We will further this with some simple ET reactions in order to draw comparisons with prebiotic analogues to the nitrogenase mechanism.

Methods

Our approach was to utilize hybrid DFT techniques and Marcus Theory [194] to model the first electron transfer step of the N_2 reduction reaction. This was done in order to evaluate rate kinetics for the reaction, and half-cell reaction energies for the radical formation. The Marcus Theory treatment is abbreviated for the redox reactions studied. Solvent components to the reaction barriers were not computed due to the high barriers of reaction.

Hybrid DFT methods were utilized to optimize the geometries of both reactants and products via energy minimization. These stable states were then connected by linear synchronous transit (LST) [186] to approximate the reaction pathway. LST works by taking single point calculations on geometries that are interpolations between the reactant and product geometries. The formula for the interpolations in internal coordinates:

$$X_n = \varepsilon X_p + (1-\varepsilon)X_r \quad (3)$$

where X is the atom coordinate (bond, angle or dihedral), n is the intermediate, r is the reactants, p is the products, and ε is the extent along the reaction coordinate measured as a fraction of 0 to 1. LST is an excellent approximation of the true, transition-state barrier energy when bonding relationships do not change significantly [186].

For the inner-sphere and ligation calculations, the B3LYP/6-31+G(d,p) method and basis sets were used [10, 180]. For the outer-sphere calculations, B3LYP/6-31G(d) was used to obtain the minimum potential energy geometries, and B3LYP/6-31++G(d,p) for the Gibbs free energies. All calculations were performed using Gaussian 03 [107]. Optimizations and single point calculations were performed with an IEFPCM [323] implicit

solvent field, and a minimum of one explicit solvent shell of H_2O around the Fe atom. Additional solvent, another six H_2O molecules, was utilized when computationally practical.

The goethite clusters were initially created using experimentally-determined atomic positions for the crystal [241] cleaved along the (110) face. To mimic the rigidity of the crystal's surface, the positions of the Fe^{3+} atoms, and their surrounding O and H atoms were held fixed. The Fe^{2+} atom, the solvent H_2O, and the N atoms were allowed to relax. For the goethite clusters, due to the solvation and its role in the reaction chemistry, the LST failed to produce a reasonable barrier height. As such the 4-point method [324] was used to provide a reasonable estimate of the barrier height. This requires only the optimized geometries of both reactants and products which are then separated into donor and acceptor molecules. Single point calculations are performed at oxidized and reduced electronic states for all structures and the energies fit to quadratic Marcus theory paths according to the following formula:

$$Ea = ¼\ \lambda\ (1+\Delta G_r/\lambda)^2 \text{ where} \quad (4)$$

$$\lambda = E(Ox)_{red} - E(Ox)_{ox} + E(Red)_{ox} - E(Red)_{red} \quad (5)$$

the abbreviation in the parenthesis refers to the wave function, while subscript refers to geometry. This barrier is accurate except that it does not take into account the stabilization of the overlap between donor and acceptor states. Given the energies involved and the similarities between the heterogeneous and homogeneous cases this will be more than adequate.

Marcus Theory provides a robust connection between the reaction pathways and the overall rate constants for the reaction. In Marcus Theory, the reaction and product

states are treated as quadratic curves in reaction coordinate space. Near the crossing point, the two curves will mix, but near the minima they will behave as λx^2. λ represents the reorganization energy and has an intrinsic and solvent components. The intrinsic component is fundamental to the electronic state of the molecule, as the N_2 triple bond is transformed into a double bond radical. The solvent component is the energy required to move the H_2O molecules to stabilize the movement of an electron. The intrinsic component depends on the molecule involved in the reaction, and is transferable to similar reactions, which is why it is of particular interest. The combination of λ, with the half-cell potential indicates how much energy is needed to overcome the kinetic barrier to reduce N_2.

Solvent contributions to the barrier height were determined using the Marcus continuum solvent formula:

$$\lambda_E = (\Delta e)^2(1/2r_1 + 1/2r_2 - 1/r)(1/d_{op} - 1/d_{stat}) \quad (6)$$

where r_1 and r_2 are radii for the donor and acceptor cavities, r is the distance between their centers, d_{op} is the optical dielectric constant (1.77 for water), and d_{stat} is the static dielectric constant (78.39 for water). Values of r were taken from the optimized structures for the reactants. Cavity radii were determined by averaging the computed lengths of M-O bonds. We took the average of the λ_E values for both products and reactants evaluated at the adiabatic crossing point. These were added to the intrinsic value of the barrier determined from the LST in the homogeneous case and Nelson's method in the heterogeneous case.

No rate constants were produced as a result of this study. Any rate constant of the form: $k = Ae^{(-Ea/RT)}$, where the barrier (Ea) is above 150kJ/mol is, essentially, 0. A

photochemical reaction will depend entirely on the intensity of photons with energies above the barrier of the reaction.

A short discussion of the role of protons in electron transfer is important here, because H^+ transfer can determine the path that the reaction will take. PCET reactions are those where the motion of the proton is connected to the progress of the electron. There are two types of PCET reactions: concerted and sequential. A concerted PCET reaction is equivalent to a hydrogen atom transfer except that the electron and proton may come from different parts of the reactant. In a sequential reaction the proton is a result of pH changes, which result from oxidation changes, or vice versa. The approach of computing energies for both concerted and sequential pathways is called a Mayer Square [200].

Three paths are considered for the PCET. In the first path, the proton and the electron transfer at the same time. In the second path, the electron transfers first followed by the proton and in the final path the proton transfers first followed by the electron. This procedure requires two additional energy minimizations of the model system: one in product oxidation states, and the second in the reactants state. The transferring protons must be frozen with the minimum number of constraints during the optimization. Under ordinary circumstances, a total of five linear synchronous transits would be required. However, because N_2 is not a base, the proton-first electron-second optimization and path was neglected.

Finally, we conducted a simple calculation to examine the role of metal binding on ET to N_2. We optimized Li^+-N_2 and Li^+-$N_2^{-\bullet}$ in the gas phase at the B3LYP/6-31G+(d,p) level of theory. Using the Li-N_2 bond distances and angles we created clusters to examine the following reactions:

$$Li^{+}_{n}\text{-}N_{2(aq)} + e^{-} \rightarrow Li^{+}_{n}\text{-}N_{2}^{-\bullet}{}_{(aq)} \text{ where n=1 to 4} \quad (7)$$

These calculations were not optimized but rather single point calculations with IEFPCM continuum solvent were performed to determine reaction energetics.

Results

Inner-sphere pathways were tested first, because these mechanisms have been studied most extensively in the past. We followed that up by a study of outer-sphere mechanisms when the intermediates proved unreasonable.

Ligation mechanisms

A model $Fe^{2+}(H_2O)_6$ with a non-bonded N_2, and a $Fe^{2+}(H_2O)_5N_2$ with a non-bonded H_2O, were optimized (See Figure V-2). N_2 will bind to Fe with a ΔG_r=-0.6 kJ/mol or a K_{eq}=1. Although N_2 is as strong a ligand as H_2O, the equilibrium favors the H_2O molecule because the concentration of H_2O is much higher than N_2 in aqueous solutions (56 M vs. ~1 x 10^{-4} M). At sub-millimolar Fe concentrations, a fraction of the Fe will be ligated to the N_2. The question of double ligation was not studied directly, but predictions can be made. Mulliken charges for this complex indicate a neutral N_2, which suggests that it will bind to a second iron as well. However, at anything less than ocean/brine-level concentrations (~1 M) of Fe, the concentration of this Fe_2N_2 species would be insignificant.

Inner-sphere mechanisms

When performing the optimizations for the $Fe(II)(H_2O)_5N_2$ to $Fe(III)(H_2O)_4OHN_2H$ PCET, the reactant was an end-on complex. Both end-on and T starting points were attempted and produced the same result (See Figure V-3). We noted that the N_2H ligand had a pronounced bend, *i.e.* the N-N-H angle was significantly different from 180°, which indicated that the Fe was actually a charge-stabilized Fe(IV). We tested this by optimizing under different spin conditions, which confirmed the triplet state as the lowest energy, *i.e.* a [Ar]$3d^4$ electron configuration. The LST would have to have been performed in the S=5 state to avoid issues of spin forbidden transitions. This approach, of different spins for optimizations and energies, is necessary to overcome a limitation in the Gaussian code, which does not allow for the initial placement of electrons on specified atoms.

A problem emerged when additional solvent was placed around the N_2H ligand. This species in real solvent does not occupy an electronic minimum and cannot be expected to exhibit a finite lifespan. Nothing short of artificially fixing the N-H bond was going to keep the proton or the electron on the N_2 ligand. As such, any possibility of a singly-ligated inner-sphere pathway was rejected. It also raises the question as to what would happen to the models of adsorbed $N_2H^{\bullet}$ on the Nitrogenase cofactor if explicit solvent was included in the optimizations of the initial intermediates. As presented, the mechanism is a concerted single electron single proton transfer whose first intermediate is of the form R-Fe-N_2-H [308, 325]. It is not clear if the remainder of the cofactor could provide sufficient electronic stabilization if explicit water were included in their model.

<u>Outer-sphere mechanisms</u>

The disadvantage of outer-sphere pathways (see figure V-4) is that the Fe is unable to stabilize the unpaired electron on the N_2. It will, however, provide a comparison to competing reactions, such as the formation of hydrogen and the reduction of CO_2. Outer-sphere pathways provide information transferable to other more reducing species such as white rust: $Fe(OH)_{2(PPT)}$. Fe^{2+} to goethite was selected because the overall reaction to form ammonia from N_2 is thermodynamically favorable, and goethite is known to form environmentally from the oxidation of Fe^{2+}.

Homogeneous-$Fe^{2+}_{(aq)}$

This reaction shows a large barrier to the formation of N_2 radical species. The following reaction energies:

$$Fe^{2+}_{(aq)} + N_{2(aq)} \rightarrow N_2H^{\bullet}_{(aq)} + FeOH^{2+}_{(aq)} \qquad \Delta G=311.9kJ/mol,\ E_{a(gas)}=338.1kJ/mol \tag{8}$$

and

$$Fe^{2+}_{(aq)} + N_{2(aq)} \rightarrow N_2^{1-\bullet}{}_{(aq)} + Fe^{3+}_{(aq)} \qquad \Delta G=350.3kJ/mol \tag{9}$$

Lead to half-cell energies of:

$$e^- + H^+ + N_{2(aq)} \rightarrow N_2H^{\bullet}_{(aq)} \qquad \Delta G=286.7kJ/mol \tag{10}$$

and

$$e^- + N_{2(aq)} \rightarrow N_2^{1-\bullet}{}_{(aq)} \qquad \Delta G=276.1kJ/mol \tag{11}$$

$N_2H^{\bullet}_{(aq)}$ is the favored radical species over $N_2^{1-\bullet}{}_{(aq)}$because of the acidic nature of the ferric ions. Unlike the inner-sphere mechanism these species, although high in Gibbs free energy, are minima, meaning that they are at least metastable.

Looking at the reaction pathway, in Figure V-4, the strengths and weaknesses of hybrid DFT can be seen. Hybrid DFT is excellent for thermodynamics and energetics. However, when using LST to determine reaction pathways, the energies divert from the adiabatic, or quadratic, surface, which makes estimating the adiabatic reorganization energy difficult. Due to errors in extrapolation, any fit, whether only to the first one or two points or to the majority of the curve before the peak, shows great variability in the reorganization energy. Complicating this is the additional possibility that the reaction is actually taking place in the anomalous region where $\Delta G_r > \lambda$.

Heterogeneous-Goethite$\equiv Fe^{+2}_{(ads)}$

In the case of adsorbed Fe^{+2} on goethite, we see a slightly different picture. Figure V-5 shows the structured and hydrogen bonds for the reactants and products of the following reaction:

$$\equiv Fe^{2+}_{(ads)} + N_{2(aq)} \rightarrow N_2^{1-\bullet}{}_{(aq)} + \text{Goethite} \equiv H^{+} \qquad \Delta G = +262.9 \text{kJ/mol} \qquad (12)$$

While a significant improvement over the homogeneous case, much of the energy is lost by the absorption of ferrous iron on goethite, particularly at neutral pH. The Mayer Square was not necessary in this case. The proton preferred the goethite site, which indicated that this reaction is simply an electron transfer. Despite the calculated decrease in the Gibbs free energy of over 100 kJ/mol, it is still insufficient to produce a reaction with an appreciable concentration of products as a dark reaction. However, photchemically the range of light frequencies which will catalyze this reaction has been increased, $E_{a(gas)} = 268.1$kJ/mol.

One of the interesting, environmentally significant results of this study is an explanation of why the Fe^{+2}/goethite is often found in redox equilibrium in groundwater [326, 327]. The change in thermodynamics has a secondary, indirect change on the reduction kinetics for any Fe^{+2} system where goethite, or hematite or ferrihydrite, is present, but there is no primary change in the electronic structure or in reorganization energies (ET kinetics).

Subsequent Steps

With the initiation of a radical chain sequence, any proposed mechanism is incomplete. However, a disproportionation sequence is a logical extension of the reactions proposed above. A thorough, kinetic analysis of a possible sequence was not performed, because it would detract from the above work more than it would add. Still, it is possible to compute the thermodynamic energies of the intermediates: diimide, hydrazine, and ammonia using the following calculation:

$$N_2 \bullet 4H_2O_{(aq)} + nH_{2(g)} \rightarrow N_2H_{n(aq)} + 4H_2O_{(aq)} \quad \Delta G_f = 220.9\text{kJ/mol}(N_2H^{\bullet}) \quad (13)$$

$$145.4\text{kJ/mol}(N_2H_{2cis})$$

$$130.0\ \text{kJ/mol}(N_2H_{2trans})$$

$$9.3\ \text{kJ/mol}(N_2H_4)$$

$$-93.9\text{kJ/mol}(NH_3)$$

assuming a value of 4.32kJ/mol for $N_{2(aq)}$. The (aq) subscript designates the use of IEFPCM in the calculation. For optimized cluster structures see Figure V-6. The experimental value for aqueous ammonia is -79.4kJ/mol, indicating an error of 14.5kJ/mol, which is reasonable agreement for our purposes. However, the value

presented here for $N_2H^{\bullet}$ should be considered less reliable than the one determined by the homogeneous outer-sphere reaction, as the energies of the reactants and products were determined in separate calculations rather than as a reaction.

Li Binding

Experiments and our calculations agree that the barrier to dinitrogen reduction is the diN_2 radicals. So we turn to consideration of how to stabilize that barrier. The choice of Li as a ligating agent serves multiple purposes; it will verify the results seen in the Shilov experiments [272], as well as show the effects a metal like sodium will have in sea water. As it's a poor binder and a non-reducing agent, we can approximate the chemistry of transition metals generally without including specific benefits of individual metals resulting from binding. As a result we deliberately underestimate the effect that individual species may have. The optimizations of the Li^+-N_2 and Li^+-$N_2^{-\bullet}$ show end-on binding with Li-N distances of 2.07Å and 1.96Å respectively. They failed to optimize in the dielectric field, so these results can not be considered quantitative environmental results, but only indicators of the effects of ligation in general. Figure V-7 shows the energies of the following reactions:

$$Li^+_n\text{-}N_{2(aq)} + e^- \rightarrow Li^+_n\text{-}N_2^{-\bullet}{}_{(aq)} \text{ where n=1 to 4.} \qquad (14)$$

The first two Li were placed end on as that was the preferred ligation direction. To confirm that the results were not simply electrostatic the Li was rotated from 180 ^{o} to 120^o, obtuse, to 72.5^o, side on binding. The effect of ligating to the side of the N_2 was double the stabilization of the end on and obtuse orientations, despite the fact that the N-Li distance was the same. This demonstrates the reason why metals like Mo, which side

bind, are so effective. Each of the side binding Li reduce ≳100kJ/mol from the energy of this intermediate, resulting from interactions between the metal's d and f orbitals with the N_2 π^* orbital. This energy is independent of the overall thermodynamic driving force for the reaction, and is incorporated to all three classes of the biological mechanisms.

By this analysis, it turns out that Green Rust, generally an excellent reductant, is a poor choice for N_2. All of the irons are bound octahedrally to six OH groups each of which are simultaneously ligated to three iron centers, making for a high barrier for inner-sphere adsorption.

Conclusion

Dinitrogen reduction, while one of the most complicated redox problems, has a simple answer, adsorption to multiple reducing transition metal centers. All three biological models rely on multiple transition metals centers either to bind the N_2 directly, or, for the reduction of hydrogen, an essential component for many models. The key is an environmental system is not out-competed by H_2 production.

A second consequence of this work is that the thermodynamic driving force for ET, while not sufficient for N_2 reduction, is sufficient to explain why the introduction of a ferric iron oxide is sufficient to promote redox equilibrium in many environmental systems. The difference between aqueous ferrous iron oxidation and adsorbed oxidation, after consideration of adsorption, is still ~100kJ/mol, more than adequate to overcome most redox barriers.

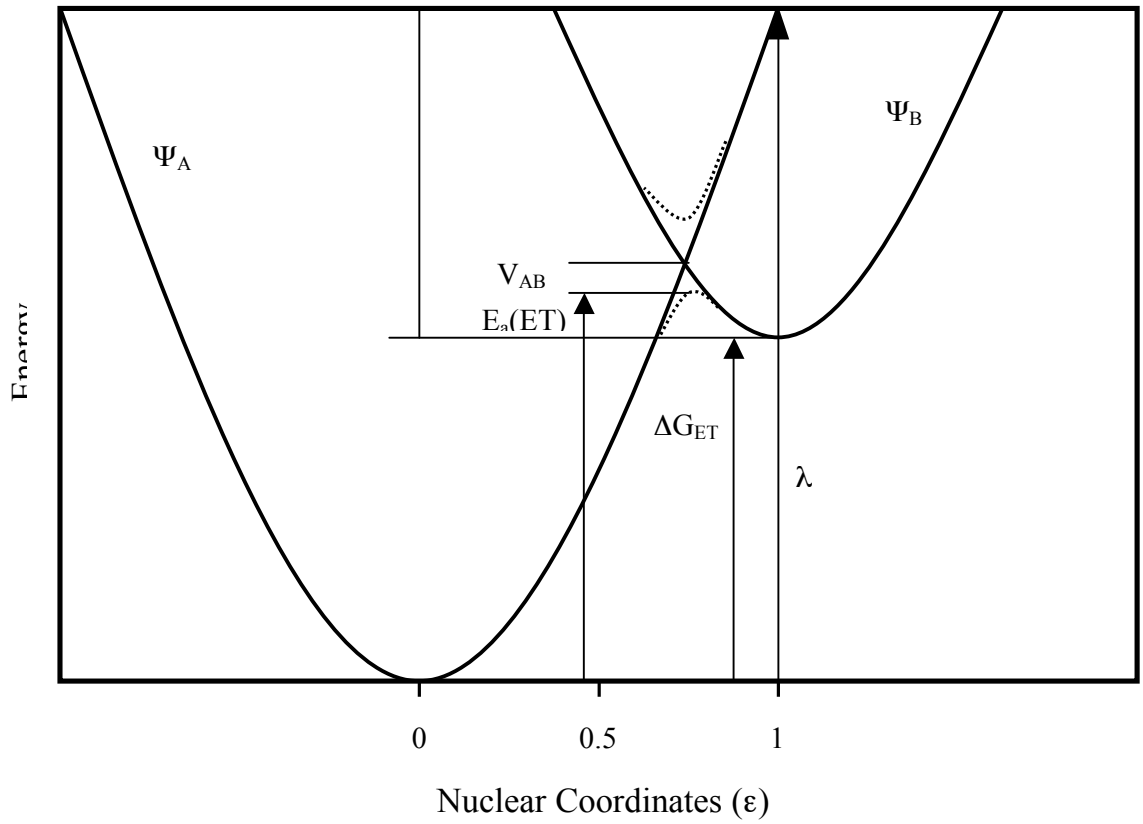

Figure V-1: Marcus reaction diagram illustrating the fundamental components of an electron transfer rate. The hypothetical system shown here illustrates the challenges associated with electron transfer to reduce dinitrogen.

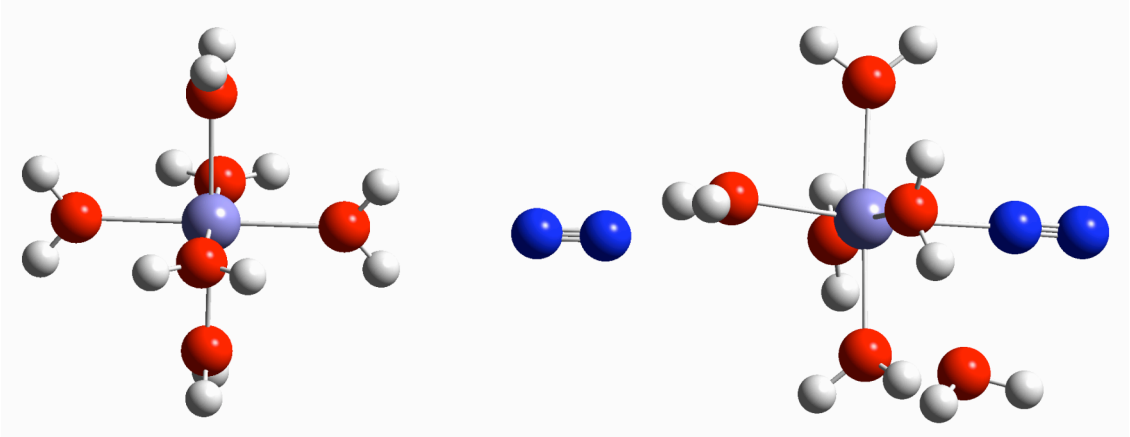

Figure V-2: Structures for the ligation of N_2. The structure on the left is the optimized $Fe^{2+}(aq)$ and the right is the $FeN_2^{2+}(aq)$ optimized structure.

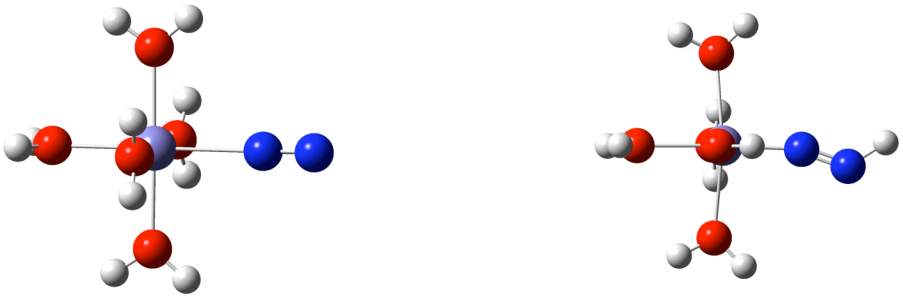

Figure V-3: Reactants and products for the inner-sphere gas phase reaction. The structure on the right is the one that disintegrates with explicit solvent resulting in essentially the same geometry as the one on the left.

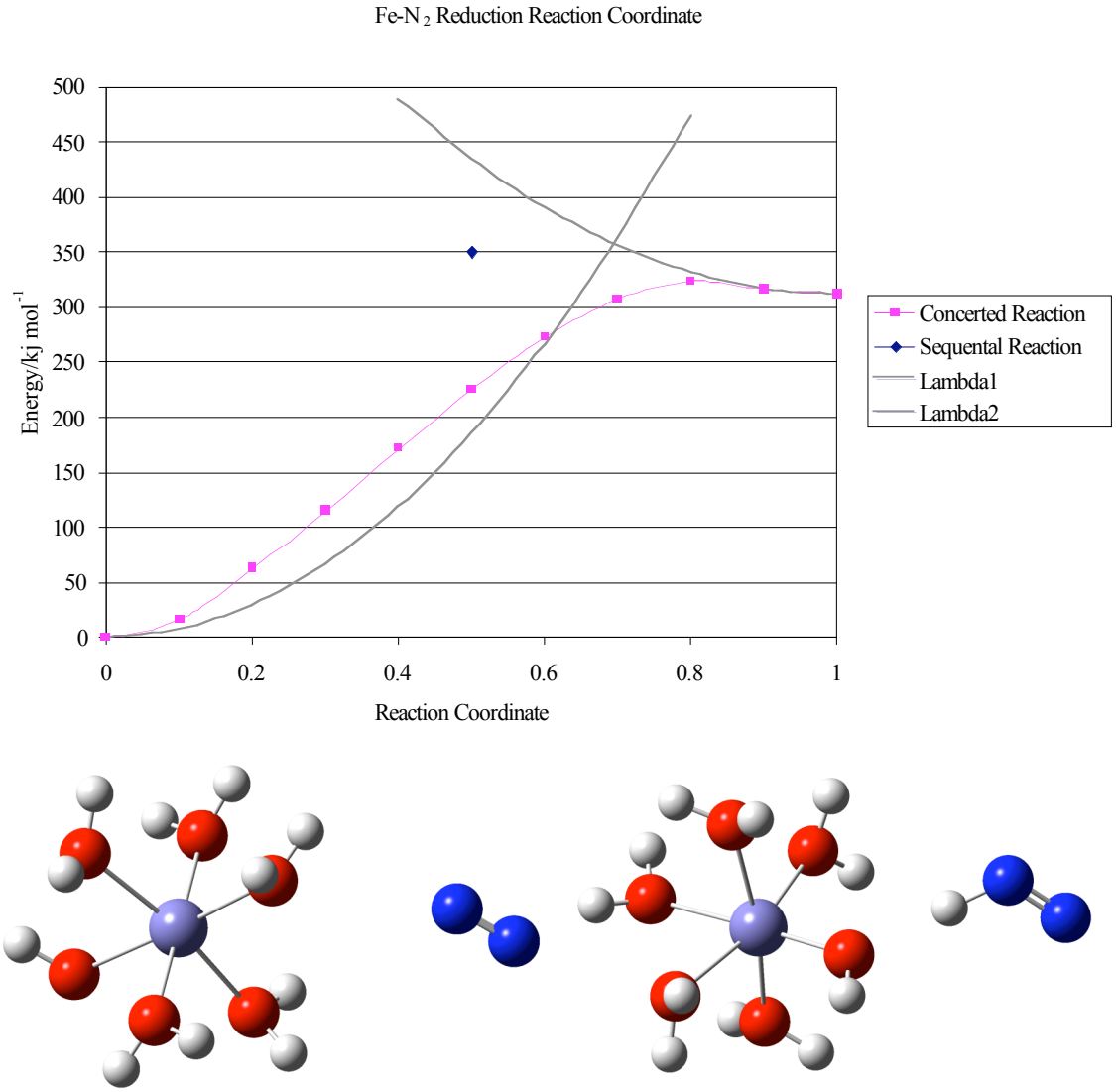

Figure V-5: Homogeneous outer sphere reaction pathway energies with structures. The point designated sequential reaction indicates what would happen on the reaction path if the electron transferred first formed N_2^-. Structures on left are the reactants structures on right is the products.

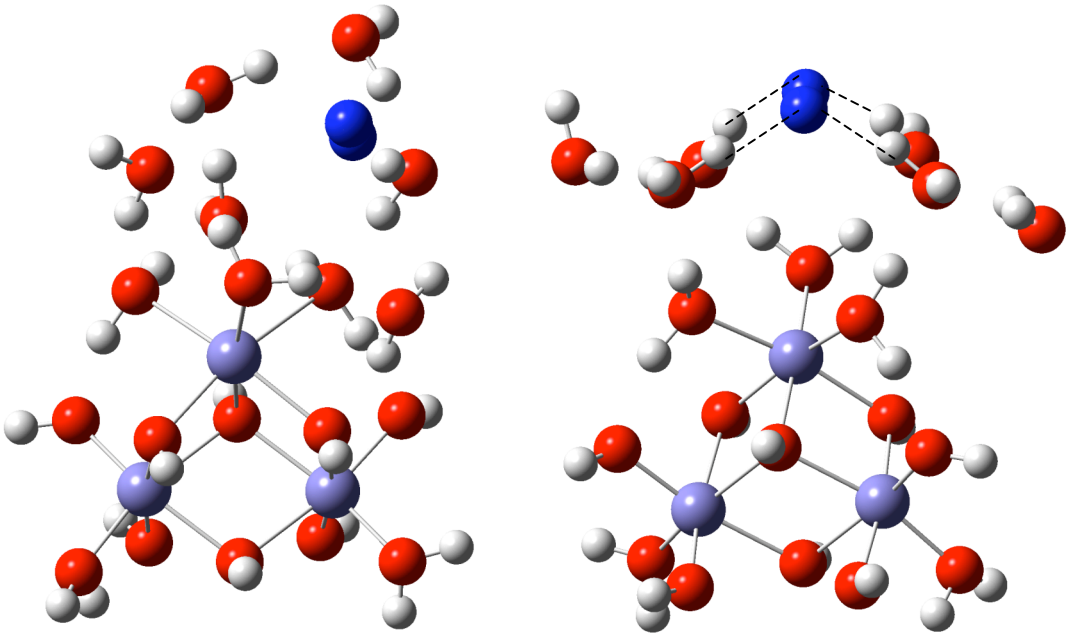

Figure V-5: Clusters were used to represent absorbed Fe^{+2} sites on goethite. Total charges for all clusters were zero. Note the four hydrogen bonds shown as dotted lines to the nitrogen in the second cluster.

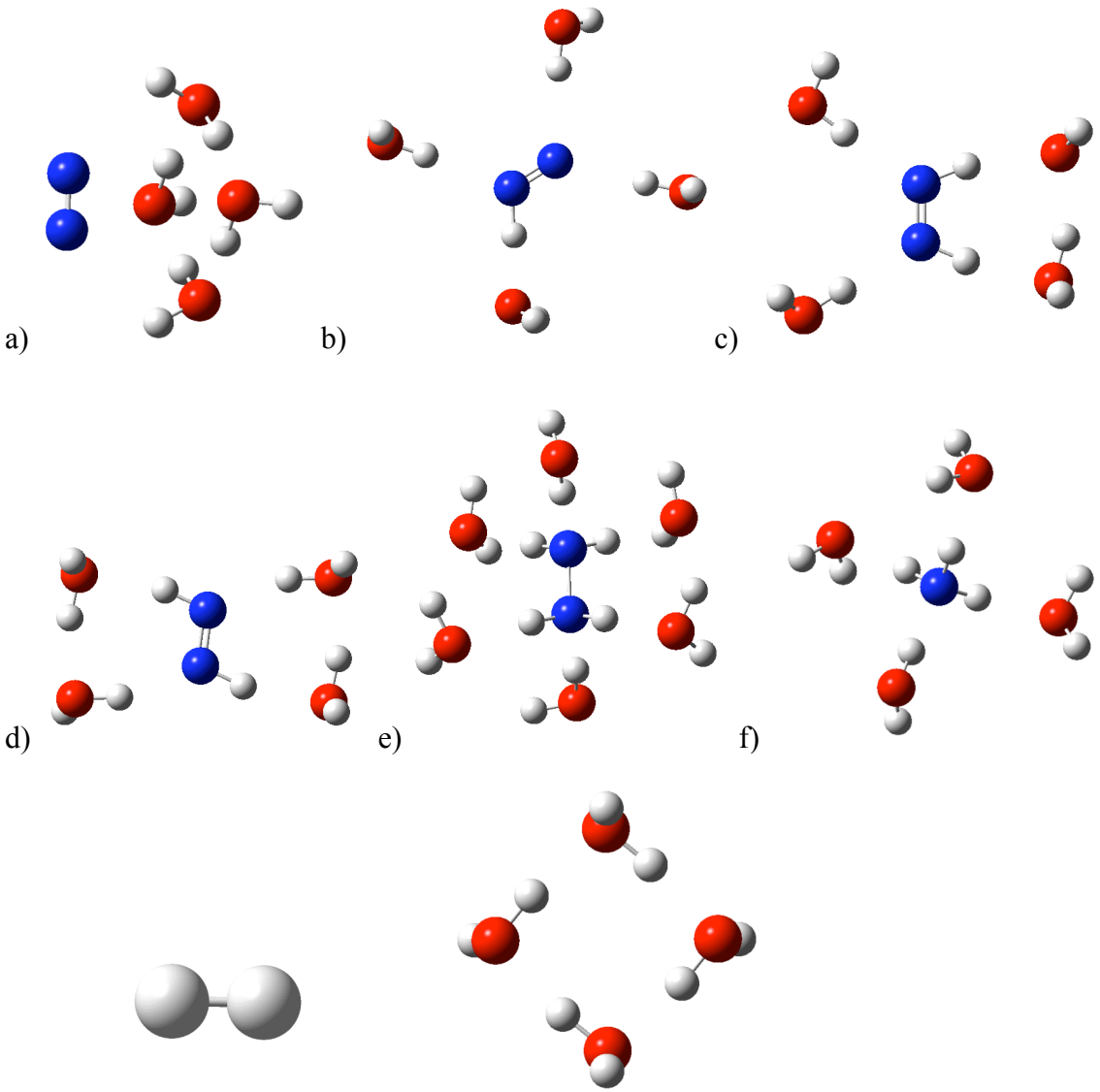

Figure V-6: Structures used for disproportionation: a) $N_{2(aq)}$ b) $N_2H\bullet_{(aq)}$ c) N_2H_{2cis} d) N_2H_{2trans} e) N_2H_4 f) NH_3 g) $H_{2(g)}$ and h) H_2O. H_2 was not computed as an aqueous cluster as the aprroach was to keep the number of water molecules as close to the same as possible between cluster, as the water represents the largest source of error in the calculation.

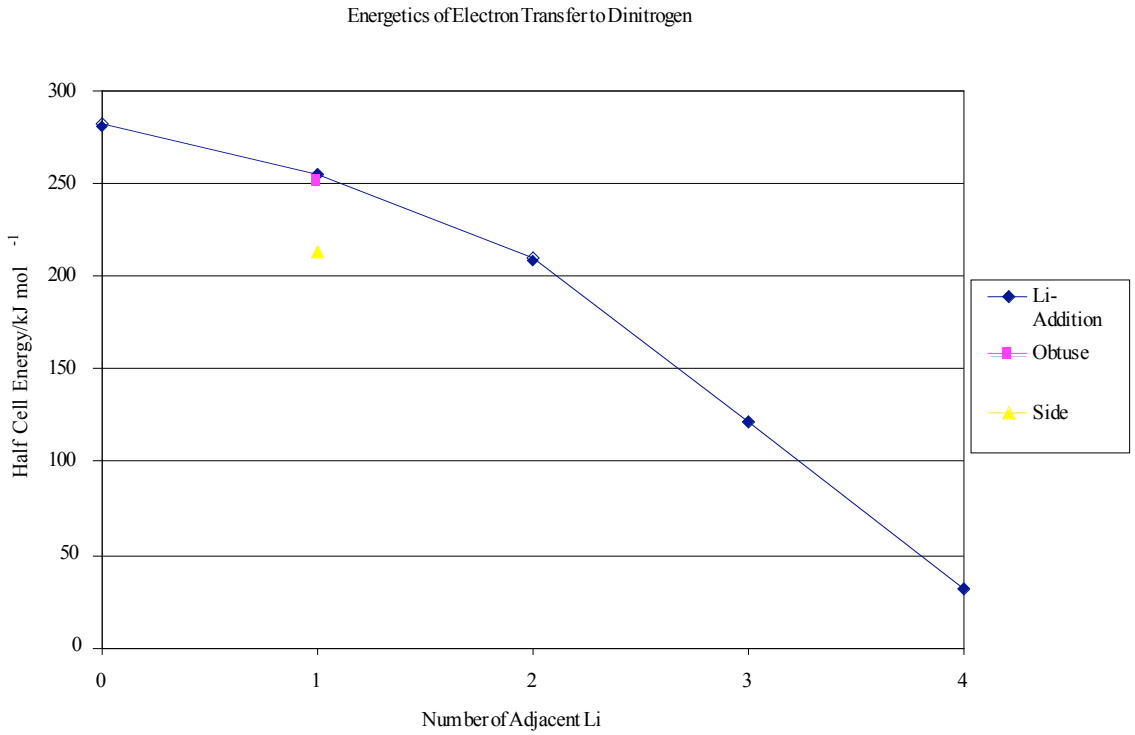

Figure V-7: Arrangement of Li ions around N_2 and half cell reaction energetics for the addition of an electron. Differences between N_2 and $N_2^{-\bullet}$ structures are in the N-N and Li-N bond lengths.

Bibiography

1. Tsuchiya, T.; Tsuchiya, J.; Wentzcovitch, R. M., MgSiO3 post-perovskite at D " conditions. *Geochimica Et Cosmochimica Acta* **2005,** 69, (10), A508-A508.
2. Umemoto, K.; Wentzcovitch, R. M., Theoretical study of the isostructural transformation in ice VIII. *Physical Review B* **2005,** 71, (1).
3. Kiefer, B.; Stixrude, L.; Hafner, J.; Kresse, G., Structure and elasticity of wadsleyite at high pressures. *American Mineralogist* **2001,** 86, (11-12), 1387-1395.
4. Karki, B. B.; Stixrude, L.; Wentzcovitch, R. M., High-pressure elastic properties of major materials of Earth's mantle from first principles. *Reviews of Geophysics* **2001,** 39, (4), 507-534.
5. Kiefer, B.; Stixrude, L.; Wentzcovitch, R. M., Calculated elastic constants and anisotropy of Mg2SiO4 spinel at high pressure. *Geophysical Research Letters* **1997,** 24, (22), 2841-2844.
6. Cramer, C. J., *Essentials of Computational Chemistry Theoreis and Models*. John Wiley & Sons: Chichester, West Sussex, England, 2002; p 542.
7. Becke, A. D., A multicenter numerical integration scheme for polyatomic molecules. *Journal of Chemical Physics* **1988,** 88, (4), 2547-2554.
8. Perdew, J. P.; Wang, Y., Accurate and simple analytic representation of the electron-gas correltation energy. *Physical Review B* **1992,** 45, (23), 13244-13249.
9. Lee, C.; Yang, W.; Parr, R. G., development of the Colle-Salvetti correltaiton-energy formula into a functiona of the electron density. *Physical Review B* **1988,** 37, (2), 785-789.
10. Becke, A. D., Density-Functional Thermochemistry. III. The Role of Exact Exchange. *Journal of Chemical Physics* **1993,** 98, 5648-5652.
11. Stevens, P. J.; Devlin, F. J.; Chabalowski, C. F.; Frisch, M. J., Ab-Initio Calculation of VIbrational Absorption and Circular-Dichroism Spectra using Density Functional Force-Fields. *Journal of Physical Chemistry* **1994,** 98, (45), 11623-11627.
12. Becker, U.; Rosso, K. M., Step edges on galena (100): Probing the basis for defect driven surface reactivity at the atomic scale. *American Mineralogist* **2001,** 86, (7-8), 862-870.
13. Gibbs, G. V.; Boisen, M. B.; Beverly, L. L.; Rosso, K. M., A computational quantum chemical study of the bonded interactions in earth materials and structurally and chemically related molecules. In *Molecular Modeling Theory: Applications in the Geosciences*, 2001; Vol. 42, pp 345-381.
14. Rosso, K. M.; Becker, U.; Hochella, M. F., Atomically resolved electronic structure of pyrite {100} surfaces: An experimentatl and theoretical investigation with implications for reactivity. *American Mineralogist* **1999,** 84, 1535-1548.
15. Rosso, K. M.; Becker, U.; Hochella, M. F. J., The interaction of pyrite {100} surfaces with O2 and H2O: Fundamental oxidation mechanisms. *American Mineralogist* **1999,** 84, 1549-1561.
16. Rosso, K. M.; Dupuis, M., Reorganization energy associated with small polaron mobility of iron oxide. *Journal of Chemical Physics* **2004,** 120, (15), 7050-7054.
17. Rosso, K. M.; Smith, D. M. A.; Dupuis, M., Aspects of Aqueous Iron and Manganese (II/III) Self Exchange Electron Transfer Reactions. *The Journal of Physical Chemistry A* **2004,** 108, (24), 5242-5248.

18. Kamolpornwijit, W.; Liang, L. Y.; Moline, G. R.; Hart, T.; West, O. R., Identification and quantification of mineral precipitation in Fe-0 filings from a column study. *Environmental Science & Technology* **2004,** 38, (21), 5757-5765.
19. Legrand, L.; El Figuigui, A.; Mercier, F.; Chausse, A., Reduction of aqueous chromate by Fe(11)/Fe(111) carbonate green rust: Kinetic and mechanistic studies. *Environmental Science & Technology* **2004,** 38, (17), 4587-4595.
20. Phillips, D. H.; Watson, D. B.; Roh, Y.; Gu, B., Mineralogical characteristics and transformations during long-term operation of a zerovalent iron reactive barrier. *Journal of Environmental Quality* **2003,** 32, (6), 2033-2045.
21. Genin, J. M. R.; Refait, P.; Olowe, A. A.; Abdelmoula, M.; Fall, I.; Drissi, S. H., Identification of Green Rust compounds in the aqueous corrosion processes of steels; the case of Microbially induced corrosion and use of 78 K CEMS. *Hyperfine Interactions* **1998,** 112, (1-4), 47-50.
22. Genin, J. M. R.; Refait, P. H.; Abdelmoula, M., Green rusts and their relationship to iron corrosion; a key role in microbially influenced corrosion. *Hyperfine Interactions* **2002,** 139, (1-4), 119-131.
23. Abdelmoula, M.; Refait, P.; Drissi, S. H.; Mihe, J. P.; Genin, J. M. R., Conversion electron Mossbauer spectroscopy and X-ray diffraction studies of the formation of carbonate-containing green rust one by corrosion metallic iron in NaHCO3 and (NaHCO3+NaC1) solutions. *Corrosion Science* **1996,** 38, (4), 623-633.
24. Furukawa, Y.; Kim, J. W.; Watkins, J.; Wilkin, R. T., Formation of ferrihydrite and associated iron corrosion products in permeable reactive barriers of zero-valent iron. *Environmental Science & Technology* **2002,** 36, (24), 5469-5475.
25. Music, S.; Nowik, I.; Ristic, M.; Orehovec, Z.; Popovic, S., The effect of bicarbonate/carbonate ions on the formation of iron rust. *Croatica Chemica Acta* **2004,** 77, (1-2), 141-151.
26. Refait, P.; Abdelmoula, M.; Genin, J. M. R.; Sabot, R., Green rusts in electrochemical and microbially influenced corrosion of steel. *Comptes Rendus Geoscience* **2006,** 338, (6-7), 476-487.
27. Bourrie, G.; Trolard, F.; Genin, J. M. R.; Jaffrezic, A.; Maitre, V.; Abdelmoula, M., Iron control by equilibria between hydroxy-Green Rusts and solutions in hydromorphic soils. *Geochimica Et Cosmochimica Acta* **1999,** 63, (19-20), 3417-3427.
28. Ruby, C.; Gehin, A.; Aissa, R.; Genin, J. M. R., Mass-balance and E-h-pH diagrams of FeII-III green rust in aqueous sulphated solution. *Corrosion Science* **2006,** 48, (11), 3824-3837.
29. Abdelmoula, M.; Trolard, F.; Bourrie, G.; Genin, J. M. R., Evidence for the Fe(II)-Fe(III) Green Rust "Fougerite" mineral occurrence in a hydromorphic soil and its transformation with depth. *Hyperfine Interactions* **1998,** 112, (1-4), 235-238.
30. Genin, J. M. R.; Refait, P.; Simon, L.; Drissi, S. H., Preparation and E-h-pH diagrams of Fe(II)-Fe(III) green rust compounds; hyperfine interaction characteristics and stoichiometry of hydroxy-chloride, -sulphate and -carbonate. *Hyperfine Interactions* **1998,** 111, (1-4), 313-318.
31. Refait, P.; Genin, J. M. R., The mechanisms of oxidation of ferrous hydroxychloride beta-Fe-2(OH)(3)Cl in aqueous solution: The formation of akaganeite vs goethite. *Corrosion Science* **1997,** 39, (3), 539-553.

32. Ruby, C.; Aissa, R.; Gehin, A.; Cortot, J.; Abdelmoula, M.; Genin, J. M., Green rusts synthesis by coprecipitation of Fe-II-Fe-III ions and mass-balance diagram. *Comptes Rendus Geoscience* **2006,** 338, (6-7), 420-432.
33. Genin, J. M. R.; Olowe, A. A.; Refait, P.; Simon, L., On the stoichiometry and Pourbaix diagram of Fe(II)-Fe(III) hydroxy-sulphate or sulphate-containing green rust .2. An electrochemical and Mossbauer spectroscopy study. *Corrosion Science* **1996,** 38, (10), 1751-1762.
34. Trolard, F.; Bourrie, G., Structure of fougerite and green rusts and a thermodynamic model for their stabilities. *Journal of Geochemical Exploration* **2006,** 88, (1-3), 249-251.
35. Hansen, H. C. B.; Guldberg, S.; Erbs, M.; Koch, C. B., Kinetics of nitrate reduction by green rusts - effects of interlayer anion and Fe(II): Fe(III) ratio. *Applied Clay Science* **2001,** 18, (1-2), 81-91.
36. O'Loughlin, E. J.; Kelly, S. D.; Cook, R. E.; Csencsits, R.; Kemner, K. M., Reduction of Uranium(VI) by mixed iron(II/iron(III) hydroxide (green rust): Formation of UO2 manoparticies. *Environmental Science & Technology* **2003,** 37, (4), 721-727.
37. O'Loughlin, E. J.; Kelly, S. D.; Kemner, K. M.; Csencsits, R.; Cook, R. E., Reduction of Ag-I, Au-III, Cu-II, and Hg-II by Fe-II/Fe-III hydroxysulfate green rust. *Chemosphere* **2003,** 53, (5), 437-446.
38. O'Loughlin, E. J.; Kemner, K. M.; Burris, D. R., Effects of Ag-I, Au-III, and Cu-II on the reductive dechlorination of carbon tetrachloride by green rust. *Environmental Science & Technology* **2003,** 37, (13), 2905-2912.
39. O'Laughlin, E. J.; Kemner, K. M.; Burris, D. R., Effects of Ag^{I}, Au^{III}, Cu^{II} on the reductive dechlorination of Carbon tetrachloride by green rust. *Environmental Science & Technology* **2003,** 37, (2905-2912).
40. O'Loughlin, E. J.; Burris, D. R., Reduction of halogenated ethanes by green rust. *Environmental Toxicology and Chemistry* **2004,** 23, (1), 41-48.
41. Pepper, S. E.; Bunker, D. J.; Bryan, N. D.; Livens, F. R.; Charnock, J. M.; Pattrick, R. A. D.; Collison, D., Treatment of radioactive wastes: An X-ray absorption spectroscopy study of the reaction of technetium with green rust. *Journal of Colloid and Interface Science* **2003,** 268, (2), 408-412.
42. Lien, H. L.; Wilkin, R. T., High-level arsenite removal from groundwater by zero-valent iron. *Chemosphere* **2005,** 59, (3), 377-386.
43. Refait, P.; Simon, L.; Genin, J. M. R., Reduction of SeO_4^{2-} anions and anoxic formation of iron(II)- iron(III) hydroxy selenate green rust. *Environmental Science & Technology* **2000,** 34, (5), 819-825.
44. Su, C. M.; Puls, R. W., Significance of iron(II,III) hydroxycarbonate green rust in arsenic remediation using zerovalent him in laboratory column tests. *Environmental Science & Technology* **2004,** 38, (19), 5224-5231.
45. Su, C. M.; Wilkin, R. T., Arsenate and arsenite sorption on and arsenite oxidation by iron(II, III) hydroxycarbonate green rust. In *Advances in Arsenic Research*, 2005; Vol. 915, pp 25-40.
46. Refait, P.; Drissi, S. H.; Pytkiewicz, J.; Genin, J. M. R., The anionic species competition in iron aqueous corrosion: Role of various green rust compounds. *Corrosion Science* **1997,** 39, (9), 1699-1710.

47. Refait, P.; Memet, J. B.; Bon, C.; Sabot, R.; Genin, J. M. R., Formation of the Fe(II)-Fe(III) hydroxysulphate green rust during marine corrosion of steel. *Corrosion Science* **2003,** 45, (4), 833-845.
48. Genin, J. M. R.; Refait, P.; Bourrie, G.; Abdelmoula, M.; Trolard, F., Structure and stability of the Fe(II)-Fe(III) green rust "fougerite" mineral and its potential for reducing pollutants in soil solutions. *Applied Geochemistry* **2001,** 16, (5), 559-570.
49. Genin, J. M. R.; Abdelmoula, M.; Ruby, C.; Upadhyay, C., Speciation of iron; characterisation and structure of green rusts and FeII-III oxyhydroxycarbonate fougerite. *Comptes Rendus Geoscience* **2006,** 338, (6-7), 402-419.
50. Genin, J.-M. R.; Abdelmoula, M.; Aıssa, R.; Ruby, C., Ordering in FeII–III Hydroxysalt green rusts from XRD and Mo¨ ssbauer analysis (chloride, carbonate, sulphate, oxalate...); about the structure of hydrotalcite-like compounds. *Hyperfine Interact* **2005,** 166, 391-396.
51. Genin, J. M. R.; Aissa, R.; Gehin, A.; Abdelmoula, M.; Benali, O.; Ernstsen, V.; Ona-Nguema, G.; Upadhyay, C.; Ruby, C., Fougerite and FeII-III hydroxycarbonate green rust; ordering drprotonation and/or cation substitution; structure of hydrotalcite-like compounds and mythic ferrosic hydroxide Fe(OH)((2+x)). *Solid State Sciences* **2005,** 7, (5), 545-572.
52. Refait, P.; Charton, A.; Genin, J. M. R., Identification, composition, thermodynamic and structural properties of a pyroaurite-like iron(II)-iron(III) hydroxy-oxalate Green Rust. *European Journal of Solid State and Inorganic Chemistry* **1998,** 35, (10-11), 655-666.
53. Ruby, C.; Gehin, A.; Aissa, R.; Ghanbaja, J.; Abdelmoula, M.; Genin, J. M. R., Chemical stability of hydroxysulphate green rust synthetised in the presence of foreign anions: carbonate, phosphate and silicate. *Hyperfine Interactions* **2006,** 167, (1-3), 803-807.
54. Simon, L.; Francois, M.; Refait, P.; Renaudin, G.; Lelaurain, M.; Genin, J. M. R., Structure of the Fe(II-III) layered double hydroxysulphate green rust two from Rietveld analysis. *Solid State Sciences* **2003,** 5, (2), 327-334.
55. Parise, J. B.; Marshall, W. G.; Smith, R. I.; Lutz, H. D.; Moller, H., The nuclear and magnetic structure of "white rust" - Fe(OH0.86D0.14)(2). *American Mineralogist* **2000,** 85, (1), 189-193.
56. Genin, J. M. R.; Ruby, C.; Upadhyay, C., Structure and thermodynamics of ferrous, stoichiometric and ferric oxyhydroxycarbonate green rusts; redox flexibility and fougerite mineral. *Solid State Sciences* **2006,** 8, (11), 1330-1343.
57. Ruby, C.; Upadhyay, C.; Gehin, A.; Ona-Nguema, G.; Genin, J. M. R., In situ redox flexibility of FeII-III oxyhydroxycarbonate green rust and fougerite. *Environmental Science & Technology* **2006,** 40, (15), 4696-4702.
58. Genin, J. M. R.; Ruby, C., Anion and cation distributions in Fe(II-III) hydroxysalt green rusts from XRD and Mossbauer analysis (carbonate, chloride, sulphate,...); the "fougerite" mineral. *Solid State Sciences* **2004,** 6, (7), 705-718.
59. Refait, P. H.; Abdelmoula, M.; Genin, J. M. R., Mechanisms of formation and structure of green rust one in aqueous corrosion of iron in the presence of chloride ions. *Corrosion Science* **1998,** 40, (9), 1547-1560.

60. Rosso, K. M.; Smith, D. M. A.; Dupuis, M., An ab initio model of electron transport in hematite (.alpha.-Fe2O3) basal planes. *Journal of Chemical Physics* **2003,** 118, (14), 6455-6466.
61. Rosso, K. M.; Ilton, E. S., Charge transport in micas: The kinetics of FeII/III electron transfer in the octahedral sheet. *Journal of Chemical Physics* **2003,** 119, (17), 9207-9218.
62. Kerisit, S.; Rosso, K. M., Computer simulation of electron transfer at hematite surfaces *Geochimica et Cosmochimica Acta* **2006,** 70, (8), 1888-1903
63. Iordanova, N.; Dupuis, M.; Rosso, K. M., Charge transport in metal oxides: A theoretical study of hematite alpha-Fe2O3. *Journal of Chemical Physics* **2005,** 122, (14).
64. Kerisit, S.; Rosso, K. M., Charge transfer in FeO: A combined molecular-dynamics and ab initio study. *Journal of Chemical Physics* **2005,** 123, (22).
65. Xu, Y.; Schoonen, M. A. A., The absolute energy position of conduction and valence bands of selected semiconducting minerals. *American Mineralogist* **2000,** 85, 543-556.
66. Rosso, K. M., Structure and reactivity of semiconducting mineral surfaces: Convergence of molecular modeling and experiment. In *Molecular Modeling Theory: Applications in the Geosciences*, 2001; Vol. 42, pp 199-271.
67. Rosso, K. M.; Becker, U., Proximity effects on semiconducting mineral surfaces II: Distance dependence of indirect interactions. *Geochimica et Cosmochimica Acta* **2003,** 67, (5), 941-953.
68. Rosso, K. M.; Rustad, J. R.; Gibbs, G. V., Trivalent ion hydrolysis reactions II: Analysis of electron density distributions in metal-oxygen bonds. *J. Phys. Chem. A* **2002,** 106, (35), 8133-8138.
69. Williams, A. G. B.; Scherer, M. M., Spectroscopic evidence for Fe(II)-Fe(III) electron transfer at the iron oxide-water interface. *Environmental Science & Technology* **2004,** 38, (18), 4782-4790.
70. Silvester, E.; Charlet, L.; Tournassat, C.; Gehin, A.; Greneche, J. M.; Liger, E., Redox potential measurements and Mossbauer spectrometry of Fe-II adsorbed onto Fe-III (oxyhydr)oxides. *Geochimica Et Cosmochimica Acta* **2005,** 69, (20), 4801-4815.
71. Pedersen, H. D.; Postma, D.; Jakobsen, R., Release of arsenic associated with the reduction and transformation of iron oxides. *Geochimica Et Cosmochimica Acta* **2006,** 70, (16), 4116-4129.
72. Gorby, Y. A.; Yanina, S.; McLean, J. S.; Rosso, K. M.; Moyles, D.; Dohnalkova, A.; Beveridge, T. J.; Chang, I. S.; Kim, B. H.; Kim, K. S.; Culley, D. E.; Reed, S. B.; Romine, M. F.; Saffarini, D. A.; Hill, E. A.; Shi, L.; Elias, D. A.; Kennedy, D. W.; Pinchuk, G.; Watanabe, K.; Ishii, S.; Logan, B.; Nealson, K. H.; Fredrickson, J. K., Electrically conductive bacterial nanowires produced by Shewanella oneidensis strain MR-1 and other microorganisms. *Proceedings of the National Academy of Sciences of the United States of America* **2006,** 103, (30), 11358-11363.
73. Rosso, K. M.; Ilton, E. S., Effects of compositional defects on small polaron hopping in micas. *Journal of Chemical Physics* **2005,** 122, (24).
74. Neal, A. L.; Bank, T. L.; Hochella, M. F.; Rosso, K. M., Cell adhesion of Shewanella oneidensis to iron oxide minerals: Effect of different single crystal faces. *Geochemical Transactions* **2005,** 6, (4), 77-84.

75. Neal, A. L.; Rosso, K. M.; Geesey, G. G.; Gorby, Y. A.; Little, B. J., Surface structure effects on direct reduction of iron oxides by Shewanella oneidensis. *Geochimica Et Cosmochimica Acta* **2003,** 67, (23), 4489-4503.
76. Genin, J. M. R., Fe(II-III) hydroxysalt green rusts; from corrosion to mineralogy and abiotic to biotic reactions by Mossbauer spectroscopy. *Hyperfine Interactions* **2004,** 156, (1), 471-485.
77. Aissa, R.; Ruby, C.; Gehin, A.; Abdelmoula, M.; Genin, J. M. R., Synthesis by coprecipitation of al-substituted hydroxysulphate green rust (Fe4Fe(2-y)AlyIII)-Fe-II-Al-III(OH)(12)SO4, nH(2)O. *Hyperfine Interactions* **2004,** 156, (1), 445-451.
78. Gehin, A.; Ruby, C.; Abdelmoula, M.; Benali, O.; Ghanbaja, J.; Refait, P.; Genin, J. M. R., Synthesis of Fe(II-III) hydroxysulphate green rust by coprecipitation. *Solid State Sciences* **2002,** 4, 61-66.
79. Feder, F.; Trolard, F.; Klingelhofer, G.; Bourrie, G., In situ Mossbauer spectroscopy: Evidence for green rust (fougerite) in a gleysol and its mineralogical transformations with time and depth. *Geochimica Et Cosmochimica Acta* **2005,** 69, (18), 4463-4483.
80. Ruby, C.; Gehin, A.; Abdelmoula, M.; Genin, J. M. R.; Jolivet, J. P., Coprecipitation of Fe(II) and Fe(III) cations in sulphated aqueous medium and formation of hydroxysulphate green rust. *Solid State Sciences* **2003,** 5, (7), 1055-1062.
81. Trolard, F.; Genin, J. M. R.; Abdelmoula, M.; Bourrie, G.; Humbert, B.; Herbillon, A., Identification of a green rust mineral in a reductomorphic soil by Mossbauer and Raman spectroscopies. *Geochimica Et Cosmochimica Acta* **1997,** 61, (5), 1107-1111.
82. Kukkadapu, R. K.; Zachara, J. M.; Fredrickson, J. K.; Kennedy, D. W., Biotransformation of two-line silica-ferrihydrite by a dissimilatory Fe(III)-reducing bacterium: Formation of carbonate green rust in the presence of phosphate. *Geochimica Et Cosmochimica Acta* **2004,** 68, (13), 2799-2814.
83. Hawthorne, F. C., Mossbauer-Spectroscopy. *Reviews in Mineralogy* **1988,** 18, 255-340.
84. Marcus, R. A., *Journal of Physical Chemstry* **1956,** 24, 966.
85. Marcus, R. A., Chemical and Electrochemical Electron-Transfer Theory. *Annual Reviews* **1964**, 155-196.
86. Newton, M. D.; Sutin, N., Electron Transfer Reactions in Condensed Phases. *Annual Reviews in Physical Chemistry* **1984,** 35, 437-480.
87. Newton, M. D., Role of Ab-Initio Calculations in Elucidating Properties of Hydrated and Ammoniated Electrons. *Journal of Physical Chemistry* **1975,** 79, (26), 2795-2808.
88. Holstein, T., Studies of Polaron Motion .2. the Small Polaron. *Annals of Physics* **1959,** 8, (3), 343-389.
89. Iordanova, N.; Dupuis, M.; Rosso, K. M., Theoretical characterization of charge transport in chromia (alpha-Cr2O3). *Journal of Chemical Physics* **2005,** 123, (7).
90. Saunders, V. P.; Dovesi, R.; Roetti, C., *CRYSTAL03, University of Torino, Torino* **2003**.
91. Catti, M.; Valerio, G.; Dovesi, R., Theoretical-Study of Electronic, Magnetic, and Structural-Properties of Alpha-Fe2o3 (Hematite). *Physical Review B* **1995,** 51, (12), 7441-7450.

92. Zicovich-Wilson, C. M., *LoptCG Valencia, Spain* **1998**.
93. Apra, E. Thesis U Torino. 1992.
94. Sherman, D. M., Cluster Molecular-Orbital Description of the Electronic-Structures of Mixed-Valence Iron-Oxides and Silicates. *Solid State Communications* **1986,** 58, (10), 719-723.
95. Schwertmann, U. C. R. M., *Iron oxides in the laboratory : preparation and characterization*. New York: Weinheim, 1991; p xiv, 137 p.
96. Goodenou.Jb, Coexistence of Localized and Itinerant D Electrons. *Materials Research Bulletin* **1971,** 6, (10), 967-&.
97. Feller, D.; Peterson, K. A., An examination of intrinsic errors in electronic structure methods using the Environmental Molecular Sciences Laboratory computational results database and the Gaussian-2 set. *Journal of Chemical Physics* **1998,** 108, (1), 154-176.
98. Bylaska, E. J., W. A. de Jong, K. Kowalski, T. P. Straatsma, M. Valiev, D. Wang, E. Aprà, T. L. Windus, S. Hirata, M. T. Hackler, Y. Zhao, P.-D. Fan, R. J. Harrison, M. Dupuis, D. M. A. Smith, J. Nieplocha, V. Tipparaju, M. Krishnan, A. A. Auer, M. Nooijen, E. Brown, G. Cisneros, G. I. Fann, H. Früchtl, J. Garza, K. Hirao, R. Kendall, J. A. Nichols, K. Tsemekhman, K. Wolinski, J. Anchell, D. Bernholdt, P. Borowski, T. Clark, D. Clerc, H. Dachsel, M. Deegan, K. Dyall, D. Elwood, E. Glendening, M. Gutowski, A. Hess, J. Jaffe, B. Johnson, J. Ju, R. Kobayashi, R. Kutteh, Z. Lin, R. Littlefield, X. Long, B. Meng, T. Nakajima, S. Niu, L. Pollack, M. Rosing, G. Sandrone, M. Stave, H. Taylor, G. Thomas, J. van Lenthe, A. Wong, and Z. Zhang, *"NWChem, A Computational Chemistry Package for Parallel Computers, Version 5.0" (2006), Pacific Northwest National Laboratory, Richland, Washington 99352-0999, USA.* **2005**.
99. Hariharan, P. C.; J. A. Pople, Influence Of Polarization Functions On Molecular-Orbital Hydrogenation Energies *Theoretica Chimica Acta* **1973,** 28, (3), 213-222.
100. Francl, M. M.; Pietro, W. J.; Hehre, W. J.; Binkley, J. S.; Gordon, M. S.; DeFrees, D. J.; Pople, J. A., Self-Consistent Molecular-Orbital Methods .23. A Polarization-Type Basis Set For 2nd-Row Elements *J. Chem. Phys.* **1982,** 77, (7), 3654-3665.
101. Rassolov, V.; Pople, J. A.; Ratner, M.; Windus, T. L., *J. Chem. Phys.* **1998,** 109, 1223.
102. Krishnan, R.; Binkley, J. S.; Seeger, R.; Pople, J. A., Self-Consistent Molecular-Orbital Methods .20. Basis Set For Correlated Wave-Functions *J. Chem. Phys.* **1980,** 72, (1), 650-654.
103. Clark, T.; Chandrasekhar, J.; Spitznagel, G. W.; Schleyer, P. V. R.; , Efficient Diffuse Function-Augmented Basis-Sets For Anion Calculations .3. The 3-21+G Basis Set For 1st-Row Elements, Li-F *J. Comp. Chem.* **1983,** 4, (3), 294-301.
104. Ortiz, J. V.; Hay, P. J.; Martin, R. L., Role Of D-Orbitals And F-Orbitals In The Geometries Of Low-Valent Actinide Compounds - Abinitio Studies Of U(CH3)3, Np(CH3)3, And Pu(CH3)3 *Journal of the American Chemical Society* **1992,** 114, (7), 2736-2737.
105. Schafer, A.; Huber, C.; Ahlrichs, R.; , Fully Optimized Contracted Gaussian-Basis Sets Of Triple Zeta Valence Quality For Atoms Li To Kr. *J. Chem. Phys.* **1994,** 100, (8), 5829-5835.
106. Rassolov, V.; Pople, J. A.; Ratner, M.; Windus, T. L., 6-31G* basis set for atoms K through Zn *J. Chem. Phys.* **1998,** 109, (4), 1223-1229.

107. Frisch, M. J.; Trucks, G. W.; Schlegel, H. B.; Scuseria, G. E.; Robb, M. A.; Cheeseman, J. R.; Montgomery, J., J. A. ; Vreven, T.; Kudin, K. N.; Burant, J. C.; Millam, J. M.; Iyengar, S. S.; Tomasi, J.; Barone, V.; Mennucci, B.; Cossi, M.; Scalmani, G.; Rega, N.; Petersson, G. A.; Nakatsuji, H.; Hada, M.; Ehara, M.; Toyota, K.; Fukuda, R.; Hasegawa, J.; Ishida, M.; Nakajima, T.; Honda, Y.; Kitao, O.; Nakai, H.; Klene, M.; Li, X.; Knox, J. E.; Hratchian, H. P.; Cross, J. B.; Adamo, C.; Jaramillo, J.; Gomperts, R.; Stratmann, R. E.; Yazyev, O.; Austin, A. J.; Cammi, R.; Pomelli, C.; Ochterski, J. W.; Ayala, P. Y.; Morokuma, K.; Voth, G. A.; Salvador, P.; Dannenberg, J. J.; Zakrzewski, V. G.; Dapprich, S.; Daniels, A. D.; Strain, M. C.; Farkas, O.; Malick, D. K.; Rabuck, A. D.; Raghavachari, K.; Foresman, J. B.; Ortiz, J. V.; Cui, Q.; Baboul, A. G.; Clifford, S.; Cioslowski, J.; Stefanov, B. B.; Liu, G.; Liashenko, A.; Piskorz, P.; Komaromi, I.; Martin, R. L.; Fox, D. J.; Keith, T.; Al-Laham, M. A.; Peng, C. Y.; Nanayakkara, A.; Challacombe, M.; Gill, P. M. W.; Johnson, B.; Chen, W.; Wong, M. W.; Gonzalez, C.; Pople, J. A., *Gaussian 03W*. Revision C.2 ed.; Gaussian, Inc.: Wallingford, CT, 2004.
108. Farazdel, A.; Dupuis, M.; Clementi, E.; Aviramt, A., Electric Field Induced Intramolecular Electron Transfer in
Spiro a-Electron Systems and Their Suitability as Molecular
Electronic Devices. A Theoretical Study. *Journal of the American Chemical Society* **1990,** 112, 4206-4212.
109. Rosso, K. M.; Rustad, J. R., Ab initio calculation of homogeneous outer sphere electron transfer rates: application to $M(OH_2)_6^{3+/2+}$ redox couples. *Journal of Physical Chemistry A* **2000,** 104, (29), 6718-6725.
110. Marcus, R. A., Theory Of Oxidation-Reduction Reactions Involving Electron Transfer .1. *J. Chem. Phys.* **1956,** 24, 966-978.
111. Fernandez, D. P.; Goodwin, A. R. H.; Lemmon, E. W.; Levelt Sengers, J. M. H.; Williams, R. C., *J. Phys. Chem. Ref. Data, Suppl. 1* **1997,** 26, 1125.
112. Farmer, V., The Infra-Red Spectra of Minerals. *Mineral. Soc., London* **1974**.
113. Tsuda, N.; Nasu, K.; Fujimori, A.; Siratori, K., *Electronic condition in oxides* 2nd ed. ed.; Springer-Verlag: Heidelberg, 2000; p 365.
114. Sutin, N., Electron transfer reactions in solution: A historical perspective. In *Electron Transfer-from Isolated Molecules to Biomolecules, Pt 1*, 1999; Vol. 106, pp 7-33.
115. Rosso, K. M.; Smith, D. M. A.; Wang, Z. M.; Ainsworth, C. C.; Fredrickson, J. K., Self-exchange electron transfer kinetics and reduction potentials for anthraquinone disulfonate. *J. Phys. Chem. A* **2004,** 108, (16), 3292-3303.
116. Brunschwig, B. S.; Logan, J.; Newton, M. D.; Sutin, N., A Semi-Classical Treatment of Electron-Exchange Reactions - Application to the Hexaaquoiron(Ii)-Hexaaquoiron(Iii) System. *Journal of the American Chemical Society* **1980,** 102, (18), 5798-5809.
117. Guillaumont, R.; Fanghänel, T.; Fuger, J.; Grenthe, I.; Neck, V.; Palmer, D. A.; Rand, M. H., *Update on the Chemical Thermodynamics of Uranium, Neptunium, Plutonium, Americium and Technetium*. Elsevier: 2003.
118. Gonzalez-Gil, G.; Amonette, J. E.; Romine, M. F.; Gorby, Y. A.; Geesey, G. G., Bioreduction of natural specular hematite under flow conditions *Geochimica et Cosmochimica Acta* **2005,** 69, (5), 1145-1155.

119. Sani, R. K.; Peyton, B. M.; Amonette, J. E.; Geesey, G. G., Reduction of uranium(VI) under sulfate-reducing conditions in the presence of Fe(III)-(hydr)oxides *Geochimica et Cosmochimica Acta* **2004,** 68, (12), 2639-2648.
120. Liu, C.; Zachara, J.; Zhong, L.; Kukkadupa, R.; Szecsody, J.; Kennedy, D., Influence of sediment bioreduction and reoxidation on uranium sorption *Environ. Sci. Technol.* **2005,** 39, (11), 4125-4133.
121. Qafoku, N. P.; Zachara, J. M.; Liu, C. X.; Gassman, P. L.; Qafoku, O. S.; Smith, S. C., Kinetic desorption and sorption of U(VI) during reactive transport in a contaminated Hanford sediment *Environ. Sci. Technol.* **2005,** 39, (9), 3157-3165.
122. Neck, V.; Kim, J. I., An electrostatic approach for the prediction of actinide complexation constants with inorganic ligands-application to carbonate complexes. *Radiochim. Acta* **2000,** 88, 815-822.
123. Mizuoka, K.; Grenthe, I.; Ikeda, Y., Structural and Kinetic Studies on Uranyl(V) Carbonate Complex Using 13 C NMR Spectroscopy. *Inorganic Chemistry* **2005,** 44, 4472-4474.
124. Rybakov, V. B.; Ansalov, L. A.; Kolesnichenko, V. L.; Kulikovskii, B. N.; Volkov, S. V., Crystal Structure of New U(IV) and U(V) complexes. *Russian Journal of Coordination Chemistry* **2000,** 26, (8), 594-598.
125. Grenthe, I.; Wanner, H.; Forest, I., *Chemical thermodynamics of uranium*. New York: Amsterdam, 1992; p xvii, 715 p.
126. Eelless, M. P.; Lee, S. Y., URANIUM SOLUBILITY OF CARBONATE-RICH URANIUM-CONTAMINATED SOILS. *Water, Air, and Soil Pollution* **1998,** 107, 147–162.
127. Echevarria, G.; Sheppard, M. I.; Morel, J.; Aviramt, A., Effect of pH on the sorption of uranium in soils. *Journal of Environmental Radioactivity* **2001,** 53, 257-264.
128. Abdelouas, A.; Lutze, W.; Nuttall, E., Chemical reactions of uranium in ground water at a mill tailings site. *Journal of Contaminant Hydrology* **1998,** 34, 343–361.
129. Gu, B. H.; Wu, W.-M.; -Vogel, M. A. G.; Yan, H.; Fields, M. W.; Zhou, J. Z.; Fendorf, S.; Criddle, C.; Jardine, P. M., Bioreduction of Uranium in a Contaminated Soil Column. *Environ. Sci. Technol* **2005,** 39, 4841-4847.
130. Iwatsuki, T.; Arthur, R.; K.Ota; Metcalfe, R., Solubility constraints on uranium concentrations in groundwaters
of the Tono uranium deposit, Japan. *Radiochim. Acta* **2004,** 92, 789-796.
131. Gu, B. H.; Wu, W.-M.; Ginder-Vogel, M. A.; Yan, H.; Fields, M. W.; Zhou, J. Z.; Fendorf, S.; Criddle, C.; Jardine, P. M., Bioreduction of Uranium in a Contaminated Soil Column. *Environ. Sci. Technol.* **2005,** 39, 4841-4847.
132. Mizuguchi, K.; Park, Y.-Y.; Tomiyasu, H., Electrochemical and Spectroelectrochemical Studies on Uranyl Carbonato and Aqua Complexes. *Journal of Nuclear Science and Technology* **1993,** 30, (6), 542-548.
133. Duff, M. C.; Coughlin, J. U.; Hunter, D. B., Uranium co-precipitation with iron oxide minerals. *Geochimica et Cosmochimica Acta* **2002,** 66, (20), 3533–3547.
134. Fuller, C. C.; Bargar, J. R.; Davis, J. A.; Piana, M. J., Mechanisms of Uranium Interactions with Hydroxyapatite: Implications for Groundwater Remediation. *Environ. Sci. Technol.* **2002,** 36, 158-165.

135. Mason, C. F. V.; Turney, W. R. J. R.; Thomson, B. M.; Lu, N.; Longmire, P. A.; -Brause, C. J. C., Carbonate Leaching of Uranium from Contaminated Soils. *Environ. Sci. Technol* **1997,** 31, 2707-2711.
136. Qiu, S. R.; Lai, H.-F.; Roberson, M. J.; Hunt, M. L.; Amrhein, C.; Giancarlo, L. C.; Flynn, G. W.; Yarmoff, J. A., Removal of Contaminants from Aqueous Solution by Reaction with Iron Surfaces. *Langmuir* **2000,** 16, 2230-2236.
137. Morris, D. E., Redox Energetics and Kinetics of Uranyl Coordination Complexes in Aqueous Solution. *Inor. Chem.* **2002,** 41, 3542-3547.
138. Morris, D. E., Redox Energetics and Kinetics of Uranyl Coordination Complexes in Aqueous Solution. *Inorganic Chemistry* **2002,** 41, 3542-3547.
139. Caja, J.; Pravdic, V., Contribution to the Electrochemistry of U(V) in Carbonate Solutions. *Croatica Chemica Acta* **1969,** 41, 213-222.
140. Capdeleva, H.; Vitorge, P., Temperature and Ionic Strength Influence on U(VI/V) and U(IV/III) Redox Potentials in Aqueous Acidic and Carbonate Media. *Journal of Radioanalytical and Nuclear Chemistry* **1990,** 143, (2), 403-414.
141. Nash, K. L.; Sullivan, J. C., Kinetics and Mechanisms of Actinide Redox and Complexation Reactions. In Sykes, A. G., Ed. Academic Press: New York, 1986; Vol. 5, pp 185-213.
142. Liger, E.; Charlet, L.; Van Cappellen, P., Surface catalysis of uranium(VI) reduction by iron(II) - Spectroscopic evidence for sorption and reduction. *Geochimica et cosmochimica acta* 1999, pp 2939-2955.
143. Privalov, T.; Schimmelpfennig, B.; Wahlgren, U.; Grenthe, I., Reduction of Uranyl(VI) by Iron(II) in Solutions: An Ab Initio Study. *Journal of Physical Chemistry A* **2003,** 107, 587-592.
144. Newton, T.; Baker, F., Uranium(V)-Uranium(VI) complex and its effect on Uranium(V) disproportionation rate. *Inor. Chem.* **1965,** 4, (8), 1166-1170.
145. Mizuoka, K.; Ikeda, Y., Structural changes of uranyl moiety with reduction from U(VI) to U(V). *Radiochimica Acta* **2004,** 92, (9-11), 631-635.
146. Mizuoka, K.; Tsushima, S.; Hasegawa, M.; Hoshi, T.; Ikeda, Y., Electronic spectra of pure uranyl(V) complexes: Characteristic absorption bands due to a (UO2+)-O-V core in visible and near-infrared regions. *Inorganic Chemistry* **2005,** 44, (18), 6211-6218.
147. Valiela, I.; Costa, J.; Foreman, K.; Teal, J. M.; Howes, B.; Aubrey, D., Transport of groundwater-borne nutrients from watersheds and their effects on coastal waters. *Biogeochemistry* **1990,** 10, 177-197.
148. Newton, T. W., The kinetics of the Oxidation - Reduction Reactions of Uranium, Neptunium, Plutonium and
Americium in Aqueous Solutions. In Administration, U. S. E. R. a. D., Ed. U.S. Government: 1975; Vol. TID-26506.
149. Bernhard, G.; Geipel, G.; Reich, T.; Brendler, V.; Amayri, S.; Nitsche, H., Uranyl(VI) carbonate complex formation: Validation of the Ca2UO2(CO3)(3)(aq.) species. *Radiochimica Acta* **2001,** 89, (8), 511-518.
150. Rosso, K. M.; Smith, D. M. A.; Dupuis, M., An ab initio model of electron transport in hematite (alpha-Fe2O3) basal planes. *J. Chem. Phys.* **2003,** 118, (14), 6455-6466.

151. Rosso, K. M.; Morgan, J. J., Outer-sphere electron transfer kinetics of metal ion oxidation by molecular oxygen. *Geochimica Cosmochimica Acta* **2002,** 66, (24), 4223-4233.
152. Iordanova, N.; Duipuis, M.; Rosso, K. M., Charge Transport in Metal Oxides; A theoretical study of hematite α-Fe_2O_3. *The Journal of Chemical Physics* **2005,** 122, 144305-.
153. Kaltsoyannis, N., Recent developments in computational actinide chemistry. *Chemical Society Reviews* **2003,** 32, (1), 9-16.
154. Kaltsoyannis, N., Relativistic effects in inorganic and organometallic chemistry. *Journal of the Chemical Society-Dalton Transactions* **1997**, (1), 1-11.
155. Kaltsoyannis, N., Computational study of analogues of the uranyl ion containing the -N=U=N- unit: Density functional theory calculations on UO22+, UON+, UN2, UO(NPH3)(3+), U(NPH3)(2)(4+), [UCl4{NPR3}(2)] (R = H, Me), and [UOCl4{NP(C6H5)(3)}](-). *Inor. Chem.* **2000,** 39, (26), 6009-6017.
156. Polihronov, J. G.; Hedstrom, M.; Hummel, R. E.; Cheng, H.-P., Semi-empirical calculation of the optical spectra of slilica clusters in spark-procesed silicon. *Journal of Luminescence* **2002,** 96, (2002), 119-128.
157. Smith, W.; Forester, T. R., DL_POLY is a package of molecular simulation routines copyright The Council for the Central Laboratory of the Research Councils, Daresbury Laboratory at Daresbury, Nr. Warrington. **1996**.
158. Born, M.; Huang, K., *Dynamical Theory of Crystal Lattices*. Oxford University Press: Oxford, UK, 1954.
159. Dick, B. G.; Overhauser, A. W., Theory of the dielectric constants of alkali halide crystals. *Physical Reviews* **1958,** 112, 90-103.
160. Hoover, W. G., Canonical dynamics - equilibrium phase-space distributions. *Physical Review A* **1985,** 31, 1695-1697.
161. Melchionna, S.; Ciccotti, G.; Holian, B. L., Hoover NPT dynamics for systems varying in shape and size. *Molecular Physics* **1993,** 78, 533-544.
162. Ewald, P. P., Die Berechnung optischer und elektrostatischer Gitterpotentiale. *Annalen der Physik* **1921,** 64, 253-287.
163. Mitchell, P. J.; Fincham, D., Shell model simulations by adiabatic dynamics. *Journal of Physics: Condensed Matter* **1993,** 5, 1031-1038.
164. de Leeuw, N. H.; Parker, S. C., Molecular-dynamics simulation of MgO surfaces in liquid water using a shell-model potential for water. *Physical Review B* **1998,** 58, (20), 13901-13908.
165. Kerisit, S.; Parker, S. C., Free energy of adsorption of water and metal ions on the {1014} calcite surface. *Journal of the American Chemical Society* **2004,** 126, 10152-10161.
166. Guilbaud, P.; Wipff, G., Hydration of UO2+ cation and its NO3- and 18-Crown-6 adducts studied by molecular dynamics simulations. *J. Phys. Chem.* **1993,** 97, 5685-5692.
167. Guilbaud, P.; Wipff, G., Force field representation of the UO2+ cation from free energy MD simulations in water on its 18-crown-6 and NO3- adducts, and on its calix[6]arene-6 and CMPO complexes. *Journal Of Molecular Structure* **1996,** 366, 55-63.
168. Lewis, G. V.; Catlow, C. R. A., Potential models for ionic oxides. *Journal of Physics C: Solid State Physics* **1985,** 18, 1149-1161.

169. Hagberg, D.; Karlstrom, G.; Roos, B. O.; Gagliardi, L., The coordination of uranyl in water: A combined quantum chemical and molecular simulation study. *Journal of the American Chemical Society* **2005,** 127, (41), 14250-14256.
170. Pavese, A.; Catti, M.; Parker, S. C.; Wall, A., Modelling of the thermal dependence of structural and elastic properties of calcite, $CaCO_3$. *Physics and Chemistry of Minerals* **1996,** 23, 89-93.
171. de Leeuw, N. H.; Parker, S. C., Surface structure and Morphology of calcium carbonate polymorphs calcite, aragonite, and vaterite: an atomistic approach. *J. Phys. Chem. B* **1998,** 102, 2914-2922.
172. Duffy, D. M.; Harding, J. H., Modelling the interfaces between calcite crystals and Langmuir monolayers. *Journal of Materials Chemistry* **2002,** 12, 3419-3425.
173. Kristensen, R.; Stipp, S. L. S.; Refson, K., Modeling steps and kinks on the surface of calcite. *J. Chem. Phys.* **2004,** 121, (17), 8511-8523.
174. Kerisit, S.; Cooke, D. J.; Spagnoli, D.; Parker, S. C., Molecular dynamics simulations of the interactions between water and inorganic solids. *Journal Of Materials Chemistry* **2005,** 15, 1454-1462.
175. Hemmingsen, L.; Amara, P.; Ansoborlo, E.; Field, M. J., Importance of charge transfer and polarization effects for the modeling of uranyl-cation complexes. *J. Phys. Chem. A* **2000,** 104, 4095-4101.
176. Gagliardi, L.; Grenthe, I.; Roos, B. O., A theoretical study of the structure of tricarbonatodioxouranate. *Inor. Chem.* **2001,** 40, 2976-2978.
177. Vazquez, J.; Bo, C.; Poblet, J. M.; de Pablo, J.; Bruno, J., DFT studies of uranyl acetate, carbonate, and malonate, compexes in solution. *Inorganic Chemistry* **2003,** 42, 6136-6141.
178. Curtiss, L. A.; Halley, J. W.; Hautman, J.; Rahman, A., Nonadditivity of ab initio pair potentials for molecular dynamics of multivalent transition metal in water. *J. Chem. Phys.* **1987,** 86, (4), 2319-2327.
179. Aprà, E.; Windus, T. L.; Straatsma, T. P.; Bylaska, E. J.; de Jong, W.; Hirata, S.; Valiev, M.; Hackler, M.; Pollack, L.; Kowalski, K.; Harrison, R.; Dupuis, M.; Smith, D. M. A.; Nieplocha, J.; V., T.; Krishnan, M.; Auer, A. A.; Brown, E.; Cisneros, G.; Fann, G.; Fruchtl, H.; Garza, J.; Hirao, K.; Kendall, R.; Nichols, J.; Tsemekhman, K.; Wolinski, K.; Anchell, J.; Bernholdt, D.; Borowski, P.; Clark, T.; Clerc, D.; Dachsel, H.; Deegan, M.; Dyall, K.; Elwood, D.; Glendening, E.; Gutowski, M.; Hess, A.; Jaffe, J.; Johnson, B.; Ju, J.; Kobayashi, R.; Kutteh, R.; Lin, Z.; Littlefield, R.; Long, X.; Meng, B.; Nakajima, T.; Niu, S.; Rosing, M.; Sandrone, G.; Stave, M.; Taylor, H.; Thomas, G.; van Lenthe, J.; Wong, A.; Zhang, Z. *NWChem, A Computational Chemistry Package for Parallel Computers, Version 4.7*, Pacific Northwest National Laboratory: Richland, Washington 99352-0999, USA., 2005.
180. Stevens, P. J.; Devlin, F. J.; Chabalowski, C. F.; Frisch, M. J., Ab-Inition Calculation of VIbrational Absorption and Circular-Dichroism Spectra using Density Functional Force-Fields. *Journal of Physical Chemistry* **1994,** 98, (45), 11623-11627.
181. Richens, D. T., *The Chemistry of Aqua Ions; Synthesis, Structure and reactivity; A periodic tour through the elements*. John Wiley: Chichester, 1997; p 592.
182. Hariharan, P. C.; J. A. Pople, Influence Of Polarization Functions On Molecular-Orbital Hydrogenation Energies *Theoretica Chimica Acta* **1973,** 28, (3), 213-222.

183. Rassolov, V.; Pople, J. A.; Ratner, M.; Windus, T. L., 6-31G* basis set for atoms K through Zn *J. Chem. Phys.* **1998,** 109, (4), 1223-1229.
184. Clark, T.; Chandrasekhar, J.; Spitznagel, G. W.; Schleyer, P. V. R.; , Efficient Diffuse Function-Augmented Basis-Sets For Anion Calculations .3. The 3-21+G Basis Set For 1st-Row Elements, Li-F *J. Comp. Chem.* **1983,** 4, (3), 294-301.
185. Kuechle, W., to be published
186. Farazdel, A.; Dupuis, M.; Clementi, E.; Aviramt, A., Electric Field Induced Intramolecular Electron Transfer in Spiro a-Electron Systems and Their Suitability as Molecular Electronic Devices. A Theoretical Study. *Journal of the American Chemical Society* **1990,** 112, 4206-4212.
187. Docrat, T. I.; Mosselmans, J. F. W.; Charnock, J. M.; Whiteley, M. W.; Collison, D.; Livens, F. R.; Jones, C.; Edmiston, M. J., X-ray absorption spectroscopy of tricarbonatodioxouranate(V), [UO2(CO3)(3)](5-), in aqueous solution. *Inor. Chem.* **1999,** 38, (8), 1879-1882.
188. Cora, F.; Stachiotti, M. G.; Catlow, C., Transition metal oxide chemistry: Elecronic structure study of WO_3, $ReO_3$and $NaWO_3$. *Journal of Physical Chemistry* **1997,** 101, 3945-3952.
189. Lundberg, M.; Siegbahn, P. E. M., Quantifying the effects of the self-interaction error in DFT: When do the delocalized states appear? *J. Chem. Phys.* **2005,** 122, (22), Art. No. 224103
190. Baric, D.; Maksic, Z. B., Atomic additivity of the correlation energy in molecules by the DFT-B3LYP scheme. *J. Phys. Chem. A* **2003,** 107, (51), 11577-11586.
191. Polo, V.; Kraka, E.; Cremer, D., Electron correlation and the self-interaction error of density functional theory. *Molecular Physics* **2002,** 100, (11), 1771-1790.
192. Polo, V.; Kraka, E.; Cremer, D., Some thoughts about the stability and reliability of commonly used exchange-correlation functionals - coverage of dynamic and nondynamic correlation effects. *Theoretical Chemistry Accounts* **2002,** 107, (5), 291-303.
193. Csonka, G. I.; Johnson, B. G., Inclusion of exact exchange for self-interaction corrected H-3 density functional potential energy surface. *Theoretical Chemistry Accounts* **1998,** 99, (3), 158-165.
194. Marcus, R. A.; Sutin, N., electron transfers in chemistry and biology. *Biochimica et Biophysical Acta* **1985,** 811, 265-322.
195. Skodje, R. T.; Truhlar, D. G.; Garrett, B. C., Vibrationally Adiabatic Models for Reactive Tunneling. *Journal of Chemical Physics* **1982,** 77, (12), 5955-5976.
196. Skodje, R. T.; Truhlar, D. G., Parabolic Tunneling Calculations. *J. Phys. Chem.* **1981,** 85, (6), 624-628.
197. Peng, C. Y.; Schlegel, H. B., Combining Synchronous Transit and Quasi-Newton Methods to Find Transition-States. *Israel Journal of Chemistry* **1993,** 33, (4), 449-454.
198. Jensen, A., Location of Transition-States and Stable Intermediates by Minimax Minimi Optimization of Synchronous Transit Pathways. *Theoretica Chimica Acta* **1983,** 63, (4), 269-290.
199. Halgren, T. A.; Lipscomb, W. N., Synchronous-Transit Method for Determining Reaction Pathways and Locating Molecular Transition-States. *Chemical Physics Letters* **1977,** 49, (2), 225-232.
200. Mayer, J. M., Proton-Coupled Electron Transfer: A Reaction Chemist's View. *Annual Reviews in Physical Chemistry* **2004,** 55, 363-390.

201. Gratzel, M., *Heterogeneous photochemical electron transfer*. CRC: Boca Raton, 1989.
202. Moraes, J. E.; Quina, F. H.; Nascimento, C. A.; Silva, D. N.; Chiavone-Filho, O., Treatment of saline wastewater contaminated with hydrocarbons by the photo-Fenton process. *Environ Sci Technol* **2004,** 38, (4), 1183-7.
203. Wester, D. W.; Sullivan, J. C., Electrochemical And Spectroscopic Studies Of Uranium(IV), Uranium(V), And Uranium(VI) In Carbonate-Bicarbonate Buffers *Inor. Chem.* **1980,** 19, (9), 2838-2840.
204. Parks, G. A., Surface energy and adsorption at mineral/water interfaces: an introduction. In *Mineral-water interface geochemistry*, Hochella, M. F.; White, A. F., Eds. Mineral Society of America: Washington, D.C., 1990; Vol. 23, pp 133-176.
205. Fenter, P.; Cheng, L.; Rihs, S.; Machesky, M.; Bedzyk, M. J.; Sturchio, N. C., Electrical double-layer structure at the rutile-water interface as observed in situ with small-period X-ray standing waves. *Journal of Colloid and Interface Science* **2000,** 225, (1), 154-165.
206. Bockris, J. O.; Reddy, A. K. N.; Gamboa-Aldeco, M., *Modern Electrochemistry : Electrodics and Related Fields 2A: Fundamentals of Electrodics*. Kluwer Academic, Plenum Publishers: New York, 2000.
207. Spohr, E., Some recent trends in computer simulations of aqueous double layers. *Electrochimica Acta* **2003,** 49, 23-27.
208. Helmholtz, H. v., A theorem of the distribution of electrical currents in material conductors. *Bericht u¨ber die zur Bekanntmachung geeigneten Verhandlungen der Ko¨nigl. Preuss. Akademie der Wissenschaften zu Berlin* **1852**, 466-68.
209. Helmholtz, H. v., Ueber einige Gesetze der Vertheilung eleltrischer Strome in korperlichen Leitern, mit Anwendung auf die thierisch-elektrischen Versuche. *annalen der physik und chemie* **1853,** 89, (7), 353-377.
210. Chapman, D., A Contribution to the Theory of Electrocapilarity. *the London, Edinberg, and Dublin philosophical magazine and Journal of Science* **1913,** 25, 475-81.
211. Gouy, M., Charge Electrique a la Surface d'un Electrolyte *J. de Physique* **1910,** 9.
212. Stern, O., Zur thteorie der elektrolytischen doppelschicht. *Zeitschrift fur electrochem.* **1924,** 30, 508-516.
213. Yates, D. E.; Levine, S.; Healy, T. W., Site-Binding Model of Electrical Double-Layer at Oxide-Water Interface. *Journal of the Chemical Society-Faraday Transactions I* **1974,** 70, 1807-1818.
214. Davis, J. A.; James, R. O.; Leckie, J. O., Surface Ionization and Complexation at Oxide-Water Interface .1. Computation of Electrical Double-Layer Properties in Simple Electrolytes. *Journal of Colloid and Interface Science* **1978,** 63, (3), 480-499.
215. Lyklema, J., Electrified Interfaces In Aqueous Dispersions Of Solids. *Pure & Appl. Chem.* **1991,** 63, (6), 895-906.
216. Gregory, J., *Particles in Water: Properties and Processes*. IWA Publisher: Boca Raton, London, New York, 2006.
217. Kuznetsov, A. M.; Ulstrup, J., Theory of electron transfer at electrified interfaces. *Electrochimica Acta* **2000,** 45, (15-16), 2339-2361.
218. McCafferty, E.; Zettlemoyer, A. C., Adsorption of Water Vapour on α-Fe_2O_3. *Disc. Farad. Soc.* **1971,** 52, 239-255.

219. Magdans, U.; Gies, H.; Torrelles, X.; Rius, J., Investigation of the {104} surface of calcite under dry and humid atmospheric conditions with grazing incidence X-ray diffraction (GIXRD). *European Journal of Mineralogy* **2006,** 18, (1), 83-91.
220. Chiarello, R. P.; Sturchio, N. C., The Calcite (10(1)over-Bar-4) Cleavage Surface in Water - Early Results of a Crystal Truncation Rod Study. *Geochimica et Cosmochimica Acta* **1995,** 59, (21), 4557-4561.
221. Eng, P. J.; Trainor, T. P.; Brown, G. E.; Waychunas, G. A.; Newville, M.; Sutton, S. R.; Rivers, M. L., Structure of the hydrated alpha-Al2O3 (0001) surface. *Science* **2000,** 288, (5468), 1029-1033.
222. Trainor, T. P.; Eng, P. J.; Brown, G. E.; Robinson, I. K.; De Santis, M., Crystal truncation rod diffraction study of the alpha-Al2O3 (1(1)over-bar-0 2) surface. *Surface Science* **2002,** 496, (3), 238-250.
223. Tanwar, K. S.; Lo, C. S.; Eng, P. J.; Catalano, J. G.; Walko, D. A.; Brown, G. E.; Waychunas, G. A.; Chaka, A. M.; Trainor, T. P., Surface diffraction study of the hydrated hematite (1(1)over-bar-02) surface. *Surface Science* **2007,** 601, (2), 460-474.
224. Waychunas, G.; Trainor, T.; Eng, P.; Catalano, J.; Brown, G.; Davis, J.; Rogers, J.; Bargar, J., Surface complexation studied via combined grazing-incidence EXAFS and surface diffraction: arsenate an hematite (0001) and (10-12). *Analytical and Bioanalytical Chemistry* **2005,** 383, (1), 12-27.
225. Henderson, D.; Gillespie, D.; Nagy, T.; Boda, D., Monte Carlo simulation of the electric double layer: dielectric boundaries and the effects of induced charge. *Molecular Physics* **2005,** 103, (21-23), 2851-2861.
226. Hayes, K. F.; Redden, G.; Ela, W.; Leckie, J. O., Surface Complexation Models - an Evaluation of Model Parameter-Estimation Using Fiteql and Oxide Mineral Titration Data. *Journal of Colloid and Interface Science* **1991,** 142, (2), 448-469.
227. Sverjensky, D. A.; Fukushi, K., Anion Adsorption on Oxide Surfaces: Inclusion of the Water Dipole in Modeling the Electrostatics of Ligand Exchange. *Environm. Sci & Technol.* **2006,** 40, 263-271.
228. Sverjensky, D. A., Interpretation and prediction of triple-layer model capacitances and the structure of the oxide-electrolyte-water interface. *Geochimica et Cosmochimica Acta* **2001,** 65, (21), 3543-3655.
229. Archer, D. G.; Wang, P., The dielectric constant of water and Debye-Huckel limiting law slopes. *Journal of Physical Chemistry* **1990,** 19, (2), 371-407.
230. Kharkats, Y. I.; Nielsen, H.; Ulstrup, J., The Effect of a Low Dielectric-Constant Interlayer on the Current Voltage Relationship for Simple Electrode Processes. *Journal of Electroanalytical Chemistry* **1984,** 169, (1-2), 47-57.
231. Cances, E.; Mennucci, B.; Tomasi, J., A new integral equation formalism for the polarizable continuum model: theoretical background and applications to isotropic and anisotropic dielectrics. *J. Chem. Phys.* **1997,** 107, (8), 3032-3041.
232. Oster, G.; Kirkwood, J. G., The influence of hindered molecular rotation on the dielectric constants of water, alcohols, and other polar liquids. *Journal of Chemical Physics* **1943,** 11, (4), 0175-0178.
233. Ballenegger, V.; Hansen, J.-P., Dielectric permittivity profiles of confined polar fluids. *The Journal of Chemical Physics* **2005,** 122, 114711-114721.

234. Omelyan, I. P., Transverse wavevector dependent and frequency dependent dielectric function, magnetic permittivity and generalized conductivity of interaction site Fuids: MD calculations for the TIP4P water. *Molecular Physics* **1999,** 96, (3), 407-427.
235. Yeh, I.-C.; Berkowitz, M. L., Dielectric constant of water at high electric fields: Molecular dynamics study. *Journal of Chemical Physics* **1999,** 110, (16), 7935-7942.
236. Stern, H. A.; Feller, S. E., Calculation of the dielectric permittivity profile for a nonuniform system: Application to a lipid bilayer simulation. *Journal of Chemical Physics* **2003,** 118, (7), 3401-3412.
237. Bursulaya, B. D.; Kim, H. J., Spectroscopic and dielectric properties of liquid water: A molecular dynamics simulation study. *Journal of Chemical Physics* **1998,** 109, (12), 4911-4919.
238. Watanabe, M.; Brodsky, A. M.; Reinhardt, W. P., Dielectric-Properties and Phase-Transitions of Water between Conducting Plates. *Journal of Physical Chemistry* **1991,** 95, (12), 4593-4596.
239. Bruesch, P.; Christien, T., The electric double layer at a metal electrode in pure water. *Journal of Applied Physics* **2004,** 95, (5), 2846-2856.
240. Weidler, P. G.; Hug, S. J.; Wetche, T. P.; Hiemstra, T., Determination of Growth Rates of (100) and (110) faces of synthetic goethite by scanning force microscopy. *Geochimica et Cosmochimica Acta* **1998,** 62, (21/22), 3407-3412.
241. Szytuta, A.; Burewicz, A.; Dimitrijevic, Z.; Krasnicki, S.; Rzany, H.; Todorovic, J.; Wanic, A.; Wolski, W., Goethite Redetermination. In *Structure Reports*, Pearson, W. B.; Duckworth, V., Eds. Osthoek, Sheltema & Holkema: Utrecht, 1968; Vol. 33A.
242. *Accelerys Software Inc. Cerius2 Version 4* **2005**
243. Hiemstra, T.; Van Riemsdijk, W. H.; Bolt, G. H., Multisite Proton Adsorption Modeling at the Solid/Solution Interface of (Hydr)oxides: A New Approach. I. Model Description and Evaluation of Intrinsic Reaction Constants. *Journal of Colloid and Interface Science* **1989,** 133, 91-104.
244. Hiemstra, T.; Van Riemsdijk, W. H., A Surface Structural Approach to Ion Adsorption: The Charge Distribution (CD) Model. *Journal of Colloid and Interface Science* **1996,** 179, 488-508.
245. Plimpton, J.; Pollock, R.; Stevens, M., Particle-Mesh Ewald and rRESPA for Parallel Molecular Dynamics Simulations. *Proc of the Eighth SIAM Conference on Parallel Processing for Scientific Computing in Minneapolis, MN* **1997**.
246. Plimpton, S. J., Fast Parallel Algorithms for Short-Range Molecular Dynamics. *J Comp Phys* **1995,** 117, 1-19.
247. Cygan, R. T.; Liang, J.-J.; Kalinichev, A. G., Molecular Models of Hydroxide, Oxyhydroxide, and Clay Phases and the Development of a General Force Field. *The Journal of Physical Chemistry B* **2004**.
248. Berendsen, H. J. C. P., J. P. M.; van Gunsteren, W. F.; Hermans, J., Interaction models for water in relation to protein hydration. In *Intermolecular Forces*, Pullman, B., Ed. 1981.
249. Reidel, D.; Teleman, O.; Jonsson, B.; Engstrom, S., A molecular dynamics simulation of a water model with intramolecular degrees of freedom. *Molecular Physics* **1987,** 60, 193-203.
250. Wallqvist, A.; Teleman, O., Properties of Flexible Water Models. *Molecular Physics* **1991,** 74, (3), 515-533.

251. Kalinichev, A., *Personal Communication*.
252. Richardi, J.; Fries, P. H.; Millot, C., Fast hybrid methods for the simulation of dielectric constants of liquids. *Journal of Molecular Liquids* **2005,** 117, 3-16.
253. Mizan, T. I.; Savage, P. E.; Ziff, R. M., Molecular-Dynamics of Supercritical Water Using a Flexible Spc Model. *Journal of Physical Chemistry* **1994,** 98, (49), 13067-13076.
254. Lileev, A. S.; Filimonova, Z. A.; Lyashchenko, A. K., Dielectric permittivity and relaxation in aqueous solutions of alkali metal sulfates and nitrates in the temperature range 288-313 K. *Journal of Molecular Liquids* **2003,** 103, 299-308.
255. Hiemstra, T.; Yong, H.; Van Riemsdijk, W. H., Interfacial charging phenomena of aluminum (hydr)oxides. *Langmuir* **1999,** 15, (18), 5942-5955.
256. Navarro-Gonzalez, R.; McKay, C. P.; Mvondo, D. N., A possible nitrogen crisis for Archean life due to reduced nitrogen fixation by lighting. *Nature* **2001,** 412, 61-64.
257. Summers, D. P.; Lerner, N., Ammonia from iron(ii) reduction of nitrite and the Strecker synthesis: do iron(II) and cyanide interfere with each other? *Orig. Life Evol. Biosphere* **1998,** 28, 1-11.
258. Summers, D. P.; Chang, S., Prebiotic ammonia from reduction of nitrite by iron(II) on the early earth. *Nature* **1993,** 365, 630-632.
259. Summers, D. P., Ammonia formation by the reduction of nitrite/nitrate by FeS: Ammonia formation under acidic conditions. *Origins of Life and Evolution of the Biosphere* **2005,** 35, (4), 299-312.
260. Smirnov, A. Formation and Fate of Ammonium in the Hadean Ocean. Stony Brook University, Stony Brook, NY, 2006.
261. Strongin, D. R.; Somorjai, G. A., A surface science and catalytic study of the effects of aluminum oxide and potassium on the ammonia synthesis over iron oxide single crystal surfaces. In *Catalytic Ammonia Synthesis: Fundamentals and Practice*, Jennings, J. R., Ed. Plenum Press: London, 1991; pp 133-177.
262. Schoonen, M. A. A.; Xu, Y., Nitrogen reduction under hydrothermal vent conditions: implications for the prebiotic synthesis of C-H-O-N compounds. *Astrobiology* **2001,** 1, (2), 133-140.
263. Dorr, M.; Kasbohrer, J.; Grunert, R.; Kreisel, G.; Brand, W. A.; Werner, R. A.; Geilmann, H.; Apfel, C.; Robl, C.; Weigand, W., A possible prebiotic formation of ammonia from dinitrogen on iron oxide surfaces. *Angewandte Chemie, International Edition in English* **2003,** 42, 1540-1543.
264. Zhang, X. V.; Martin, S. T.; Friend, C. M.; Schoonen, M. A. A.; Holland, H. D., Mineral-assisted pathways in prebiotic synthesis: Photoelectrochemical reduction of carbon(+IV) by manganese sulfide. *Journal of the American Chemical Society* **2004,** 126, (36), 11247-11253.
265. Schrauzer, G. N.; Guth, T. D., Hydrogen evolving systems. 1. The formation of H_2 from aqueous suspensions of $Fe(OH)_2$ and Reactions with Reducible substrates, Including molecular nitrogen. *Journal of the American Chemical Society* **1976,** 98, (12), 3508-3513.
266. Denisov, N. T.; Zueva, A. F.; Shilova, A. K., Apropos of a communication of the reduction of nitrogen by iron(II) hydroxide. *Kinetika i Kataliz* **1978,** 19, (1), 267.

267. Mauzerall, D. C., The Photochemical Origins of Life and Photoreaction of Ferrous Ion in the Archean Oceans. *Origins of Life and Evolution of the Biosphere* **1990,** 20, (3-4), 293-302.
268. Mauzerall, D.; Borowska, Z.; Zielinski, I., Photo and Thermal-Reactions of Ferrous Hydroxide. *Origins of Life and Evolution of the Biosphere* **1993,** 23, (2), 105-114.
269. Genin, J. M. R.; Abdelmoula, M.; Aissa, R.; Ruby, C., Ordering in FeII-III hydroxysalt green rusts from XRD and Mossbauer analysis (chloride, carbonate, sulphate, oxalate ...); about the structure of hydrotalcite-like compounds. *Hyperfine Interactions* **2006,** 166, (1-4), 391-396.
270. Brandes, J. A.; Boctor, N. Z.; Cody, G. D.; Cooper, B. A.; Hazen, R. M.; Yoder, H. S., Jr., Abiotic nitrogen reduction on the early Earth. *Nature* **1998,** 395, 365-367.
271. Alberty, R. A., Thermodynamics of Nitrogenase Reactions. *THE JOURNAL OF BIOLOGICAL CHEMISTRY* **1994,** 269, (10), 7099-7012.
272. Shilov, A. E., Dinitrogen fixation in solution in the presence of iron complexes. intermediates and mechanism. *New Journal of Chemistry* **1992,** 16, 213-218.
273. Strajescu, M.; Gabrus, R.; Bratean, C.; Jeleriu, S., Dinitrogen reduction in hydroxide systems of Mo3+, Fe2+, Ti3+, and Mg2+. *Revue Roumaine de Chimie* **1997,** 42, (6), 435-438.
274. Jin, X.; Cao, Z. X.; Zhang, Q. E., A theoretical study of interaction between dinitrogen and single transition-metal centers Mo, Fe and V. *Chemical Journal of Chinese Universities-Chinese* **2005,** 26, (8), 1522-1526.
275. Strajescu, M.; Jeleriu, S.; Volosnic, M.; Margineanu, F.; Vicol, M., Reductive Abiotic Fixation of Molecular Nitrogen .2. *Revista De Chimie* **1984,** 35, (1), 59-65.
276. Braterman, P. S.; Cairnssmith, A. G.; Sloper, R. W.; Truscott, T. G.; Craw, M., Photo-Oxidation of Iron(Ii) in Water between pH 7.5 and 4.0. *Journal of the Chemical Society-Dalton Transactions* **1984**, (7), 1441-1445.
277. Schwertmann, U.; Cambier, P.; Murad, E., Properties of Goethites of Varying Crystallinity. *Clays and Clay Minerals* **1985,** 33, (5), 369-378.
278. Rasmus, K. E.; Graneli, W.; Wangberg, S. A., Optical studies in the Southern Ocean. *Deep-Sea Research Part Ii-Topical Studies in Oceanography* **2004,** 51, (22-24), 2583-2597.
279. Schrauzer, G. N.; Guth, T. D., Hydrogen evolving systems .1. Formation of H_2 from aqueous suspensions of $Fe(OH)_2$ and reactions with reducible substrates, including molecular nitrogen. *Journal of the American Chemical Society* **1976,** 98, (12), 3508-3513.
280. Kelly, C. A.; Rosseinsky, D. R., Estimates of hydride ion stability in condensed systems: energy of formation and solvation in aqueous and polar-organic solvents. *Physical Chemistry Chemical Physics* **2001,** 3, (11), 2086-2090.
281. Zhan, C. G.; Dixon, D. A., The nature and absolute hydration free energy of the solvated electron in water. *Journal of Physical Chemistry B* **2003,** 107, (18), 4403-4417.
282. Shilov, A. E., In *A Treatise on Dinitrogen Fixation*, Hardy, R. W. F.; Bottomley, F.; Burns, R. C., Eds. Wiley: new York, 1979; p 31.
283. Liger, E.; Charlet, L.; Cappellen, P. V., Surface catalysis of uranium(VI) reduction by iron(II). *Geochimica et Cosmochimica Acta* **1999,** 63, (19/20), 2939-2955.

284. Morse, J. W.; Mackenzie, F. T., Hadean ocean carbonate geochemistry. *Aquatic Geochemistry* **1998,** 4, (3-4), 301-319.
285. Kelley, D. S.; Karson, J. A.; Blackman, D. K.; Fruh-Green, G. L.; Butterfield, D. A.; Lilley, M. D.; Olson, E. J.; Schrenk, M. O.; Roe, K. K.; Lebon, G. T.; Rivvizzigno, P.; Party, A.-S., An off-axis hydrothermal vent field near Mid-Atlantic Ridge at 30°N. *Nature* **2001,** 412, 145-149.
286. Kasting, J. F., Bolide impacts and the oxidation state of carbon in the Earth's early atmosphere. *Origins of Life* **1990,** 20, (199-231).
287. Chatt, J.; Dilworth, J. R.; Richards, R. L., Recent Advances in Chemistry of Nitrogen-Fixation. *Chemical Reviews* **1978,** 78(6), „ (6), 589-625.
288. Holland, H. D., *The chemical evolution of the atmosphere and oceans*. Princeton University Press: Princeton, 1984; p 582.
289. Zones, S. I.; Vickrey, T. M.; Palmer, J. G.; Schrauzer, G. N., The reduction of molecular nitrogen, organics substrates and protons by Vanadium(II). *Journal of the American Chemical Society* **1976,** 98, (23), 7289-7295.
290. Dorr, M.; Kassbohrer, J.; Grunert, R.; Kreisel, G.; Brand, W. A.; Werner, R. A.; Geilmann, H.; Apfel, C.; Robl, C.; Weigand, W., A possible prebiotic formation of ammonia from dinitrogen on iron sulfide surfaces. *Angewandte Chemie-International Edition* **2003,** 42, (13), 1540-1543.
291. Kurnikov, I. V.; Charnley, A. K.; Beratan, D. N., From ATP to electron transfer: Electrostatics and free-energy transduction in nitrogenase. *Journal of Physical Chemistry B* **2001,** 105, (23), 5359-5367.
292. Schrock, R. R., Reduction of dinitrogen. *Proceedings of the National Academy of Sciences of the United States of America* **2006,** 103, (46), 17087-17087.
293. Hinnemann, B.; Norskov, J. K., Catalysis by enzymes: The biological ammonia synthesis. *Topics in Catalysis* **2006,** 37, (1), 55-70.
294. Fisher, K.; Newton, W. E.; Lowe, D. J., Electron paramagnetic resonance analysis of different Azotobacter vinelandii nitrogenase MoFe-protein conformations generated during enzyme turnover: Evidence for S = (3)/(2) spin states from reduced MoFe-protein intermediates. *Biochemistry* **2001,** 40, (11), 3333-3339.
295. Barney, B. M.; Lee, H. I.; Dos Santos, P. C.; Hoffmann, B. M.; Dean, D. R.; Seefeldt, L. C., Breaking the N-2 triple bond: insights into the nitrogenase mechanism. *Dalton Transactions* **2006**, (19), 2277-2284.
296. Xiao, Y. M.; Fisher, K.; Smith, M. C.; Newton, W. E.; Case, D. A.; George, S. J.; Wang, H. X.; Sturhahn, W.; Alp, E. E.; Zhao, J. Y.; Yoda, Y.; Cramer, S. P., How nitrogenase shakes - Initial information about P-cluster and FeMo-cofactor normal modes from nuclear resonance vibrational Spectroscopy (NRVS). *Journal of the American Chemical Society* **2006,** 128, (23), 7608-7612.
297. Lukoyanov, D.; Barney, B. M.; Dean, D. R.; Seefeldt, L. C.; Hoffman, B. M., Connecting nitrogenase intermediates with the kinetic scheme for N-2 reduction by a relaxation protocol and identification of the N-2 binding state. *Proceedings of the National Academy of Sciences of the United States of America* **2007,** 104, (5), 1451-1455.
298. Burgess, B. K.; Lowe, D. J., Mechanism of molybdenum nitrogenase. *Chemical Reviews* **1996,** 96, (7), 2983-3011.

299. Dance, I., The mechanistically significant coordination chemistry of dinitrogen at FeMo-co, the catalytic site of nitrogenase. *Journal of the American Chemical Society* **2007,** 129, (5), 1076-1088.
300. Hendrich, M. P.; Gunderson, W.; Behan, R. K.; Green, M. T.; Mehn, M. P.; Betley, T. A.; Lu, C. C.; Peters, J. C., On the feasibility of N-2 fixation via a single-site Fe-I/Fe-IV cycle: Spectroscopic studies of Fe-I(N-2)Fe-I, Fe-IV N, and related species. *Proceedings of the National Academy of Sciences of the United States of America* **2006,** 103, (46), 17107-17112.
301. Kastner, J.; Hemmen, S.; Blochl, P. E., Activation and protonation of dinitrogen at the FeMo cofactor of nitrogenase. *Journal of Chemical Physics* **2005,** 123, (7).
302. Leigh, G. J., The Mechanism of Dinitrogen Reduction by Molybdenum Nitrogenases. *European Journal of Biochemistry* **1995,** 229, (1), 14-20.
303. Einsle, O.; Tezcan, F. A.; Andrade, S. L. A.; Schmid, B.; Yoshida, M.; Howard, J. B.; Rees, D. C., Nitrogenase MoFe-protein at 1.16 angstrom resolution: A central ligand in the FeMo-cofactor. *Science* **2002,** 297, (5587), 1696-1700.
304. Hinnemann, B.; Norskov, J. K., Chemical activity of the nitrogenase FeMo cofactor with a central nitrogen ligand: Density functional study. *Journal of the American Chemical Society* **2004,** 126, (12), 3920-3927.
305. Lee, H. I.; Benton, P. M. C.; Laryukhin, M.; Igarashi, R. Y.; Dean, D. R.; Seefeldt, L. C.; Hoffman, B. M., The interstitial atom of the nitrogenase FeMo-cofactor: ENDOR and ESEEM show it is not an exchangeable nitrogen. *Journal of the American Chemical Society* **2003,** 125, (19), 5604-5605.
306. Dance, I., The correlation of redox potential, HOMO energy, and oxidation state in metal sulfide clusters and its application to determine the redox level of the FeMo-co active-site cluster of nitrogenase. *Inorganic Chemistry* **2006,** 45, (13), 5084-5091.
307. Yang, T. C.; Maeser, N. K.; Laryukhin, M.; Lee, H. I.; Dean, D. R.; Seefeldt, L. C.; Hoffman, B. M., The interstitial atom of the nitrogenase FeMo-Cofactor: ENDOR and ESEEM evidence that it is not a nitrogen. *Journal of the American Chemical Society* **2005,** 127, (37), 12804-12805.
308. Rod, T. H.; Norskov, J. K., Modeling the nitrogenase FeMo cofactor. *Journal of American Chemical Society* **2000,** 122, 12751-12763.
309. Lovell, T.; Liu, T. Q.; Case, D. A.; Noodleman, L., Structural, spectroscopic, and redox consequences of central ligand in the FeMoco of nitrogenase: A density functional theoretical study. *Journal of the American Chemical Society* **2003,** 125, (27), 8377-8383.
310. Dance, I., Mechanistic significance of the preparatory migration of hydrogen atoms around the FeMo-co active site of nitrogenase. *Biochemistry* **2006,** 45, (20), 6328-6340.
311. Barriere, F., Modeling of the molybdenum center in the nitrogenase FeMo-cofactor. *Coordination Chemistry Reviews* **2003,** 236, 71-89.
312. Howard, J. B.; Rees, D. C., How many metals does it take to fix N-2? A mechanistic overview of biological nitrogen fixation. *Proceedings of the National Academy of Sciences of the United States of America* **2006,** 103, (46), 17088-17093.
313. Yandulov, D. V.; Schrock, R. R., Catalytic reduction of dinitrogen to ammonia at a single molybdenum center. *Science* **2003,** 301, (5629), 76-78.
314. Weare, W. W.; Dai, X. L.; Byrnes, M. J.; Chin, J. M.; Schrock, R. R.; Muller, P., Catalytic reduction of dinitrogen to ammonia at a single molybdenum center.

Proceedings of the National Academy of Sciences of the United States of America **2006,** 103, (46), 17099-17106.
315. Leigh, G. J., So that's how it's done - Maybe. *Science* **2003,** 301, (5629), 55-56.
316. Durrant, M. C., An atomic-level mechanism for molybdenum nitrogenase. Part 1. Reduction of dinitrogen. *Biochemistry* **2002,** 41, (47), 13934-13945.
317. Fryzuk, M. D.; Haddad, T. S.; Mylvaganam, M.; McConville, D. H.; Rettig, S. J., End-on Versus Side-on Bonding of Dinitrogen to Dinuclear Early Transition-Metal Complexes. *Journal of the American Chemical Society* **1993,** 115, (7), 2782-2792.
318. Hidai, M.; Mizobe, Y., Recent Advances in the Chemistry of Dinitrogen Complexes. *Chemical Reviews* **1995,** 95, (4), 1115-1133.
319. Bazhenova, T. A.; Shilov, A. E., Nitrogen-Fixation in Solution. *Coordination Chemistry Reviews* **1995,** 144, 69-145.
320. Cao, Z. X.; Jin, X.; Zhang, Q. N., Density functional study of the structure of the FeMo cofactor with an interstitial atom and homocitrate ligand ring opening. *Journal of Theoretical & Computational Chemistry* **2005,** 4, 593-602.
321. Ogo, S.; Kure, B.; Nakai, H.; Watanabe, Y.; Fukuzumi, S., Why do nitrogenases waste electrons by evolving dihydrogen? *Applied Organometallic Chemistry* **2004,** 18, (11), 589-594.
322. Peters, J. W.; Szilagyi, R. K., Exploring new frontiers of nitrogenase structure and mechanism. *Current Opinion in Chemical Biology* **2006,** 10, (2), 101-108.
323. Mennucci, B.; Tomasi, J.; Cammi, R.; Cheeseman, J. R.; Frisch, M. J.; Devlin, F. J.; Gabriel, S.; Stephens, P. J., Polarizable Continuum Model (PCM) Calculations of Solvent Effects on Optical Rotations of Chiral Molecules. *journal of physical chemistry A* **2002,** 106, 6102-6113.
324. Nelsen, S. F.; Blackstock, S. C.; Kim, Y., Estimation of Inner Shell Marcus Terms for Amino Nitrogen Compounds by Molecular Orbital Calculations. *Journal of the American Chemical Society* **1987,** 109, (3), 677-682.
325. Hinnemann, B.; Norskov, J. K., Chemical Activity of the Nitrogenase FeMo Cofactor with a Central Nitrogen Ligand: Density Funcitonal Study. *Journal of the American Chemical Society* **2004,** 126, 3920-3927.
326. Lindberg, R. D.; Runnels, D. D., Ground water redox potentials: an analysis of equilibrium state applied to Eh measurements and geochemical modeling. *Science* **1984,** 225, 925-927.
327. Langmuir, D., *Aqueous environmental geochemistry*. Prentice Hall: Upper Saddle River, NJ, 1997; p 600.

Appendix 1: Supplement to Kinetics of Triscarbonato Uranyl Reduction by Aqueous Ferrous Iron: A Theoretical Study

Matthew C. F. Wander[1,2], Sebastien Kerisit[3], Kevin M. Rosso[3], Martin A. A. Schoonen[1,2]

[1] Department of Geosciences, Stony Brook University, Stony Brook, NY 11794-2100

[2]Center for Environmental and Molecular Science (CEMS), Stony Brook University

[3]Pacific Northwest National Laboratory (PNNL), Richland, WA

SUPPORTING INFORMATION

Table 1. Potential parameters used in this work to model molecular water, uranyl, iron, and carbonate ions.

Charges and core-shell spring constants[a]				
Ion	Core (e)	Shell (e)	k (eV.Å^{-2})	
Uranium (U)	+2.500	-	-	
Uranyl O (O_U)	+0.500	-0.750	27.40	
Iron (Fe)	+2.000	-	-	
Carbon (C)	+1.135	-	-	
Carbonate O (O_C)	+0.587	-1.632	507.40	
Water O (O_W)	+1.250	-2.050	209.45	
Hydrogen (H)	+0.400	-	-	
Buckingham potential parameters[b]				
Ion pair (ij)	A_{ij}(eV)	ρ_{ij}(Å)	C_{ij}(eV. Å^6)	
Fe-O_C	420.00	0.3299	0.00	
C-O_W	435.00	0.3400	0.00	
C-O_U	435.00	0.3400	0.00	
O_C-O_C	16372.00	0.2130	3.47	
Born-Mayer potential parameters[c]				
Ion pair (ij)	A_{ij}(eV)	B_{ij} (Å)	C_{ij} (eV. Å^{12})	D_{ij} (eV. Å^6)
Fe-Ow	45.00	0.5764	2200.00	75.00
Lennard-Jones potential parameters[d]				
Ion pair (ij)	A_{ij} (eV. Å^n)	B_{ij} (eV. Å^m)	n	m
U-O_C	15000.00	22.00	12	6
U-O_W	15000.00	22.00	12	6
O_U-O_C	27291.72	27.12	12	6
O_U-O_W	27291.72	27.12	12	6
O_C-O_W	27291.72	27.12	12	6
Ow-Ow	39344.98	42.15	12	6
H-Ow	24.00	6.00	9	6

Table I. (cont.)

Morse potential parameters[e]				
Ion pair (ij)	D_{ij} (eV)	α_{ij} ($Å^{-1}$)	r_0 (Å)	Coul. Sub. (%)
C-O_C	4.7100	3.8000	1.1800	0
Ow-H	6.2037	2.2200	0.9237	50
H-H	0.0000	2.8405	1.5000	50
Harmonic potential parameters[f]				
Ions (ijk)	k_{ij} (eV.$Å^{-2}$)		r_0	
U-O_U	43.364		1.80	
Three-body potential parameters[g]				
Ions (ijk)	k_{ijk} (eV.rad^{-2})		θ_0	
O_C-C-O_C	1.6900		120.00	
O_U-U-O_U	13.009		180.00	
H-Ow-H	4.1998		108.69	
Four-body potential parameters[h]				
Ions (ijkl)	k_{ijkl} (eV.rad^{-1})		θ_0	
O_C-C-O_C-O_C	0.1129		180.00	
O_C-U-O_C-O_C	0.5000		180.00	

a. Spring constant potential form: $V=k.r_{c\text{-}s}^{2}$
b. Buckingham potential form: $V_{ij}=A_{ij}\exp(-r_{ij}/\rho_{ij})-C_{ij}r_{ij}^{-6}$
c. Born-Mayer potential form: $V_{ij}=A_{ij}\exp(-r_{ij}/B_{ij})+C_{ij}r_{ij}^{-12}-D_{ij}r_{ij}^{-6}$
d. Lennard-Jones potential form: $V_{ij}=A_{ij}r_{ij}^{-n}-B_{ij}r_{ij}^{-m}$
e. Morse potential form: $V_{ij}=D_{ij}(1-\exp[-\alpha_{ij}(r_{ij}-r_0)]^2)-D_{ij}$
f. Harmonic potential form: $V_{ij}=k_{ij}(r_{ij}-r_0)^2$.
g. Three-body potential form: $V_{ijk}=0.5.k_{ijk}(\theta_{ijk}-\theta_0)^2$.
h. Four-body potential form: $V_{ijkl}=k_{ijkl}[1+\cos(2\theta_{ijkl}-\theta_0)]$.

Table II. Comparison of the structural parameters of the uranyl ion in aqueous solution obtained in this work with published experimental and theoretical data.

Source	R_{1st} U-O_{H2O} (Å)	n	R_{2nd} U-O_{H2O} (Å)	Method/Model
This work	2.45	5.0	4.68	Modified Guilbaud and Wipff[a] (uranyl) de Leeuw and Parker[b] (water)
Guilbaud and Wipff[a]	2.50	5.0	-	Guilbaud and Wipff[a] (uranyl) TIP3P (water)
Hagberg *et al.*[c]	2.40	5.0	4.70	Hagberg *et al.*[c] (uranyl) Brdarski *et al.*[d] (water)
Greathouse *et al.*[e]	2.49	5.0	4.85	Guilbaud and Wipff[a] (uranyl) Flexible SPC (water)
Allen *et al.*[f]	2.41	5.3	-	XAFS - aqueous solution low chloride concentration
Sémon *et al.*[g]	2.40	4.6	-	EXAFS - aqueous solution low perchlorate concentration
Wahlgren *et al.*[h]	2.41	4.5	-	EXAFS - aqueous solution low perchlorate concentration
Neuefeind *et al.*[i]	2.42	5.0	4.46	XRS - aqueous solution low perchlorate concentration
Åberg *et al.*[j]	2.42	5.0	4.50	XRD- aqueous perchlorate solution

a. Guilbaud, P.; Wipff, G. *J. Mol. Struct. (THEOCHEM)* **1996**, *366*, 55.
b. De Leeuw, N.H.; Parker, S.C. *Phys. Rev. B* **1998**, *58*, 13901.
c. Hagberg, D.; Karlström, G.; Ross, B.O.; Gagliardi, L. *J. Am. Chem. Soc.* **2005**, *127*, 14250.
d. Brdarski, S.; Åstrand, P.; Karlström, G. *Theor. Chem. Acc.* **2000**, *105*, 7.
e. Greathouse, J.A.; O'Brien, R.J.; Bemis, G.; Pabalan, R.T. *J. Phys. Chem. B* **2002**, *106*, 1646.
f. Allen, P.G.; Bucher, J.J.; Shuh, D.K.; Edelstein, N.M.; Reich, T. *Inorg. Chem.* **1997**, *36*, 4676.
g. Sémon, L.; Boehme, C.; Billard, I.; Hennig, C.; Lützenkrichen, K.; Reich, T.; Roßberg, A.; Rossini, I.; Wipff, G. *ChemPhysChem* **2001**, *2*, 591.
h. Wahlgren, U.; Moll, H.; Grenthe, I.; Schimmelpfennig, B.; Maron, L.; Vallet, V.; Gropen O. *Inorg. Chem.* **2001**, *40*, 3516.
i. Neuefeind, J.; Soderholm, L.; Skanthakumar, S. *J. Phys. Chem. A* **2004**, *108*, 2733.
j. Åberg, M.; Ferri, D.; Glaser, J.; Grenthe, I. *Inorg. Chem.* **1983**, *22*, 3986.

Figure 1. Uranyl oxygen-water oxygen and uranyl oxygen-water hydrogen radial distribution functions showing the lack of direct hydrogen bonding between water and uranyl oxygen ions and the formation of a 3 Å cavity around uranyl oxygen ions as described by Hagberg *et al.*[a].

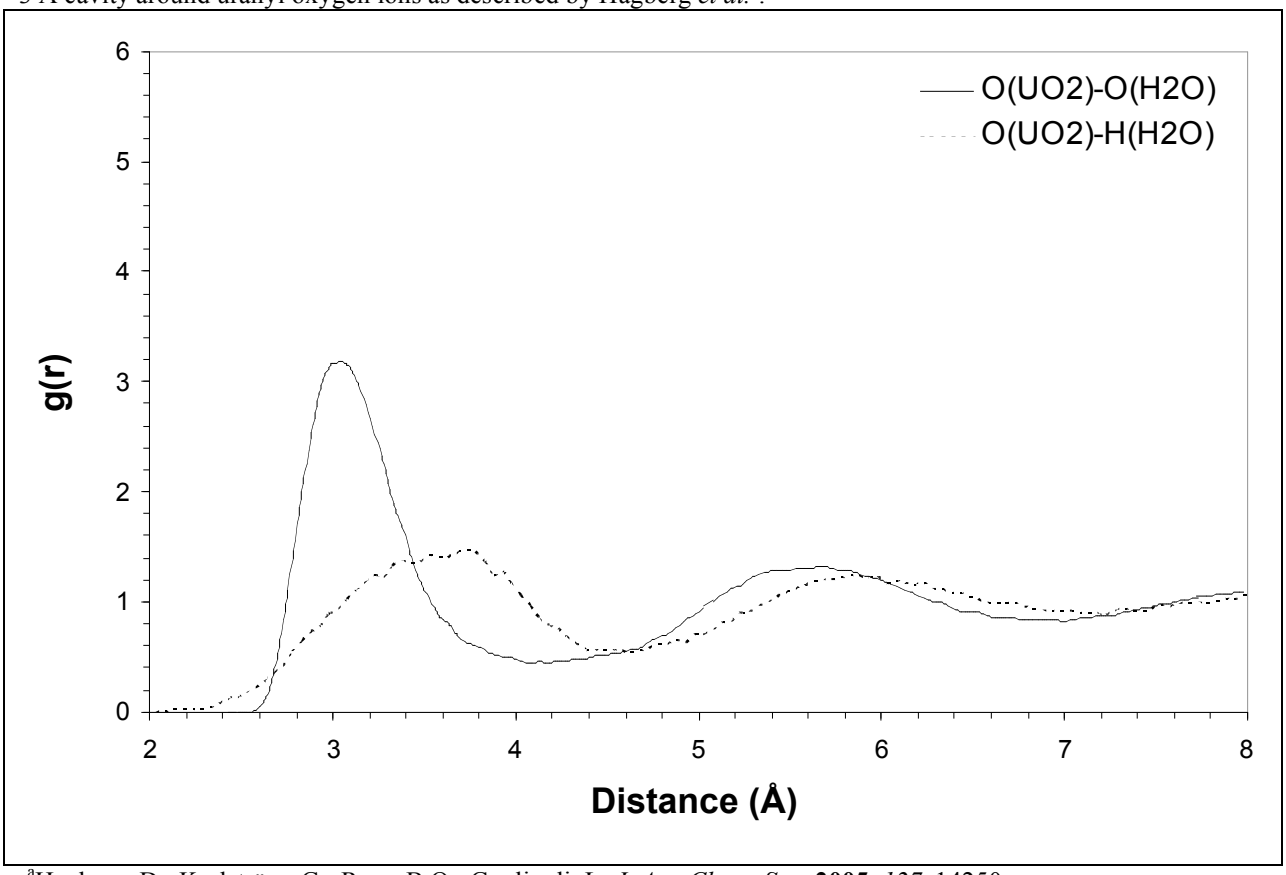

[a]Hagberg, D.; Karlström, G.; Ross, B.O.; Gagliardi, L. *J. Am. Chem. Soc.* **2005**, *127*, 14250.

Table III. Comparison of the structural parameters (Å) of the triscarbonato uranyl complex obtained in this work with published experimental and theoretical data.

Source	*R* U-O_1	*R* U-O_2	*R* U-O_3	*R* U-C	Method/Model
This work	1.83	2.44	4.06	2.86	gas-phase
This work	1.82	2.39	3.97	2.80	solution
Hemmingsen *et al.*[a]	1.85	2.58	-	-	B3LYP/DZ - gas-phase
Hemmingsen *et al.*[a]	1.77	2.57	-	-	HF/DZ - gas-phase
Vázquez *et al.*[b]	1.85	2.56	4.29	3.01	DFT - gas-phase
Vázquez *et al.*[b]	1.85	2.46	4.16	2.90	DFT - solution
Gagliardi *et al.*[c]	1.89	2.43	4.79	2.89	MBPT2 - gas-phase
Gagliardi *et al.*[c]	1.88	2.41	4.11	2.84	MBPT2 - solution
Bernhard *et al.*[d]	1.80	2.44	4.20	2.89	EXAFS
Docrat *et al.*[e]	1.80	2.43	4.13	2.81	EXAFS

a. Hemmingsen, L.; Amara, P.; Ansoborlo, E; Field, M.J. *J. Phys. Chem. A* **2000**, *104*, 4095.
b. Vázquez, J.; Bo, C.; Poblet, J.M.; de Pablo, J.; Bruno, J. *Inorg. Chem.* **2003**, *42*, 6136.
c. Gagliardi, L.; Grenthe, I.; Ross, B.O. *Inorg. Chem.* **2001**, *40*, 2976.
d. Bernhard, G.; Geipel, G.; Reich, T.; Brendler, V.; Amayri, S.; Nitsche, H. *Radiochim. Acta* **2001**, *89*, 511.
e. Docrat, T.I.; Mosselmans, J.F.W.; Charnock, J.M.; Whiteley, M.; Collison, D.; Livens, R.F.; Jones, C.; Edmiston, M. *Inorg. Chem.* **1999**, *38*, 1879.

Figure 2. Snapshots from the MD simulations of the 2xmonodentate (a), 1xbidentate (b), solvent-separated (c), and 1xmonodentate (d) iron(II)-triscarbonato uranyl complexes.

a

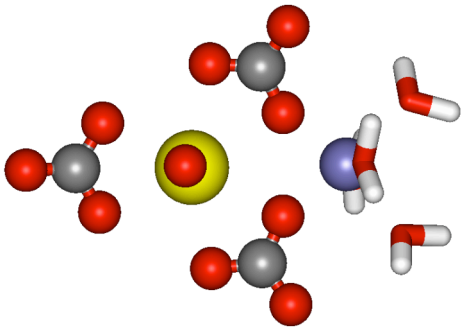

b

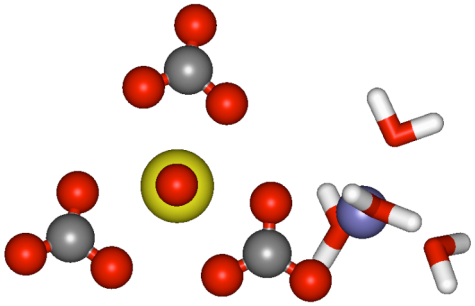

c

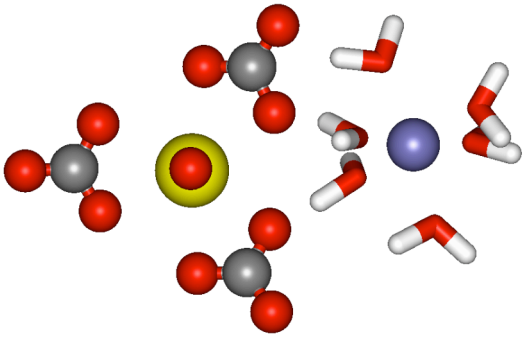

d

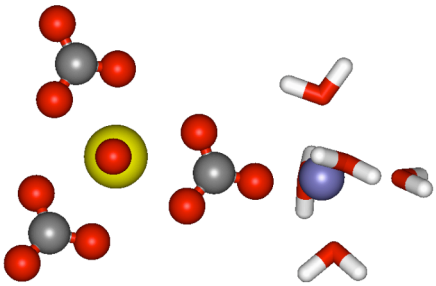

Table IV. Comparison of the distances (Å) calculated from the potential model and DFT calculations for the II/II/IV iron triscarbonato uranyl complex.

Distance	Fe_1-O_{H2O}	Fe_1-O_{H2O}	Fe_1-O_{H2O}	Fe_1-O_{H2O}	Fe_1-O_{CO}	Fe_1-O_{CO}
MD	2.28	2.07	2.38	2.04	2.28	1.82
DFT	2.34	2.22	2.16	1.95	2.76	2.01
Distance	Fe_2-O_{H2O}	Fe_2-O_{H2O}	Fe_2-O_{H2O}	Fe_2-O_{H2O}	Fe_2-O_{CO}	Fe_2-O_{CO}
MD	2.18	2.16	2.11	2.26	1.92	1.84
DFT	2.30	2.11	2.20	2.28	2.09	2.02
Distance	U-O_{CO}	U-O_{CO}	U-O_{CO}	U-O_{CO}	U-O_{CO}	
MD	2.41	2.31	2.31	2.43	2.36	
DFT	2.45	2.36	2.35	2.43	2.49	
Distance	U-O_{UO}	U-O_{UO}	Fe_1-U	Fe_2-U		
MD	1.82	1.82	3.72	4.04		
DFT	1.78	1.78	3.86	4.07		

Table V. Comparison of the experimental and calculated cell parameters and bulk modulus of siderite ($FeCO_3$).

Source	a (Å)	b (Å)	c (Å)	Bulk modulus (GPa)
Calculated	4.4696	4.4696	15.3465	105
Experimental[a]	4.6916	4.6916	15.3796	117[b]

a. Effenberger, H.; Mereiter, K.; Zemann, *J. Z. Kristalogr*. **1981**, *156*, 233.
b. Zhang, J.; Reeder, R.J. *Am. Mineral*. **1999**, *84*, 861.

Table VI: Final Ab-intio optimized structures:

$Fe(II)Fe(II)U(VI)O_2(CO_3)_2(H_2O)_8$			
U	0.39047227	-0.27937199	-0.68307657
O	0.26109998	1.37425051	-0.03708733
O	0.43130597	-1.93320667	-1.32585800
Fe	-1.44147978	-0.16653943	-4.08365861
Fe	-2.59082340	-0.18439402	2.07889965
C	0.37667567	-1.08320329	2.06304414
O	1.41690370	-0.99571087	1.31969847
O	-0.76619070	-0.92701608	1.38217332
O	0.37082404	-1.26655533	3.30030216
C	1.44160912	0.44532387	-3.24586446
O	0.11439627	0.47062929	-2.98224345
O	2.12482318	0.29616865	-2.16437388
O	1.87217143	0.52208761	-4.40208173
C	-3.19456172	-0.20128028	-0.94862168
O	-2.00252954	-0.25611026	-1.38133441
O	-3.50876584	-0.09974400	0.28356571
O	-4.20358911	-0.23888822	-1.78992787
O	-3.37067564	-0.43401238	-4.18813939
H	-3.74575416	-1.17765555	-4.66759963
H	-3.88503971	-0.35139125	-2.76143169
O	-0.71070836	-2.25716871	-3.93467662
H	-0.06495020	-2.51049714	-4.60456031
H	-0.29376644	-2.41535570	-3.06797813
O	-0.23287164	0.10162351	-5.85787490
H	-0.48466707	0.87685891	-6.37172626
H	0.66656518	0.31252051	-5.44210960
O	-2.28984726	1.97638262	-4.51096153
H	-2.25720262	2.66212867	-3.83536064
H	-3.18546981	1.59797915	-4.50344958
O	-1.67985227	1.81578091	1.99360224
H	-2.18874570	2.62838807	1.90839144
H	-0.95175357	1.85374340	1.34212908
O	-1.89089185	-0.58035480	4.03258977
H	-1.85619374	0.10288258	4.70964823
H	-0.89556485	-0.90157183	3.83503755
O	-4.66541564	0.61933701	2.56533579
H	-5.22780505	0.02284023	3.07296960
H	-4.95062209	0.53195096	1.63950841
O	-3.46380037	-2.27187180	2.50342612
H	-2.99997820	-2.51413513	3.31667059
H	-3.23823547	-2.94392772	1.84935399

$Fe(III)Fe(II)U(V)O_2(CO_3)_2(H_2O)_8$			
U	0.44436076	-0.26668506	-0.63083014
O	0.23562612	1.42377684	0.03038336
O	0.54549976	-1.93334841	-1.37030978
Fe	-1.49202907	-0.16850862	-3.96368517
Fe	-2.66222649	-0.17226423	1.84455174
C	-0.00295894	-1.42186252	2.00594122
O	1.15724713	-1.23640182	1.54383594
O	-0.99522324	-1.00289388	1.17205759

O	-0.33603207	-1.91370346	3.11687010
C	1.45168270	0.52269285	-3.30503251
O	0.16253464	0.54614916	-3.03879456
O	2.25911689	0.46743271	-2.37560003
O	1.82400217	0.53759171	-4.57068407
C	-3.25015747	-0.25340168	-1.27786072
O	-2.06915312	-0.21742790	-1.80708549
O	-3.48644326	-0.20055851	-0.05385435
O	-4.30881934	-0.32991153	-2.07698275
O	-3.31218319	-0.36417617	-4.45883014
H	-3.60225794	-0.94560217	-5.16734149
H	-4.02702279	-0.40416826	-3.03463752
O	-0.86422514	-2.15691075	-3.59217745
H	-0.29037981	-2.47226521	-4.30131778
H	-0.34399023	-2.22439200	-2.73536398
O	-0.54024853	-0.16102495	-5.60328725
H	-0.96103085	0.04442126	-6.44352376
H	1.01980608	0.40479685	-5.14013095
O	-2.01502246	1.98552603	-3.88573817
H	-1.57937122	2.44119637	-3.15434829
H	-2.96636501	2.13221880	-3.81621443
O	-1.86102816	1.90116026	1.65244351
H	-2.40006534	2.60647295	1.28061626
H	-1.04258644	1.84424485	1.08953154
O	-1.94591347	0.02815135	3.95112159
H	-1.46686212	0.85740131	4.06635554
H	-1.26206279	-0.69380561	3.93161030
O	-4.50869724	0.45175147	2.84142449
H	-4.43193415	0.13725711	3.75275310
H	-5.32778604	0.09345053	2.47937840
O	-3.08137076	-2.28049439	2.62578945
H	-2.14253967	-2.45361076	2.87742312
H	-3.29479469	-2.93135942	1.94789221

$Fe(III)Fe(III)U(IV)O_2(CO_3)_2(H_2O)_8$			
U	0.62385341	-0.26455967	-0.67721312
O	0.23105381	1.71033741	-0.06910104
O	0.50657940	-2.24104577	-1.34617373
Fe	-1.46387773	-0.42646123	-3.68417255
Fe	-2.45547271	0.09703285	1.83678204
C	0.37873549	-0.90124009	2.18349523
O	1.44961257	-0.88131880	1.51154926
O	-0.73820395	-0.69700476	1.40788424
O	0.24210092	-1.07923269	3.40869021
C	1.46829108	0.30605566	-3.41133143
O	0.15936227	0.38817785	-2.97507447
O	2.27148993	0.19622295	-2.43884093
O	1.68699464	0.33485436	-4.63093412
C	-3.12649184	-0.03446551	-1.17599242
O	-1.94621982	-0.36573524	-1.64458593
O	-3.33519519	-0.15452214	0.09767441
O	-4.04261375	0.37422309	-1.93736790
O	-3.50090367	-0.65326758	-4.22124696

H	-3.73342064	-1.58358109	-4.32329488
H	-3.94969287	-0.29667671	-3.39132971
O	-1.07414216	-2.23179540	-3.83370933
H	-0.68832620	-2.58221858	-4.64431354
H	0.07337969	-2.59979596	-2.13943511
O	-0.66526007	0.04885270	-5.58056878
H	-1.01649912	0.84011424	-6.00497578
H	0.32945599	0.21597920	-5.35953123
O	-2.18767781	1.73278062	-3.67978499
H	-1.49703558	2.19312565	-3.18260182
H	-2.98467105	1.74470200	-3.12049001
O	-2.00415163	1.88815342	1.88828639
H	-2.65275984	2.59926100	1.90665292
H	-0.28894294	2.08067197	0.66266801
O	-2.08537954	-0.34129726	3.86616070
H	-2.07834290	0.44571625	4.42342361
H	-1.09139733	-0.68864432	3.81222352
O	-4.59482450	0.38591525	2.40006548
H	-4.90059075	-0.39105874	2.88578221
H	-4.97315631	0.30971247	1.50918944
O	-3.26282714	-2.11394752	2.09704881
H	-2.72322183	-2.59599298	2.73656570
H	-3.13051530	-2.54711288	1.24427758